Stochastic Methods for Unsteady Aerodynamic Analysis of Wings and Wind Turbine Blades

by

Manuel Fluck
Dipl.-Ing. Univ., Technical University of Munich, 2010

A Dissertation Submitted in Partial Fulfillment of the
Requirements for the Degree of

DOCTOR OF PHILOSOPHY

in the Department of Mechanical Engineering

Stochastic Methods for Unsteady Aerodynamic Analysis of Wings and Wind Turbine Blades

by

Manuel Fluck
Dipl.-Ing. Univ., Technical University of Munich, 2010

Supervisory Committee

Dr. Curran A. Crawford, Supervisor
(Department of Mechanical Engineering)

Dr. Bradley J. Buckham, Departmental Member
(Department of Mechanical Engineering)

Dr. Adam H. Monahan , Outside Member
(School of Earth and Ocean Sciences)

ABSTRACT

Advancing towards 'better' wind turbine designs engineers face two central challenges: first, current aerodynamic models (based on Blade Element Momentum theory) are inherently limited to comparatively simple designs of flat rotors with straight blades. However, such designs present only a subset of possible designs. Better concepts could be coning rotors, swept or kinked blades, or blade tip modifications. To be able to extend future turbine optimization to these new concepts a different kind of aerodynamic model is needed. Second, it is difficult to include long term loads (life time extreme and fatigue loads) directly into the wind turbine design optimization. This is because with current methods the assessment of long term loads is computationally very expensive – often too expensive for optimization. This denies the optimizer the possibility to fully explore the effects of design changes on important life time loads, and one might settle with a sub-optimal design.

In this dissertation we present work addressing these two challenges, looking at wing aerodynamics in general and focusing on wind turbine loads in particular. We adopt a Lagrangian vortex model to analyze bird wings. Equipped with distinct tip feathers, these wings present very complex lifting surfaces with winglets, stacked in sweep and dihedral. Very good agreement between experimental and numerical results is found, and thus we confirm that a vortex model is actually capable of analyzing complex new wing and rotor blade geometries.

Next stochastic methods are derived to deal with the time and space coupled unsteady aerodynamic equations. In contrast to deterministic models, which repeatedly analyze the loads for different input samples to eventually estimate life time load statistics, the new stochastic models provide a continuous process to assess life time loads in a stochastic context – starting from a stochastic wind field input through to a stochastic solution for the load output. Hence, these new models allow obtaining life time loads much faster than from the deterministic approach, which will eventually make life time loads accessible to a future stochastic wind turbine optimization algorithm. While common stochastic techniques are concerned with random parameters or boundary conditions (constant in time), a stochastic treatment of turbulent wind inflow requires a technique capable to handle a random field. The step from a random parameter to a random field is not trivial, and hence the new stochastic methods are introduced in three stages.

First the bird wing model from above is simplified to a one element wing/ blade model, and the previously deterministic solution is substituted with a stochastic solution for a one-point wind speed time series (a random process). Second, the wind inflow is extended to an n-point correlated random wind field and the aerodynamic model is extended accordingly. To complete this step a new kind of wind model is introduced, requiring significantly fewer random variables than previous models. Finally, the stochastic method is applied to wind turbine aerodynamics (for now based on Blade Element Momentum theory) to analyze rotor thrust, torque, and power.

Throughout all these steps the stochastic results are compared to result statistics obtained via Monte Carlo analysis from unsteady reference models solved in the conventional deterministic framework. Thus it is verified that the stochastic results actually reproduce the deterministic benchmark. Moreover, a considerable speed-up of the calculations is found (for example by a factor 20 for calculating blade thrust load probability distributions).

Results from this research provide a means to much more quickly analyze life time loads and an aerodynamic model to be used a new wind turbine optimization framework, capable of analyzing new geometries, and actually optimizing wind turbine blades with life time loads in mind. However, to limit the scope of this work, we only present the aerodynamic models here and will not proceed to turbine optimization itself, which is left for future work.

Table of Contents

List of Tables

List of Figures

ACKNOWLEDGEMENTS

I would like to thank everyone who gave me his or her support during this work.

This is first of all my supervisor Dr. Curran Crawford, who invited me to join the Sustainable Systems Design Lab (SSDL) and pursue my PhD studies under his guidance. Curran, you have been a roll model and a source of inspiration, both professionally and in private matters. The seed of this work grew out of our discussions. Although your time was sparse, you were always there when I really needed advice. I also like to thank my advisory committee, Dr. Buckham and Dr. Monahan, for overseeing this work, as well as the external examiner, Dr. Bottasso, for reviewing this work from my old alma mata in Munich.

Moreover I would like to thank my coworkers and fellow students, both engineers and from all over campus. I thank you for sharing your thoughts, asking/ answering questions, leading exciting discussions and challenging my thoughts. Especially I would like to thank Dr. Michael McWilliam and Dr. Usman Khan. Thank you Mike for kicking me off into this project and for your never-ending explanations about how stuff works. Thanks Ozzy for being an awesome office mate and friend – since you graduated I have been missing your insights and thoughts (particularly on Monday mornings). It was my honor to follow your advice.

Special thanks goes to Susan Walton for her administrative support, but even more for having an open ear, valuable advise, and usually a good story to share, too; And to Ged McLean: Thanks for all your time, Ged. Your advice is still invaluable in so many aspects!

I owe thanks to the Pacific Institute for Climate Solutions (PICS), the Institute for Integrated Energy Systems at the University of Victoria (IESVic), the Natural Sciences and Engineering Research Council of Canada (NSERC), and once more the German Academic Exchange Service (DAAD) for their financial support. I had the freedom to put all the necessary time in this project only through your support.

Finally I want to say “thanks” to all my friends and family – particularly my parents and grandparents. Again you saw me leaving for an exciting opportunity. I know it has (once again) not been easy to say goodbye. I gratefully acknowledge you understanding why I left and the freedom you gave me to spread my wing and lean to fly.

Danke euch allen!

Manuel Fluck

Chapter 1

Introduction

Climate change is obvious. Moreover, as the famous Canadian science broadcaster and environmental activist David Suzuki puts it, climate change is "one of the greatest challenges humanity will face this century. Confronting it will take a radical change in the way we produce and consume energy" (Suzuki, 2014). Producing a large portion of our electricity from renewable energies may be such a radical change. With its wide availability, positive impact on the local economy and potential to create local jobs[1], and little 'costs' to society[2], wind power is a promising candidate among the multiple forms of renewable energy. Decision makers in politics and industry have realized the potential of wind energy, thus spurring an increase in wind energy installation. For 2015 this led to installation of 63 GW of new wind capacity, a 17.1 % cumulative capacity growth rate (GWEC, 2015). This trend is expected to continue for the next years. From now up to 2020 GWEC (2015) expects an annual installed capacity growth rate of around 5 %.

This growth is driven by a rapid progress in wind turbine technology, leading to larger turbines and the ability to harvest wind energy at less favorable locations. However, as wind power takes over an increasing share of electricity production, stability of the electrical grid becomes a concern. With an increasing amount of wind

[1] The British government for example recognizes that "the offshore wind sector has the potential to become one of strategic economic importance to the UK [...]. In 2020/21, under a strong growth scenario, the sector could deliver in the order of £ 7 bn Gross Value Added to the UK economy (excluding exports) and support over 30,000 full time equivalent UK jobs." (HM Government, 2013).

[2] Stiesdal (2013) adds various social, political and economic contributions to the levelized cost of energy (LCOE) to arrive at the "Society's Cost of Electricity", or SCoE, a cost that is supposed to reflect the 'real costs' of electricity produced by a certain source. For the UK in 2025 he finds wind power to have the lowest SCoE.

power generated from large turbines, some of them in increasingly less favorable sites (i.e. less windy, more turbulent sites) the dynamic fluctuations in the wind power production (driven by unsteady wind) increases, too. This variable input is becoming a challenge for the electricity utilities, which are trying to balance power supply and demand (Altın et al., 2010; Zhang et al., 2010; Heier, 2014). To sustain ongoing growth in wind power production several questions have to be addressed, all revolving around three central trends: larger turbines, less favorable sites, and grid stability issues with increased wind power generation.

The research project presented in this dissertation aims at one factor that impacts all three of these core trends: unsteady turbulent wind. In the following we will look at:

- ◇ How unsteady turbulent wind is modeled as a source term in engineering analyses;
- ◇ The way unsteady effects of turbulent wind are currently dealt with in engineering analysis;
- ◇ The reasons why these unsteady effects are of growing importance for the design of the next generation of wind turbines;
- ◇ The deficiencies of the current methods to deal with unsteady effects of turbulent wind;
- ◇ An alternative approach to deal with unsteady effects of turbulent wind.

Many of the findings presented in this dissertation are not specific to wind turbine engineering; instead, they are applicable to multiple fields of wind engineering and sometimes beyond. We will mention these other applications in places, but keep our main focus on wind energy applications.

1.1 Background and motivation

Wind in the atmospheric boundary layer is highly turbulent, with wind speeds inherently unsteady quantities varying considerably in space and time on various scales (Emeis, 2012). Wind turbines typically operate within this atmospheric boundary layer, although certain geographical and meteorological conditions exist where modern wind turbines operate at least partially above the atmospheric boundary layer. Naturally,

the wind speed fluctuations a turbine blade encounters transfer to fluctuating blade forces, fluctuating structural loads and finally a highly fluctuating power output. Milan et al. (2013) for example found in an eight month data set wind speed changes of up to 11 m/s within only 8 s. For the 2 MW turbine regarded in this study they also found turbine power changes of 82.5 % within these 8 s. This indicates that short term wind speed variations do have a considerable influence on turbine performance and load. Zhou et al. (2016) show that the peak power fluctuation for wind turbines (estimated by twice the rms values) can reach 22% of its average. These strong fluctuations in wind forcing and resulting turbine loads are not without consequences, particularly when looking at current trends in wind turbine design.

1.1.1 Current trends in wind turbine design

We identify the following current trends in wind turbine design:

Trend towards harvesting wind power at less favorable sites: As the installed wind power capacity increases globally, the best sites are quickly occupied, leaving only less favorable sites or moving off-shore. To enable further on-shore development and to make second tier sites economically attractive wind turbines have to become (technically and economically) more efficient, because electricity has to be generated under worse conditions but at similar cost. 'Worse' often means 'less mean wind speed' and/ or 'more fluctuations'. Thus, this directly leads to the second trend.

Trend towards larger turbines: To capture more power from less wind at second tier sites the turbine rotor diameter is increased to capture more wind. Moreover, larger turbines, with stronger generators, are also favored at top tier sites and off-shore to harvest more energy while simultaneously reducing the cost of electricity through economy of scale. For larger turbines, however, blade elasticity is of growing importance to correctly predict fundamental design parameters such as tower clearance and fatigue loads (Zhang and Huang, 2011). Since blade vibrations, a major source of fatigue, are mainly driven by turbulent wind effects, the accurate translation of unsteady wind loads to unsteady blade forces becomes increasingly crucial. Moreover, increased blade motions add another unsteady term (viz., the relative wind velocities due the the blade motion) to the apparent wind[3] equation. Thus, for large turbine

[3] Borrowed from sailing terminology, apparent wind is used to denote the flow as the blade 'sees' it, including all blade motion and wake induced velocities as well as (tower) blockage effects.

blades including unsteady aerodynamics becomes increasingly relevant.

Rising grid stability issues: With increasing wind power grid penetration the impact on grid stability from the variable and uncontrollable wind source increases. Unsteady wind is again the driving cause as it is the unsteady power generation that threatens grid stability. This is certainly true for longer time scales of wind speed fluctuations (over ten minutes), where wind speed changes can still be treated quasi steady. But, as shown by Milan et al. (2013), wind speed fluctuations at much higher frequencies are also transferred to output power fluctuations. If and how these higher frequency fluctuations affect grid stability is still unclear. At the same time considerable research effort is directed to developing smart grid technologies (Holttinen et al., 2011) to meet fluctuations on the generation side by controlled changes on the demand side (Williams et al., 2013; Broeer et al., 2014). Although power and grid electronics is certainly out of the scope of this project, modeling the relation between real (higher frequency) wind speed fluctuations and output power fluctuations correctly is essential to analyzing its influence on the grid and devising appropriate smart grid strategies. Thus, assessing the unsteady aerodynamic loads correctly is fundamental to possibly designing future wind turbines, which enhance grid stability rather than compromising it.

1.1.2 The need for unsteady optimization considering life time loads and unsteady power output

In order to offer the 'best' wind turbine possible its design has to be optimized for the conditions it is working in. This includes considering different wind speeds and the turbulent wind conditions over the period of the turbine's life time. With the trends discussed above, unsteady optimization becomes essential to correctly account for the dynamic loads and unsteady power output. Once considering both on a life time scale the optimum design may shift to different aerodynamic shapes, different structural layouts, and different controller designs, resulting in a different cost of electricity.

Moreover, regarding growing grid stability issues it can be expected that the optimization objectives and with it wind turbine controller design objectives have to be revisited in the future. Will the current version, solely driven by narrow economic considerations focused on the total power generation, still hold in the next years?

What are the real costs to be minimized? Will we rather have to turn to a more global optimization, including power grid stability and market effects?

Regardless what the answer to these questions will be, including unsteady effects in future optimization routines will be essential, whether to predict the impact on grid performance or to minimize LCOE for the wind as it is out there: unsteady. However, unsteady optimization is limited at this moment.

Currently wind turbines are usually optimized based on time stepping simulations run for relatively short (e.g. 600 s) wind samples, often these simulations are even fed only with mean wind speeds or mean wind speed distributions. The aerodynamic equations are usually solved through a Blade Element Momentum (BEM) model (Burton et al., 2011; Bladed, 2012; Hansen, 2008). This results in two challenges, which are becoming increasingly relevant with the trends identified above. Firstly, BEM solvers are inherently limited to planar rotor designs. This neglects more complex, possibly more advantageous geometries. Secondly, basing wind turbine optimization on one or at best a few short samples neglects long term dynamic effects. The wind turbine design standard IEC 61400-1, Ed. 3 (2005) is indicative for this process: it bases the turbine (life time) load analysis on multiple unsteady 600 s simulations, for multiple different design load cases (DLCs), analyzed at many different mean wind speeds superimposed with turbulent fluctuations, every one repeated several times with different realizations of the turbulent fluctuations, each generated from a different random seed. This results in a large number of analyses. The computational costs associated with this multitude of analyses obviously present a challenge to optimization, where additionally many different candidate designs have to be evaluated. Moreover, extrapolation from a limited data set to life time extreme loads is a delicate exercise and results can vary greatly (Moriarty, 2008; Burton et al., 2011; Tibaldi et al., 2014; Zwick and Muskulus, 2015). This poses an additional challenge for wind turbine optimization, particularly when concerned with gradient-based methods, where obtaining reliable design variable gradients is vital.

As a result of these challenges, wind turbines are usually 'optimized' first, and life time unsteady loads are assessed afterwards via the analysis of the DLCs from IEC 61400-1, Ed. 3 (2005)). However, relying on BEM and not considering life time loads is obviously sub-optimal, because:

A) BEM based solvers cannot explore unconventional, but potentially beneficial new designs such as winglets, ailerons, swept or downwind coning rotors, etc., and
B) the optimization is blind to the important (Kareem, 2008) cost savings of modified long term loads and power production from different blade designs operating in unsteady conditions.

So far only very few multidimensional optimization (MDO) frameworks have been presented, which try to address the second point and include life time loads into the optimization (Bottasso et al., 2012; Ashuri et al., 2014; Chew et al., 2016; Bortolotti et al., 2016). However, these tools typically only assess a few selected DLCs and/ or rely on nested aero-structural loops. While in principle any number of DLCs could be analyzed and a large number of iteration could be performed to converge the nested optimization loops, the limiting factors are the substantial computational costs. These costs lead to long solution times, which are not too problematic in academic research, but are problematic for industry applications, where over night results are vital. Merz (Merz, 2015a,b) and Lupton (2014), on the other hand, develop a frequency space model and thus are able to consider significantly more DLCs at much lower computational cost. However, both still relay on BEM for the aerodynamic modeling, and thus do not address point (A). Moreover, their frequency domain approach brings the usual challenges with respect to non-liner effects.

Lagrangian vortex models (LVM) based on Prandtl's lifting line theory (Prandtl, 1918, 1919) are an attractive solution to (A), see for example Junge et al. (2010); McWilliam et al. (2013b); McWilliam (2015). They are relatively fast to solve, and – as we will show later (Chapter 2) – flexible enough to handle unconventional geometries. Point (B), on the other hand, is more demanding, particularly when employing LVM equations to assess new geometries. These equations are more time consuming to solve then BEM, especially in unsteady conditions. Hence, time stepping through multiple LVM solutions to obtain data for extrapolation to long term loads is not an option within the time budget of any practicable optimization program. To resolve this, we suggest a fundamental shift in how we approach unsteady loads.

1.1.3 A new perspective on unsteady analysis

Unsteady wind turbine blade loads are caused by the unsteady aerodynamic forcing during the turbine's life time of some 20 years. However, calculating turbine loads for a time series of 20 years of wind data is difficult. This is too long a time span for a conventional model with a high enough temporal resolution to capture all relevant frequencies. Hence one usually resorts to the (well known, but unsatisfactory) process summarized in Fig. 1.1: extracting several short samples out of the 20 year wind speed time series, analyzing each sample individually, and subsequently populating a load probability distribution (PDF) to extrapolate life time loads. This is a deterministic approach. Each wind speed sample represents one specific time series of wind data. And each load solution is the (deterministic) solution to one of these specific samples. There is no randomness in the analysis, and statistics of the life time loads (e.g. return periods, probabilities of exceedance) are obtained via a Monte Carlo kind of analysis from multiple deterministic solutions.

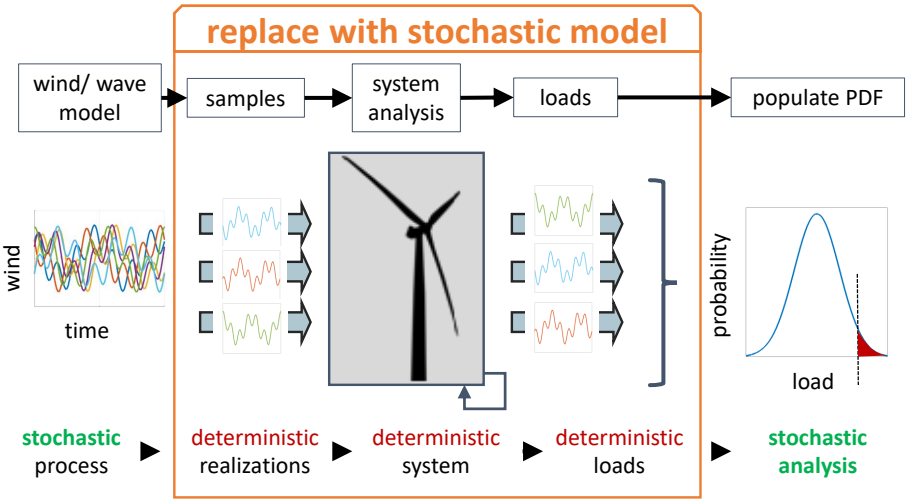

Figure 1.1: Comparison deterministic vs. stochastic approach.

Alternatively the unsteady wind forcing can be regarded as a stochastic process: random, but highly correlated in time and space. What we called a 'short wind speed sample' thus becomes one wind speed *realization*. From this point of view rotor loads are the output of a system excited by a random process. Hence the loads are a random process, too, and the loads we calculated for one wind speed sample, i.e. one wind

speed realization, become one specific realization of the stochastic loads. Once we have adopted this stochastic view, how about we try to treat the problem as such, too: a stochastic problem, driven by a random input, yielding a random output? This means replacing the deterministic steps in Fig. 1.1 with a direct stochastic analysis as called for by the input. This view opens the door to a new approach to deal with unsteadiness – now viewed as randomness – in wind turbine aerodynamics.

In this dissertation we will first briefly look at Lagrangian vortex models and study their suitability for analyzing and thus optimizing new and unconventional wind turbine blade geometries. We then will turn towards the new stochastic view to assess unsteady loads. This new approach will allow us to extract long term loads from one single stochastic solution. In the sequel we will focus on unsteady aerodynamic wind turbine blade loads. However, the approach can be similarly applied to e.g. bridges under wind load, or offshore structures under (possibly combined wind and) wave loads.

1.2 Objective

Tackling the above identified deficiencies in current wind turbine optimization is a bigger task than manageable in a single PhD student life. Accordingly, the scope of this dissertation includes only a selected set of tasks from a more comprehensive research endeavor geared towards advanced wind turbine optimization, capable of expanding rotor design towards new blade geometries (Cline et al., 2011; Lawton and Crawford, 2012, 2013, 2014; McWilliam, 2015; Ghulam, 2016; Karimi et al., 2017).

The principal objective the work presented here is:

> *Develop a method to assess unsteady turbulent wind loads to be used in a new wind turbine design optimization framework.*

This objective yields three tightly interconnected challenges:

1. To work with an aerodynamic model capable of handling the unsteady aerodynamic loads introduced through turbulent atmospheric wind on various time scales.

2. To choose time scales such that "life time loads" are captured appropriately. For wind turbine design these are usually the most extreme loads (ultimate loads) and the worst combination of fatigue loads to be expected over the turbines life time. Hence time scales from fractions of seconds (the highest relevant structural vibration excitation frequency) to 20 or 25 years (the turbine life time) have to be assessed.

3. To develop a method employable in a (future) optimization framework, i.e. one that is fast enough that the analysis of life time loads is feasible for hundreds or even thousands of candidate designs with reasonable computational effort.

With the Lagrangian vortex model a promising candidate to tackle (1) is available. However, this needs to be verified. Points (2) and (3) is where the crux hides. Because a life time load assessment is expensive, point (2) is usually addressed after the turbine optimization, often with Monte Carlo like analysis based on wind input generated from multiple random seeds, see Section 1.1.2. However, a Monte Carlo approach often poses problems for optimization routines, point (3), because with these methods the design evaluation is not only dependent on design variable changes, but also on the specific random seed used. Particularly with a limited number of random seeds (i.e. a limited set of wind speed samples analyzed) the effects from the seeds can override design variable effects, and hence render optimization very difficult (Moriarty, 2008; Tibaldi et al., 2014; Zwick and Muskulus, 2015). To address points (2) and (3), and to make the life time load assessment accessible to an optimization routine, requires a shift in perspective and a fundamentally different approach.

As indicated above, stochastic methods provide this new approach. It is the objective of this dissertation to summarize the development of these stochastic methods, to present their application to the problem at hand (wind turbine aerodynamics), and to give an outlook onto the relevance of the new models to wind turbine optimization.

1.3 Work flow and dissertation outline

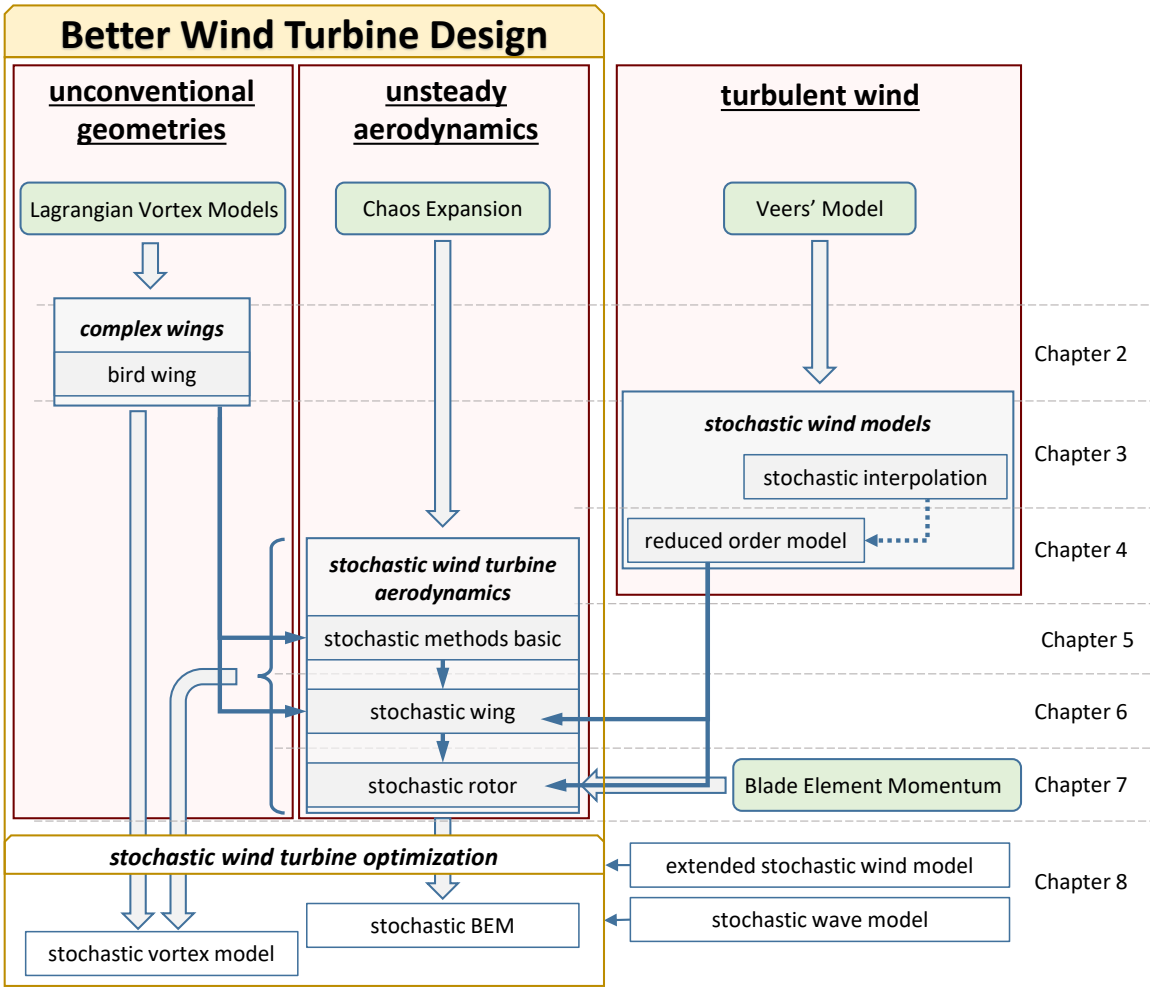

Figure 1.2: Research work flow underlying this dissertation.

This dissertation is composed of a collection of six independent (but connected) articles which are published or submitted for publication in peer reviewed academic journals. Each of the central chapters presents one article. Thus each chapter is self contained, including its own introduction, literature review, specific objectives, methods, results and discussion, as well as its own abstract and conclusions. This allows the reader to specifically select the chapters most relevant to them without having to work though the whole dissertation. The nomenclature is generally similar in all chapters, but (due to different journal standards and a limited set of symbols available) not completely identical. A nomenclature overview is included in most chapters, in

others the terms are defined in the text. This was driven by the standards of the journal, which a specific chapter was published in. In any case the full nomenclature and all terms are completely explained within each chapter.

The work flow of the underlying research is summarized in Fig. 1.2. It comprises three major building blocks:

1. Leaving blade element momentum theory and moving to a more flexible aerodynamics model to be able to analyze **new turbine blade geometries**.

2. Leaving the world of deterministic analyses and turn towards stochastic models to provide a means to efficiently assess **unsteady aerodynamic loads** within the turbine optimization loop.

3. In order to successfully implement (2) **turbulent atmospheric wind** had to be looked at as the main source of stochasticity in the system at hand.

These three blocks translate to the dissertation structure as follows:

Chapter 1 sets the stage, gives an overview of the background of the conducted research, provides the motivation behind it, presents this outline of the dissertation, and concludes with an overview of the central research contributions achieved.

Chapter 2 looks at complex wing geometries. It is our goal to extend the design space for wind turbine optimization to new geometries (e.g. swept blades, wing tip modifications). Aerodynamic models based on Blade Element Momentum theory are fundamentally limited to straight, planar rotor blades. Lagrangian vortex models on the other hand do not face this constraint. In this chapter we adopt a Lagrangian vortex model, in the form of an extended and modified version of Prandtl's lifting line formulation (Prandtl, 1918, 1919). Through the analysis of bird wings, featuring a geometry far more complex than most of their engineering complements, we not only provide new insight into some details of bionic drag reduction, but also show that a vortex model is indeed capable of analyzing very complex non-planar geometries, and thus new wind turbine blade shapes as well.

Chapter 3 and **Chapter 4** are concerned with the stochastic modeling of turbulent atmospheric wind in two steps. These two chapters are based on the wind model developed by Veers (1988) and implemented in TurbSim (Jonkman and Kilcher, 2012).

Concerned with turbulent wind and looking at numerical wind turbine analysis we find that interpolation of tabulated wind speed data (a 'block of frozen wind') is often necessary. In Chapter 3 we show that the default choice (linear interpolation) is erroneous – it distorts the spectrum of the wind inflow and thus alters the resulting turbine load statistics. To tackle this issue we introduce a more accurate alternative based on stochastic wind speed increments.

In Chapter 4 we advance Veers's model to a formulation requiring significantly fewer random variables. This step was necessary because the stochastic models used later on (Chapters 6 and 7) have trouble handling a large number of random variables, a fact well known as the 'curse of dimensionality'. For the reduced order model derived here we pick up the ideas from Chapter 3 and again use stochastic increments, this time applied to the random phase angles.

Chapter 5, **Chapter 6** and **Chapter 7** form the core of this dissertation, the derivation and validation of a stochastic method for modeling unsteady wind turbine aerodynamics. We develop this method in three steps:

First, we derive stochastic model for aerodynamic loads driven by unsteady wind. This step is based on the theory of polynomial chaos expansion, as used in previous work and initially introduced by Ghanem and Spanos (1991). However, while previous work was concerned with with stochastic but constant (in time) boundary conditions or system parameters (e.g. unknown but constant temperature, material properties, oscillation amplitudes), we now extend the theory to models driven by stochastic wind input, i.e. a random process correlated in time and space. We start with a basic introduction of the new theory by picking up the lifting line model that was used before (Chapter 2), but simplifying it to a basic one element wing in unsteady inflow. We limit the model to linear equations, neglect spatial correlation, and focus on correctly capturing the (temporal) one-point statistics (i.e. the auto-correlation) of wing loads caused by stochastic inflow. This leads us to two different, but similar stochastic aerodynamic models: the (now time resolved) polynomial chaos model, and the Fourier-Galerkin model. Both models are introduced and validated in

Chapter 5. Moreover, the stochastic projection, used to obtain the coefficients of the stochastic solution, is presented.

In the second step we remain with linear equations, but extend the lifting line model to n spanwise wing elements on a translating blade. The challenge here was to extend the stochastic model such that it correctly captures not only the (temporal) one-point, but also the (spatial) two-point statistics (cross-correlation, covariance, cross-spectrum) of the aerodynamic loads. Based on the Fourier-Galerkin model introduced before (Chapter 5) this step is presented in Chapter 6. Here, we also pick up the results from Chapter 4 to model the wind inflow field with few enough random variables to be manageable for the stochastic model.

In the third and final step we eventually extend the stochastic method to analyzing wind turbine blade loads in rotationally sampled wind field. We include non-linear equations and discover that a polynomial chaos basis is not an ideal choice for the stochastic series expansion, and that the Fourier Galerkin method as introduced in Chapter 5 becomes challenging for non-linear equations. We thus introduce a combination of both previous approaches (polynomial chaos and Fourier-Galerkin), and arrive at a new method. This new methods is uses a stochatic series expansion (like polynomial chaos) but on a stochastic space spanned by multivariate complex exponential functions (like the ones used for Fourier-Galerkin). We call this an *exponential chaos expansion*, and find that now the stochastic expansion collapses to a multidimensional discrete Fourier transform in the stochastic space. In Chapter 7 this new stochastic expansion is introduced and validated. We show that one stochastic solution can produce similar rotor blade load results as multiple solutions from the conventional deterministic model.

To not introduce too much complexity at once we decided to revert to the well established and more simple Blade Element Momentum model (Bladed, 2012; Burton et al., 2011; Hansen, 2008) for this third step. The goal was to show the feasibility of the stochastic model for wind turbine rotor analysis including non-linear effects. This could be achieved with the Blade Element Momentum equations, without having to deal with the extra complexity of vortex models. Moving to a stochastic formulation of Lagrangian vortex equations will eventually follow the same route as described in this chapter for the Blade Element Momentum model. However, this step is left for future work.

Chapter 8 wraps up this dissertation with a summary of the main conclusions drawn from each of the three building blocks as well as an outlook onto future work.

Our long term goal is to arrive at an advanced wind turbine optimization platform. This dissertation presents major steps towards this goal. However, our time is limited – as always. Hence, eventually arriving at a stochastic wind turbine optimization framework, including structural response and controller actions, is left for future work.

1.4 Research contributions

The research presented in this dissertation yielded the following contribution to the current knowledge:

1. We modified and implemented a Lagrangian vortex model to assess unconventional, non-planar wings (Chapter 2).
   (a) We showed that vortex models are capable of accurately assessing aerodynamic lift and drag even for complex and strongly interacting lifting surfaces.
   (b) We studied birds wings and gained insight into bionic methods to enhance wing performance.
2. We developed new stochastic methods applicable to turbulent wind.
   (a) We showed that the current method of linearly interpolating turbulent wind data (available with the common grid resolution) is erroneous. We provided an alternative solution (Chapter 3).
   (b) Current wind models are not suitable for stochastic methods. We developed a better suited alternative (Chapter 4).
3. We introduced new stochastic methods for unsteady aerodynamics.
   (a) We adopted polynomial chaos expansion such that not only random parameters, but also random processes can be dealt with (Chapter 5).

(b) We applied two different kinds of stochastic series expansion to aerodynamic vortex equations in order to analyze wing loads in the stochastic domain (Chapters 5 and 6).

(c) We substituted polynomial chaos basis functions with multivariate complex exponential functions and introduced exponential chaos expansion (Chapter 7).

(d) We analyzed unsteady wind turbine blade loads in the stochastic domain (Chapter 7).

The following chapters will present details to each of these contributions.

Chapter 2

A Lifting Line Model to Investigate the Influence of Tip Feathers on Wing Performance

This chapter was first published as:
Fluck, Manuel and Crawford, Curran: "*A lifting line model to investigate the influence of tip feathers on wing performance*", Bioinspiration & Biomimetics, IOP Publishing, **2014**, 9; DOI: 10.1088/1748-3182/9/4/046017

It was questionable if Lagrangian vortex models are actually a good choice to extend the wind turbine design space from flat rotors with straight blades to unconventional shapes (e.g. with winglets, ailerons, or sweep). In this paper we apply an extended lifting line model (a special type of Lagrangian vortex model) to analyze bird wings. Thus we:

A) proof that vortex model are actually capable to analyze very complex wing geometries.
B) gain insights into bionic ways to decrease induced drag and/ or increase maximum lift.

See Appendix C.1 for further information regarding the C++ code used to generate results for this section.

Abstract

Bird wings have been studied as prototypes for wing design since the beginning of aviation. Although wing tip slots, i.e. wings with distinct gaps between the tip feathers (primaries), are very common in many birds, only a few studies have been conducted on the benefits of tip feathers on the wing's performance, and the aerodynamics behind tip feathers remains to be understood. Consequently most aircraft do not yet copy this feature.

To close this knowledge gap an extended lifting line model was created to calculate the lift distribution and drag of wings with tip feathers. With this model, is was easily possible to combine several lifting surfaces into various different birdwing-like configurations. By including viscous drag effects, good agreement with an experimental tip slotted reference case was achieved. Implemented in C++ this model resulted in computation times of less than one minute per wing configuration on a standard notebook computer. Thus it was possible to analyse the performance of over 100 different wing configurations with and without tip feathers.

While generally an increase in wing efficiency was obtained by splitting a wing tip into distinct, feather-like winglets, the best performance was generally found when spreading more feathers over a larger dihedral angle out of the wing plane. However, as the results were very sensitive to the precise geometry of the feather fan (especially feather twist) a careless set-up could just as easily degrade performance. Hence a detailed optimisation is recommended to realize the full benefits by simultaneously optimizing feather sweep, twist and dihedral angles.

2.1 Introduction

The effect of end-plates on the performance of aircraft wings was studied in early aeronautics (e.g. Nagel (1924); Reid (1925)) and its positive influence has been recognized for at least a half century Hoerner (1952). Classical end plates are simply vertical plates fitted to wing tips. Later refinements used cambered airfoils with toe-in and sweep, leading to the winglets commonly seen on today's passenger aircraft (e.g. Whitcomb (1976); Kirk and Whitcomb (1995)). Modern winglets are essentially vertically-oriented wings implemented to enhance the performance of redesigned or limited-span wings. To mitigate transonic effects sweep is often incorporated. As fuel economy becomes increasingly important and new manufacturing techniques are developed, aircraft manufactures are revisiting winglet technology to further reduce wing drag and hence improve fuel efficiency. Examples are Boeing's new "Advanced Technology" and "Split Scimitar" winglets used with the 737 and 737 MAX families. With both of these new types the winglets are set no longer vertical but at a dihedral angle to the main wing. Birds on the other hand do not have end-plate like vertical winglets but often feature primary feathers, which spread horizontally and vertically to form distinct wing tip gaps. Thus, following the ideas of bio-inspiration, it is intriguing to learn if moving further from conventional winglets to tip feather like winglet fans contributes to further benefits for aircraft wings.

Various analytic and experimental studies have been conducted on the effects of primary feathers and it is understood that these generally reduce induced drag and increase stability for wings of limited span (Lockwood et al., 1998; Norberg, 1990; Sachs and Moelyadi, 2006; Swaddle and Lockwood, 2003; Withers, 1981). From wing drag experiments with Harris Hawks (*Parabuteo Unicinctus*) 10 – 30 % drag reduction was found with tip-slotted primary feathers (Tucker et al., 1995). This reduction is explained by the tip slots breaking up and spreading the tip vortex. Moreover, a clear superiority of vertically spread (Hummel, 1980) and flexible feather-like winglets (Tucker, 1993) over planar wing tip extensions has been reported.

The concept of spread tip feathers and slotted wing tips has been transferred to experimental aircraft designs by equipping wings with multiple (feather like) winglets (Eberhardt, 2011) and a few experimental reports demonstrate that benefits from artificial feather like winglets do exist for aircraft applications. Here again up to 30%

increase in wing efficiency (i.e. lift to drag ratio), up to 20% more lift, or 30% less drag were found for wings equipped with winglets (Cosin and Catalano, 2009; Hossain et al., 2011; Smith et al., 2001). However, the experiments had some difficulty in varying parameters independently, e.g. adding winglets changed the total wing area (Hossain et al., 2011).

The above mentioned studies provide strong evidence that wing tip feathers or tip slotted wings improve the efficiency both for bird wings and aircraft. Although the standard Prandtl lifting line analysis is cited to loosely explain the benefits of wing tip slots (Tucker, 1993; Tucker et al., 1995), profound understanding of the underlying physics has not been provided. Yet, to take full advantage of the benefits wing tip slots offer, it is vital to understand how these devices work and how to best arrange them. Hence this paper aims to contribute towards a better understanding of the processes that lead to a reduction in induced drag for tip-slotted wings. Therefore special attention is paid to the wing's vortex system. The vertical (out of wing-plane) vs. horizontal (in wing-plane) spreading of vorticity by a winglet fan and the influence of the geometric arrangement of the tip feather assembly on induced drag is studied. This extends well beyond the few cases presented by Hummel (1980). It is also recognized that adding winglets or tip slots will increase the viscous drag; hence a viscous drag model in included. The goal is to give fundamental guidelines for bio-inspired design for improved wing performance.

2.2 Calculation method

Considering the goals stated above it was concluded that a full CFD calculation would be too complex with too little flexibility for studying the vortex system of tip slotted wings across a wide range of parameter variations. Even a vortex lattice approach was considered inappropriate for this case, since the prime interest was in spanwise properties such as the spanwise distribution of induced drag and vorticity. Hence the method of choice was an extended lifting line calculation. This method is known to give realistic results for high aspect ratio wings like the ones considered in this study (Schlichting and Truckenbrodt, 2000). The validation case (see Section 2.3) showed that the current model produces good agreement with a tip feathered experimental test case. Moreover, by employing a lifting line model it was possible to focus on the vortex system and its properties, while neglecting airfoil-dependent chordwise quantities such

as chordwise pressure distribution, pitching moment, or center of lift. The calculation routine was constructed such that different wing-winglet configurations could easily be studied.

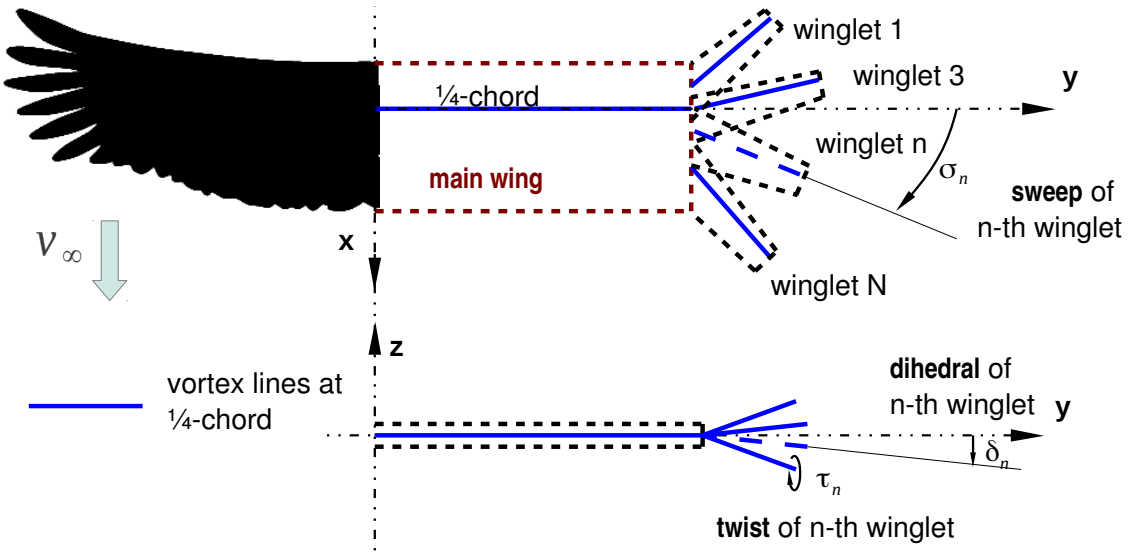

Figure 2.1: The lifting line system (right) compared to a generic bird wing shape (left) including naming conventions and coordinate system.

To suit the tip feather calculations, i.e. representing a main wing and multiple feathers (Figure 2.1), several modifications to the standard lifting line method (see e.g. Phillips and Snyder (2000)) were implemented:

(i) For each lifting surface (i.e. the main wing and each feather) a separate lifting line with its own wake was defined. Each lifting line was discretized by n_s spanwise elements along the 1/4-chord line of the wing or feather respectively. The bound circulation Γ_i of each element i is determined by Kutta-Joukowski's theorem based on the local sectional lift coefficient $c_l(\alpha_e(y), Re(y))$ and the free stream velocity $\boldsymbol{v}_\infty$:

$$\Gamma_i = \frac{1}{2}|\boldsymbol{v}_\infty + \boldsymbol{w}_i|\, c_l\left(\alpha_e(y_i), Re(y_i)\right)\, c(y_i). \tag{2.1}$$

Here $c(y)$ is the chord of the section at the spanwise position y_i, $\alpha_e(y_i)$ is the effective angle of attack of that section resulting from the geometric and the induced angle of attack, and $Re(y_i)$ is the local Reynolds number. Finally $\boldsymbol{w}_i = \sum_j \boldsymbol{w}_{ij}$ is the component of induced velocity normal to the lifting line at element i, obtained as

the sum of all downwash $\boldsymbol{w}_{ij}$ computed via the Biot–Savart law from the influence of each vortex element j at the position i. The local lift coefficients $c_l(\alpha(y), Re(y))$ were extracted from look-up tables (Sheldahl and Klimas, 1981; Doenhoff and Abbot, 1959).

(ii) To include viscous drag into the model, together with its lift coefficient c_l the local sectional drag coefficient $c_d(\alpha(y), Re(y))$ was identified from the same lookup tables for each lifting line element at its respective angle of attack and Reynolds numbers. Thus the total viscous drag of a wing configuration was obtained by integrating the local viscous drag c_d along the whole wing configuration. For this it was critical to supply accurate c_l and c_d tables far into the airfoil's stall region for a wide range of Reynolds number. The latter was necessary, since slim tip feathers often operate in different Reynolds number regimes compared to the main wing, possibly on the other side of the critical Reynolds number. The accurate representation of the post stall behaviour was necessary to correctly model wing-winglet interactions and associated additional drag. Since this component of drag is created by the proximity of two lifting surfaces, it can be understood as drag caused by large induced velocities, which drive wing sections close to the wing-feather junction into stall. Hence, rather than defining empirical induced drag correction factors for the wing-feather connections, the influence of large induced velocities was directly included into the lifting line model. This was achieved by correctly accounting for the increased drag of stalling sections close to the connection point.
Although this approach for capturing viscous drag is based purely on sectional airfoil data and thus neglects spanwise flow, the good agreement of the numerical results with experiments (see Section 2.3) justifies its application. Hence it is understood that this model indeed is a good representation of the viscous drag with both its constituents, profile as well as wing-winglet interaction drag.

(iii) The wake was assembled from chordwise trailing elements and spanwise shed elements (see Figure 2.2) to include the possibility of unsteady calculations. As usual, the strength of the wake elements was determined by Helmholtz' second theorem. For the steady-state analysis presented here, the circulation of the shed elements vanished. To obtain a better representation of the wing and feather geometry, the first segment of spanwise wake is aligned with the wing's trailing edge, while the chordwise bound wake elements connect the lifting line with the trailing edge in the direction of the local chord (Figure 2.2). Downstream of the trailing edge

the wake is aligned with the free stream. Thus, the wing was actually modelled by vortex panels with a chordwise resolution of one panel on each wing or winglet element.

(iv) To avoid numerical instabilities, special care had to be taken at the connection point of two or more lifting surfaces. Here only one common trailing filament is shed (instead of several coinciding ones). The circulation γ_t of that shared filament is set such that $\gamma_t = \Delta\gamma_b$, where $\Delta\gamma_b$ is the difference in circulation of adjacent lifting line elements on the right and left of that connection point.

(v) Equation (2.1) together with wing and wake geometry and the wake strength constitutes the typical extended lifting line non-linear system of equations, which defines the strength of each vortex element Γ_i uniquely. This system was solved via an iterative Gauss–Seidel pseudo time stepping algorithm, where $\boldsymbol{w}_{ij}$ and $\alpha_{e,i}$ are updated after each time step:

$$\Gamma_i^{(n+1)} = \omega \cdot \left(\frac{1}{2} \left| \boldsymbol{v}_\infty + \sum\nolimits_j (\boldsymbol{w}_{ij})^{(n)} \right| c_l(y, \alpha_{e,i}^{(n)}) c(y) \right) + (1-\omega) \cdot \Gamma_i^{(n)} \tag{2.2}$$

For better convergence, an under relaxation factor ω is included. To improve solution times ω was dynamically adapted such that $\omega \in [0.01, 1]$.

(vi) To improve the stability of the method with finer resolution a core radius model as proposed by Van Garrel (2003) was included in the Biot–Savart equations. The validation revealed, however, that increasing the vortex core resulted in inaccurate representation of the close interaction of vortex elements in the tip feather region. This was particularly true for the cases with larger numbers of feathers. Hence the core radius was set to a negligible 0.0001% chord of the main wing to only desingularize the equations, but not compromise the results.

Eventually lift and viscous drag results were obtained directly by summing sectional lift (as obtained from $c_l(\alpha_e(y_i), Re(y_i))$) and drag (as obtained from $c_d(\alpha_e(y_i), Re(y_i))$) at each lifting line element. The induced drag could be directly calculated at the wing from each section's circulation Γ_i and the induced angle of attack α_i. However, this only yielded stable results for planar wing configurations. For highly non-planar configurations a Trefftz plane analysis (Schlichting and Truckenbrodt, 2000) was found

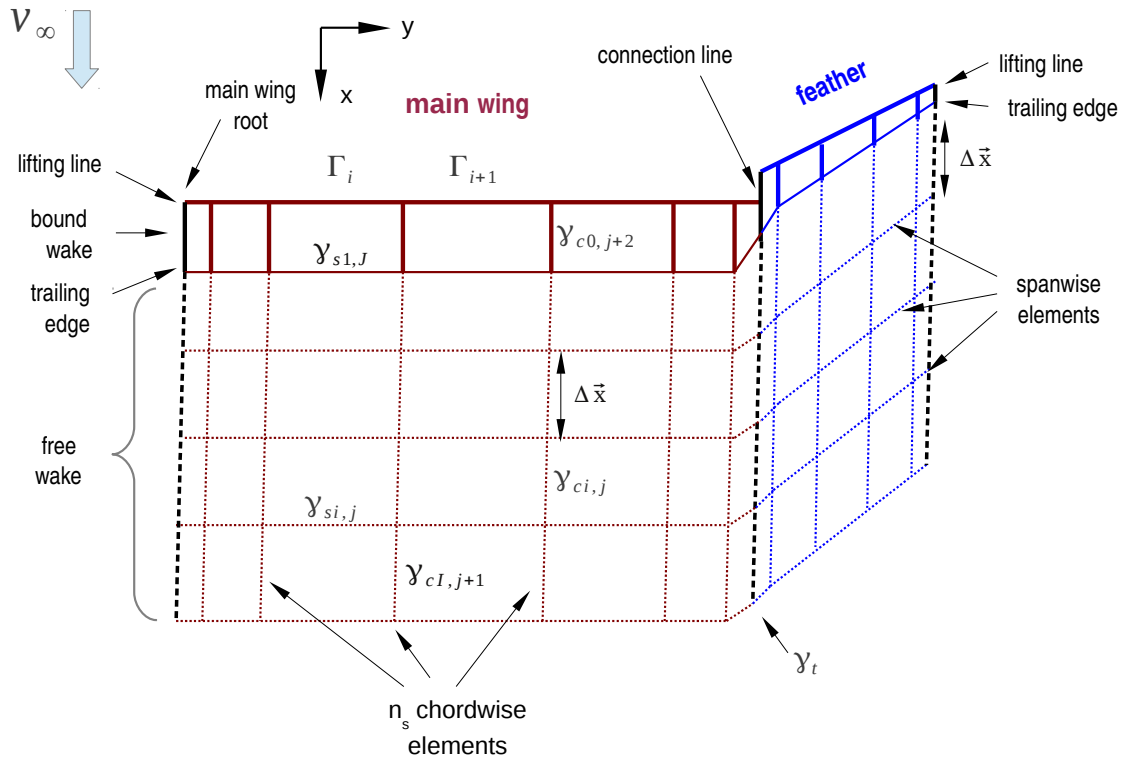

Figure 2.2: The lifting line assembly together with the wake layout in top view. For clarity only the right half wing is shown and only a single tip feather is included.

the better choice to obtain the induced drag component.

The extended lifting line model described above was implemented in a C++ code and used for the numerical experiments. The relative residual R of the equations for wing load distribution was monitored as a convergence criteria. For N_{ll} lifting line elements the relative residual R_n at time step n is defined by

$$R_n = \frac{1}{N_{ll}} \sum_{i}^{N_{ll}} \frac{\Delta\Gamma_{i,n}}{\Gamma_{i,0}} \tag{2.3}$$

where $\Delta\Gamma_{i,n}$ is the change in circulation at element i from time step $(n-1)$ to (n), and $\Gamma_{0,i} = \alpha_i \pi v_\infty c_i$ is the reference circulation of that wing segment from two dimensional theory (chord length c_i, free stream speed v_∞, and geometric angle of attack α_i or $\alpha_i = 1°$ for an element at zero geometric angle of attack).

2.3 Convergence and validation

To assess the quality of the model, the convergence behaviour and two validation cases were studied.

The basic validation of the lifting line model was obtained by comparing results for a wing of elliptical platform. In this case an analytical solution for the lift and induced drag coefficients exists (Schlichting and Truckenbrodt, 2000):

$$C_L = \frac{c_l}{1 + \frac{2}{\Lambda}} \qquad C_D = \frac{C_L^2}{\pi \Lambda}. \tag{2.4}$$

Table 2.1 compares the results for such a wing with flat cross section ($c_l = 2\pi\alpha$), aspect ratio $\Lambda = 5$, wing area $S = 10$ m^2 and angle of attack $\alpha = 0.05$ rad $= 2.9°$ at $v_\infty = 10$ m/s and $\rho = 1.2$ kg/m^2 to the results from the lifting line model with 25 cosine spaced spanwise elements and a quasi semi-infinite wake. As can be seen the presented lifting line calculation reproduces the analytic results for the inviscid case well.

Table 2.1: Comparison of lifting line predictions to analytic results.

	analytic Eq. (2.4)	lifting line	error
C_L	0.224	0.226	0.54%
C_D	0.00321	0.00316	-1.5%

With an increasing number of iterations the model was found to converge in a roughly log-linear fashion in the residual R_n. Figure 2.3, on the other hand, shows the glide ratio results for an increasing number of cosine spaced spanwise elements, for a wing at $\alpha = 5°$ with five tip feathers spread over $\delta = 30°$ dihedral. The wing was discretised consistently with half as many elements on each feather as on the main wing. As can be seen from Figure 2.3 the results are fairly independent of the resolution for about 100 to 500 spanwise elements ($L/D = 33.1 \pm 1.2\%$). Yet, when pushing to very high resolutions, the results become less consistent. Considering the fact that virtually no core radius was used this is not surprising: beyond a certain resolution the control points of some lifting line elements will be very close to the core

of some trailing filaments. As the mutual influence grows with $1/r$, the hyperbolic variation in induced velocity will be increasingly resolved leading to non-monotonic convergence. Fortunately, this region of unstable resolutions could easily be avoided as a large region of resolution-independent results exists. For the following results the resolution was set to 30 elements on the main wing and 15 on each feather (180 elements total).

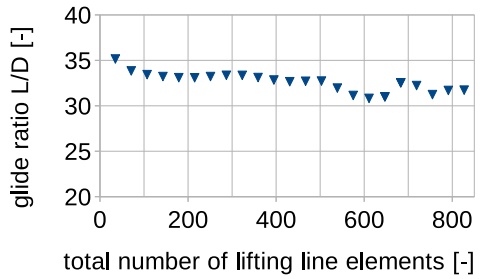

Figure 2.3: Grid convergence for L/D results for a wing with five tip feathers.

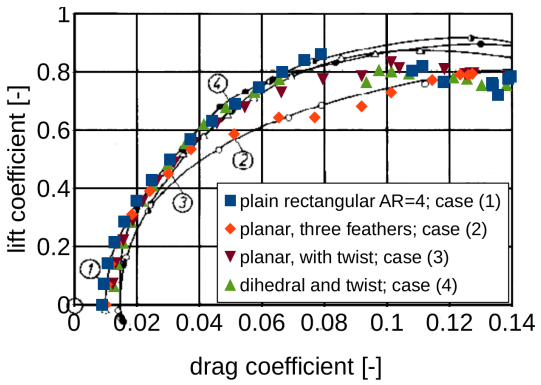

Figure 2.4: Comparison of simulation (marker) to experimental results (Hummel, 1980) for a wing with three feathers.

To further validate the developed extended lifting line model especially for non-planar wing configurations (e.g. wings with winglets or tip feathers), results were compared with an experimental study by Hummel (1980). Four different wing configurations were compared:

(1) a rectangular wing of aspect ratio $AR = 4$.

(2) a planar tip-slotted wing with three feathers, but without any feather twist or dihedral.

(3) a tip-slotted wing with three feathers at $\tau = [-10, -5, 0]^\circ$ twist, no dihedral.

(4) a tip-slotted wing with three feathers at $\tau = [-10, -5, 0]^\circ$ twist and $\delta = [20, 0, -20]^\circ$ dihedral.

As in the experiments a NACA0015 airfoil was used for wing and winglets. The required 2D lift and drag coefficients were extracted from tables published by Sheldahl and Klimas (1981).

As shown in Figure 2.4, below stall the lifting line code reproduces experimental results well. Once the main wing reaches stall (at $C_D \approx 0.08$) the numerical results

diverge from the experimental data. This is, however, not surprising: when the wing stalls, complex three-dimensional flow governs the wing load. Naturally, the model based on two-dimensional input can not fully capture these effects.

The drag at zero lift, on the other hand, is reproduced well. This demonstrates that the chosen model generates the right viscous profile drag (the only drag constituent at zero lift). Moreover, the fact that the increased drag experienced with the plain tip-slotted wing (configuration (2)) is reproduced well by the calculations shows that this model is capable of analysing tip-slotted configurations and captures wing-winglet interaction drag penalties. Closer inspection of the local angles of attack at the tip feathers revealed that the increased drag mainly results from partial stall at the feathers. The non-planar configurations, cases (3) and (4), again matched the experimental results closely. This shows that non-planar and wing-winglet interaction effects are also reproduced well.

Overall, this validation exercise shows that the proposed extended lifting line model is well suited to investigate phenomena and trends influencing the performance of a bird wing like, tip-slotted wings.

2.4 Parametric study results

The presented model allows for quickly studying various configurations of multiple (bird) wing assemblies. Therefore, over 100 cases of different tip feather dihedral, sweep, and twist configuration were analysed. In this section a summary of the results is presented. If not otherwise stated, 30 spanwise elements on the main wing and 15 spanwise elements on each feather were used for the computations. The wake was modelled with straight line elements extending 500 chord lengths downstream. The Trefftz plane was located half-way along the wake. Convergence was assumed to be reached at a residual $R_n < 10^{-5}$. Depending on the number of feathers, computing the results for one configuration at one angle of attack took a few seconds to a few minutes on an Intel i5 quad core processor with four cores in parallel. Since this study is inspired by bird wing design, primarily small aircraft (possibly unmanned aerial vehicles - UAV) at sizes only slighter bigger than birds were investigated. The Reynolds number was set to $Re = 1.3 \cdot 10^6$, based on the main wing chord. The attempt to study lower Reynolds numbers was abandoned, since no adequate airfoil

coefficients were available.

An elliptic load distribution is known to give best performance (i.e. minimum induced drag) for planar wings. Hence, the results obtained for two different bird wing configurations (rectangular main wing with two and five tip feathers respectively) are compared to a wing with elliptic chord distribution with $b = 10$ m span and aspect ratio $\Lambda_e = b^2/A = 10$ (A denoting the wing area). For both bird wing cases the feather length was set to $b_f = 1$ m with a feather taper ratio $\lambda_f = 0.5$, while the main wing length was reduced to $b_m = 8$ m. Thus the total span (i.e. span of the main wing plus double the feather length) was held constant $b_t = b_m + b_f = 10$ m. Moreover, to be able to compare the configurations on a similar basis, the main wing chord c_m was set such that total aspect ratio $\Lambda = b_t^2/A_t = 10$ (A_t now denoting the total wing area of main wing and all feathers) did not change either. NACA63_2-415 airfoil data from Doenhoff and Abbot (1959), extrapolated to $\pm 180°$ with NREL's AirfoilPrep (2014), was used for all lifting surfaces.

In the following, the results for sequentially varying the feather dihedral, sweep, and twist angles (see Figure 2.1) are presented. The connection points $x_{f,i}$ of each feather to the main wing were spread along the main wing tip chord c_m according to:

$$x_{f,n} = x_m + \left(0.7 \cdot \frac{n-1}{N-1} - 0.15\right) c_m \qquad \text{for} \quad n \geq 2 \tag{2.5}$$

Here x_m denotes the terminal point of the main wing lifting line at $0.25c_m$. No vertical stacking was introduced. However, in the case of non-zero angle of attack the feathers appear offset with respect to the inflow as a result of the inclined main wing chord line (see front view in Figures 2.5 - 2.6).

In the following sections, both wing performance C_L – C_D polars and glide ratio (L/D – α) curves are presented to evaluate performance.

2.4.1 General remarks on tip feathers

Splitting a wing tip into several feathers first of all introduces a viscous drag penalty and distorts the ideal elliptical load distribution (Figures 2.5 - 2.7). For very low wing loadings these effects always resulted in decreased glide ratio L/D. At medium wing

loadings some feather configurations were found to overcome the increase in induced drag to perform better than the planar elliptical wing. At very high wing loadings the L/D of the tip feathered wings often decreased again. For all cases L/D gains were more pronounced with five feathers. On the other hand, the maximum achievable lift ($C_{L,max}$) was usually higher with fewer feathers. Moreover, some cases (especially with fewer feathers) seem to have a beneficial effect on post-stall performance. Figures 2.5 - 2.7 show that the post-stall decline in lift is often less steep for the feathered wings than for the elliptic baseline case. This indicates that the feathers help mitigate stall. The slower onset of stall provides an early warning and helps to fly transient manoeuvres in partial stall. This may reduce the demands on flight control. The increased $C_{L,max}$ increases manoeuvrability by extending the flight envelope to higher wing loadings. All this indicates that, for a given mission profile, there might be an ideal number of feathers. Below this the L/D benefits of more feathers are not fully exploited; with too many feathers the reduction of $C_{L,max}$ is too disadvantageous and the wing becomes overly susceptive to detrimental feather effects.

2.4.2 Twisted tip feathers

Twisted feathers deteriorated wing L/D significantly if all feathers were set to the same twist angle (constant along each feather), see Figure 2.5. However, $C_{L,max}$ was increased in these cases and the post-stall decline in lift is less steep than for the elliptic wing.

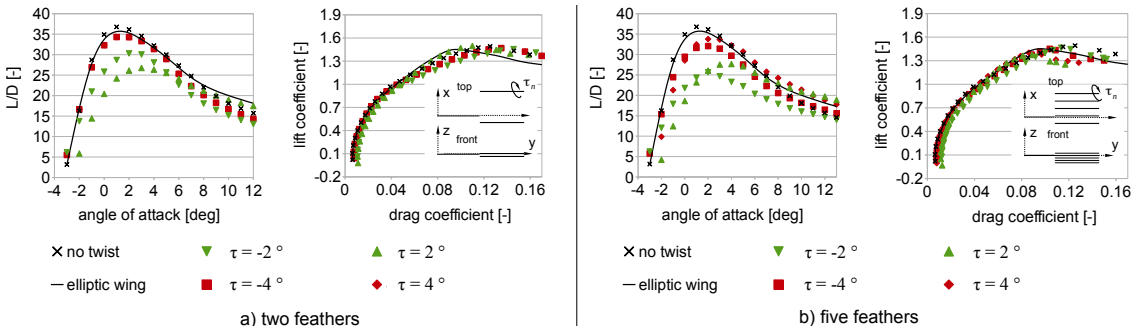

Figure 2.5: Glide ratio and $C_L - C_D$ polars for an elliptic wing vs one with twisted feathers; same twist τ for all feathers.

Results for twisting each of N feathers at an individual twist angle

$$\tau_n = \tau\left(-1 + \frac{2n}{N}\right) \tag{2.6}$$

are shown in Figure 2.6. In contrast to setting all feathers to the same twist angle (Figure 2.5), successively increasing the twist at each feather ($\tau = [-10...10]°$ and $\tau = [-5...5]°$) improves the wing glide ratio for most angles of attack. However, the maximum glide ratio still slightly decreases. Moreover, a clear loss in post-stall lift is now found.

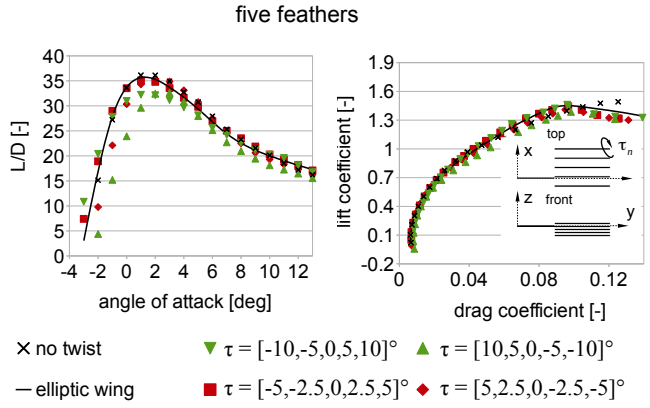

Figure 2.6: Glide ratio and C_L – C_D polars for an elliptic wing and one with five twisted feathers; different twist τ_n for each feather (increasing front to back).

2.4.3 Swept tip feathers

Several configurations with N feathers swept forward and aft were tested as well. Each feather was set such that its sweep was $\sigma_n = \sigma\left(-1 + \frac{2n}{N}\right)$, see Figure 2.1. However, moderate feather sweep had little influence on the wing L/D and the the best glide ratio was always found for the straight arrangement with all feathers parallel. This is reasonable, since swept feathers only reduces the effective aspect ratio, while according to Munk's theorem (Munk, 1923) in-plane stagger does not change the load distribution nor the induced drag. Therefore, it is unlikely that the birds' tip feather sweep, which is commonly seen in nature, is directed toward an improved glide ratio. As shown by Sachs and Moelyadi (2006) though, sweep can be important for yaw stability, and as suggested by others (Withers, 1981; Hummel, 1980; Tucker, 1993) might be important for for roll stability as well.

2.4.4 Tip feathers with dihedral

Spreading the feathers in dihedral can bring significant benefits regarding the wing performance. For the numerical experiments the dihedral angle δ_n of each of the N feathers was set such that:

$$\delta_n = \delta \left(-1 + \frac{2n}{N} \right) \tag{2.7}$$

Although the viscous drag penalty associated with adding tip feathers reduces wing performance at very low wing loadings here as well, L/D increased at some dihedral angles δ (see Figure 2.7). Again, the effects are more pronounced for five feathers: at $\delta = \pm[0, 30, 60]^\circ$ the maximum achievable L/D exceeds the peak L/D of the elliptic wing considerably. But again, the maximum lift achieved with five feathers is less than with two. Moreover, for two feathers $\delta = \pm 30^\circ$ yields more L/D than $\delta = \pm 60^\circ$.

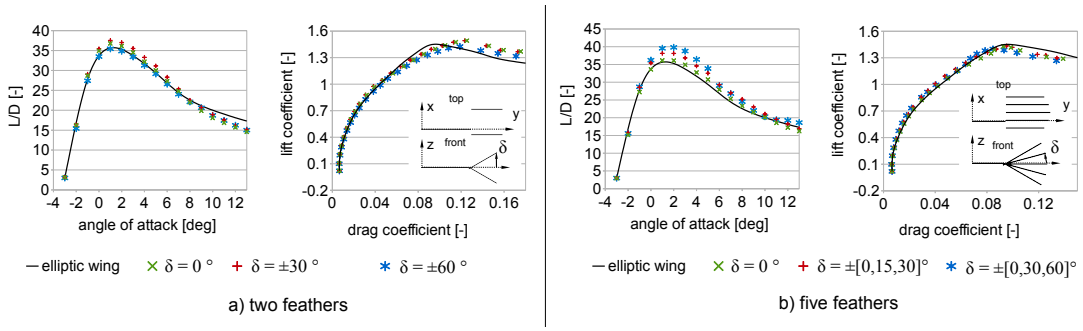

Figure 2.7: Glide ratio and C_L – C_D polars for an elliptical wing (baseline) and different feather dihedral angles δ.

The maximal achievable glide ratio as a function of dihedral is analysed next. For passenger aircraft the wing span is usually restricted by the established airport infrastructure and/or structural limitations; for UAVs transportability often limits the span. For birds, the required agility given a certain habitat constrains the wingspan. Hence, the projected span b_p (i.e. the horizontal distance from wing tip to wing tip) is now kept constant, instead of the aspect ratio as above. For two feathers this meant increasing the main wing span (and accordingly the wetted wing area A_t) with increasing feather dihedral such that $b_m = b_p - b_f \cos\delta$. For five feathers the middle feather always remains horizontal and projected span and total wing area are constant independently of feather dihedral. The geometry of each feather was kept the same as above. Figure 2.8 shows the maximum glide ratio achieved for a wing with two and five feathers per side, tilted according to equation 2.7 from $\delta = 0^\circ$

(planar) to $\delta = \pm 90°$. Here $\delta < 0$ indicates the leading feather is angled upwards, while $\delta > 0$ indicates the leading feather is angled downwards. The L/D curves were evaluated at $\Delta\alpha = 0.2°$ increments in angle of attack. To decrease computational time and to avoid instabilities in the solution at high dihedral angles, the spanwise resolution was reduced to 15 lifting line elements on the main wing and five on each feather.

It was already shown that a wing with two feathers (which at $\delta = \pm 90°$ dihedral resemble conventional winglets) reaches its maximum L/D at $\delta < 60°$, not at $\delta \approx 90°$ as with the usual winglets on aircraft. Figure 2.8 reveals that for two feathers even with constant projected span the best L/D is achieved at $\delta \approx 20°$. For five feathers, on the other hand, the glide ratio actually increases continuously with increasing dihedral. The reason for this is attributed to the complex processes of the vertical spreading of vorticity around the wing tips. Moreover, for the two feather wing the wetted area A_t increases faster with dihedral than the projected (i.e. the lift generating) area A_p. Thus an optimum in dihedral seems reasonable. For five feathers, on the other hand, it is interesting to note that increasing dihedral and thus reducing the lift generating area still increases L/D. Again, the reason for this can be found in the positive effects of vertically spreading tip vorticity, where the larger spacing between individual feathers at larger dihedral seems beneficial. The $L/D_{max} = 43.2$ of this configuration is 21% greater than the maximum glide ratio ($L/D_{elliptic,max} = 35.6$) of the elliptic wing. This increase in performance may appear overly large, but is actually within the range found by others in previous experiments (Tucker et al., 1995; Smith et al., 2001).

Figure 2.8 shows a direct comparison of the performance gains achievable by two vs. five feathers. The trend found above is confirmed: five feathers can achieve significantly more gain in L/D than two feathers. But figure 2.8 also reveals that this extra gain is only reached once the feathers are spread over a sufficiently large dihedral. For both cases differences between angling the leading feather upwards ($\delta < 0$) or downwards ($\delta < 0$) are present, but negligible.

2.4.5 Circulation distribution

To assess the mechanisms behind wing performance improvements with tip feathers Figure 2.9 shows an example for the non-dimensional circulation distribution at the right

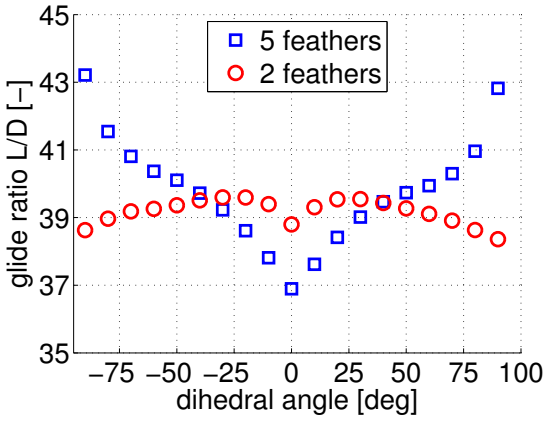

Figure 2.8: Tip feathers angled from $\delta = 0°$ to $\pm 90°$ dihedral at constant wing span.

wing tip as obtained from Equation 2.1. The wing with the best glide ratio (five tip feathers with $\delta = 60°$, no sweep, no twist) was analysed at $\alpha = 2°$ angle of attack. The same feather geometry as above was used [4]. For comparison the circulation distribution of a planar wing with similar tip taper ($\lambda_{tip} = 0.5$) as the case with feathers is included.

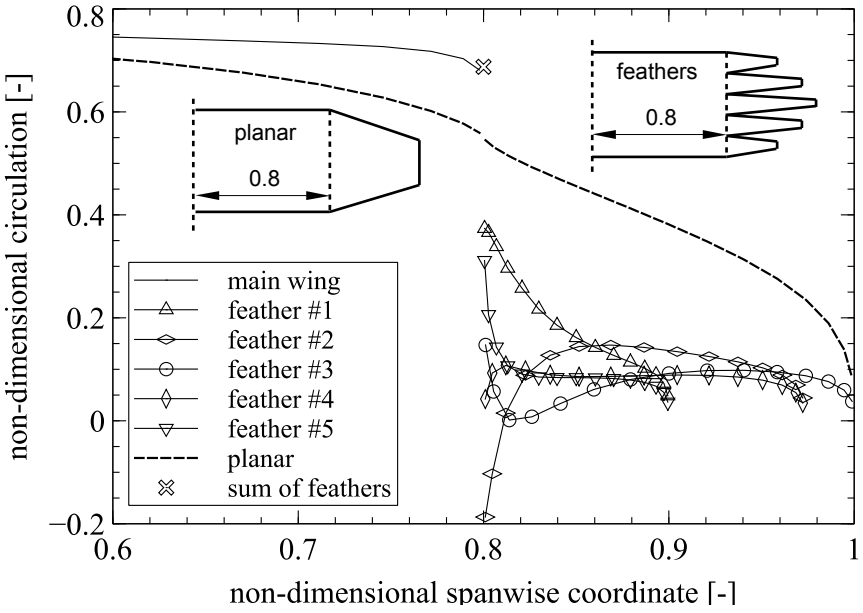

Figure 2.9: Lift distribution on a wing with five tip feathers ($\alpha = 2°$, $\delta = 60°$).

The effect of mutual up-/downwash influences between feathers and the main wing is clearly evident. While the circulation on the planar wing decays slowly towards

[4]Note that with $\delta = 60°$ the feathers appear of different length only in the projection of Figure 2.9, while they are actually of equal length $b_f = 1$ m.

the tip (mainly due to the decreasing chord), the wing with feathers experiences a significant increase in circulation on the main wing due to the upwash from the leading feathers. The strong gradient in circulation at the feather roots indicates that here strong root trailing vortices are shed. These feather root trailing vortices in turn induce a strong influence on the feather's load distribution and cause very different circulation levels on the different feather roots. Depending on the exact wing and feather geometry this can cause an increase in L/D or maximum lift.

Although all the shed tip and root trailing vortices strongly influence the load distribution on the wing, it is important to note that in this case the combined root circulation of all feathers (the cross mark in Figure 2.9) is almost equal to the circulation at the end of the main wing. According to Helmholtz' second theorem this implies that the sum of all vorticity trailing from the main-feather connection point vanishes behind the wing. This, in turn, is important since additional vorticity shed at the connection point would lead to increased induced drag.

While tip feathers increase the wing loading (i.e. the circulation) on the inner parts of the wing, the tip load on the feathers is in-turn reduced by splitting the wing up into distinct feathers. This leads to weaker tip vortices and thus less induced drag.

However, it is vital to acknowledge that all three effects mentioned above – increased main wing load, no extra shed vorticity and reduced load at the tips – are strongly dependent on the precise wing geometry. While the configuration presented in Figure 2.9 is the best performing configuration found in this parametric study, other configurations resulted in different circulation distributions.

2.5 Discussion

The results of the current study point to physical reasons for the evolution of tip feathers:

- ◇ Stall mitigation reduces the complexity of flight control and reduces sensitivity to flight control errors.
- ◇ The increase in maximum glide ratio with tip feathers spread vertically improves gliding capabilities even under wing span limitations (imposed by habitat or inertia constraints e.g. for take-off capabilities)

- ◇ The increase in maximum achievable lift at high wing loads seems particularly valuable when occasional high manoeuvrability is required (e.g. for raptors).

Since this study was carried out to shed light on the biomimetic applications of tip feather devices, a more throughout discussion of the implications of tip feather aerodynamics for birds is left to the biologists' examination.

For aircraft wing design the significant increase in wing efficiency L/D (21% over the value for an elliptic wing) is the most important finding. However, an increase in L/D was never associated with an increase in maximum lift. While birds combine both, increasing L/D and maximum lift by adjusting their tip feather geometry to the instantaneous flight conditions, aircraft are usually limited to one fixed tip configuration. As a result, further investigation into flexible or actuated tip feathers seems a promising avenue for fully exploiting the potential benefits of tip feathers.

Based on numerical studies, Smith (1996) reported considerable wake interaction for highly non-planar wakes and found another 6% efficiency increase for relaxed wake calculations over fixed wake ones. Additional tests were run with relaxed wakes in the current model, using moderate length wake elements ($\approx 10\,\%$ main chord). These investigations did not, however, reproduce the influence found by Smith. It is possible that discretizing the wake with much finer elements might reveal more wake relaxation influence. As this would have increased the computational effort significantly and thus would have compromised the ability to investigate various different winglet configurations, no further work in this direction was pursued.

Although the chosen lifting line model neglects most effects of chordwise load distribution, the validation against experimental results showed that this model is reasonably capable of reproducing tip feather effects and wing-winglet interaction, as well as viscous drag components. Moreover, with its fast solution times of only a few seconds to minutes, the model is perfectly suitable for preliminary design studies and to investigate fundamental trends. This enabled a study of over 100 different configurations. Considering the huge and complex design space even this represents only a few isolated samples. In order to find the "best" configuration under the constraints of a given flight mission clearly the effort of a full optimisation is required. However, since the primary scope was limited to an initial investigation of possible benefits, important trends, and physical explanation of tip feathers, this optimisation

effort is postponed to future work.

2.6 Conclusions

Based on an extended lifting line model, the performance of tip slotted wings, similar to bird wings equipped with distinct wing tip feathers, was studied in a set of numerical experiments. It was shown that introducing multiple tip feathers, vertically spread through varying dihedral to create a non-planar tip slotted wing, can be beneficial. Gains were found in wing efficiency (i.e. the obtained glide ratio L/D), stall behaviour, and/ or maximum achievable lift. Five main conclusions regarding a beneficial layout of tip feathers can be drawn:

1. More feathers only seem beneficial if they are spread far enough in dihedral, i.e. if additional feathers are not packed into the same volume but spread out further.
2. There exists a feather dihedral with a maximum glide ratio. For two winglets this is *not* $\approx 90°$ as common winglet design suggests.
3. Twist is a very sensitive parameter: ideally twist would be adjusted to the point of operation to ensure maximised benefits. Only with twist varying for each feather (τ successively increasing from forward to aft feathers) cases of slightly increased max L/D were found. Yet, twist may have further benefits in combination with dihedral.
4. A simultaneous increase in maximum lift and maximum glide ratio L/D with the same configuration was never found. This suggests difficulties finding an ideal wing for a variety of different flight requirements without active geometry control.
5. Sweep was never found to reduce drag or increase lift. However, sweep might be necessary for a physical wing design to arrange an increased number of feathers appropriately. Moreover, other resources suggest sweep may increase stability and is of course important for higher Mach number flight.

As an example the circulation distribution over the wing with the highest glide ratio was studied. From this examination of circulation distribution the performance gains found could be attributed to the tip feathers increasing the main wing load and decreasing the tip circulation while not shedding extra vorticity from the main-feather junction. Overall, the feathers were found to reduce the total shed vorticity.

Although only a few wing configurations were analysed in the current work and no optimisation was performed, it was shown that for certain configurations (e.g. five tip feathers spread over $\delta = 90^\circ$ dihedral) a 21% efficiency improvement over an elliptic wing of same aspect ratio but with no tip feathers was achieved. This number is expected to increase further when actually optimising a specific feather geometry.

Chapter 3

Minimizing Errors in Interpolated Discrete Stochastic Wind Fields

This chapter is a slightly corrected version of a paper first published as:
Fluck, Manuel and Crawford, Curran: "*Minimizing Errors in Interpolated Discrete Stochastic Wind Fields*", Journal of Wind Engineering and Industrial Aerodynamics, **2016**, 152, 15–22; DOI: 10.1016/j.jweia.2016.02.007

In this paper we realize that the method currently used to map tabulated wind speed data, e.g. an (earth fixed) 'block of frozen wind', onto rotating blades is erroneous. As a remedy we introduce a new method based on stochastic wind speed increments.

See Appendix C.2 for further information regarding the MATLAB code used to generate results for this section.

Abstract

For many unsteady processes (e.g. turbulent wind, electricity demand, traffic, financial markets, space physics, etc.) data is only available at discrete points, be it due to data storage or data gathering limitations. However, derived forms of that data are often used in further studies where the discretization may be different from the discretization of the original data. This paper addresses the question of how to obtain values between discrete data points, for example when sampling turbulent wind. Linear interpolation is often the standard answer. Yet, it is shown that this is a poor choice for unsteady processes where the sample step size is significantly larger than the fluctuation scale. An alternative employing probability density functions of data increments is suggested. While this new method does not require much more effort than linear interpolation, it yields significantly more accurate results. Unsteady wind is used to exemplify this: turbulent wind speeds on a (rotating) wind turbine blade are synthesized from a coarse data grid via the introduced method of wind speed increments. Thus the superiority of the presented approach over linear interpolation is demonstrated – with important implications for blade load and power output computations.

3.1 Introduction

In engineering application we often have to deal with unsteady, highly fluctuating processes, e.g. turbulent atmospheric wind, urban electricity demand, local traffic volume, financial markets, space physics, etc. Due to limitations in data handling and/or storage capacity often a full time series of the process under investigation is not available. Instead, only incomplete data sets at discrete points are at hand. However, these data sets are regularly used as input for further analysis and often data values between two sample points are needed. To solve this task, interpolation based on deterministic, continuous, and possibly multivariate algebraic or sometimes trigonometric polynomials, with the number of variables depending on the considered problem (one or several interpolation dimensions), is the common solution (Phillips, 2003; Steffensen, 2006; Mastroianni and Milovanovic, 2008). Linear interpolation is the most basic (and very widely used) example of this kind of interpolation in a one-dimensional space.

However, if the interpolation time and/ or length scales are significantly larger than the signal's fluctuation scale these interpolation schemes become erroneous. In fact, in these cases conventional interpolation with continuous functions acts as a low-pass filter. Thus it results in a reduced variance σ^2 of the interpolated signal, i.e. a reduced likelihood of extreme events, and consequently a distorted spectrum. Fig. 3.1 illustrates this. A set of $N = 100$ data points, labelled 'original process', is considered as a generic example of some unsteady, highly fluctuating process with a short fluctuation scale. The N points were generated independently and standard normal distributed (variance $\sigma^2 = 1$). If this process is reconstructed via linear interpolation from a set of ten equidistant sample points, much further apart than the fluctuation scale, the resulting process (labeled 'interpolated') is obviously considerably smoother, and the signal variance drops to $\sigma^2 = 0.67$ [5]. Clearly this results in an error when the interpolated data set is used in further analysis.

Although a simple Gaussian process was used here for illustration, linear interpolation obviously has the same effect on various kinds of weakly correlated processes with short fluctuation scales. Switching from linear to higher order interpolation methods might mitigate these effects and potentially even conserve the statistical

[5] For clarity only a short process is shown in Fig. 3.1. However, to achieve statistically stable results $N >> 100$ data points were considered.

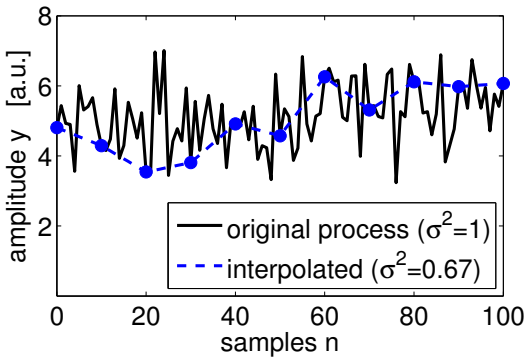

Figure 3.1: Comparison of a generic highly unsteady process and the resulting data set after interpolation between discrete sample values.

moments (see e.g. Mastroianni and Milovanovic's discussion on moment-preserving approximation (Mastroianni and Milovanovic, 2008)). However, this will not solve the problem in principle, because these methods still use continuous functions, which lead to a strongly correlated result not adequate for highly fluctuating processes.

To overcome this limitation Barnsley (1986) and Barnsley and Harrington (1989) introduced generalized polynomial interpolation. This method is based on fractal functions and tailored for interpolating highly "wriggly" (Barnsley, 1986) functions, such as the elevation profiles in mountain ranges, stock-market indices, or the profile of cloud tops. However, the method lacks flexibility concerning conditions on the interpolation points and is mathematically rather involved (Bouboulis, 2012). Hence, even 30 years after its introduction fractal interpolation is not used widely in the engineering community (Navascués et al., 2014), while linear interpolation remains the default method.

To limit the scope of this paper, we focus on wind turbine engineering. Here, linear interpolation certainly is the most common strategy to obtain local blade inflow velocities from a turbulent wind field pre-computed from an industry standard spectrum. For example, the two major wind turbine simulation tools, *FAST* (Jonkman and Buhl, 2005) and *GH Bladed* (Bladed, 2012), employ piecewise linear interpolation to map from discrete wind speeds on a regular spatial grid to blade-local velocities. Based on Taylor's frozen turbulence hypothesis (see e.g. Panofsky (1984)) these tools interpolate local apparent wind speeds linearly onto the rotating blades at each time step, while an a priori computed block of discrete frozen wind is stepped through the rotor disc. However, as just discussed in general (cf. Fig. 3.1), for a highly unsteady processes (with short correlation scales) such as turbulent wind, this approach can

introduce a significant error into the statistical properties of the data set.

The time record of turbulent wind speed data in the atmospheric boundary layer can be interpreted as a stochastic field. Here the cross-correlation C is the indicator of what we called fluctuation length scale in the general case above. For the wind speed signals at any two points P_i and P_j the cross-correlation C is defined via the cross and auto spectrum of the two signals, S_{ij} and S_{ii}, respectively (Burton et al., 2011):

$$C(f, \Delta r) = \frac{|S_{ij}(f, \Delta r)|}{S_{ii}(f) S_{jj}(f)} \tag{3.1}$$

Obviously C is a function of the signal frequency component f as well as of the the distance Δr between P_i and P_j. The commonly used wind turbine design standard IEC 61400-1, Ed. 3 (2005) gives an empiric approximation equation for $C(f, \Delta r)$. The values decay quickly with increasing Δr, e.g. for 10 m/s wind speed $C(f{=}1$ Hz, $\Delta r{=}2$ m$) = 0.091$, and $C(f{=}1$ Hz, $\Delta r{=}5$ m$) = 0.024$. Hence, even for small distances linear interpolation between neighboring wind speeds means averaging two weakly correlated events and thus smoothing the data. The consequences are as discussed above (Fig. 3.1).

Veers (1988) was already aware of this loss of variance. Based on the cross-correlation function between the two support points of given data he derived an analytical expression for the resulting variance error. As remedy he suggests without further details to add white noise to the interpolated data to recover the lost variance. Although this method can restore the desired variance it distorts the power spectrum by neglecting auto-correlation – an important characteristic for wind speed data and other physical processes.

A better method, which is based on stochastic increments and preserves both the signal's variance and spectrum, will be introduced in the next section. Rather than deriving yet another mathematically rigorous but practically too complicated interpolation theory, our goal was to devise a simple engineering method that provides a solution to the interpolation problem and an improvement over linear interpolation as currently used in wind turbine engineering, but without digging too deep into probabilistic math.

The resulting method will be presented for the one dimensional case first in general

(section 3.2.1), such that it can be easily transferred to any unsteady, weakly correlated/ highly fluctuating (one dimensional) process in any field. Section 3.2.2 will provide a graphic application example: the method will be extended to higher dimensions and applied to a specific interpolation problem in wind turbine design. Results will be presented in section 3.3, and compared against linear wind interpolation, the current status-quo, which is used baseline case here.

3.2 A new interpolation strategy: stochastic increment interpolation

While linearly interpolating (as well as interpolation based on continuous functions in general) does not always yield 'good' results, reducing the interpolation length down to the correlation length through finer spacing of known support points, or even obtaining the whole unsteady process at each required point from its fundamental statistical properties (e.g. probability density function, spectrum, spatial and temporal correlation, etc.) is often too tedious (Rai et al., 2015). For turbulent wind, for example, the computational effort for simulating the field rises with the fourth power of the number of grid points (Bladed, 2012). Moreover, the location of required inter-grid points is often not known a priori. Hence some kind of interpolation is inevitable. As an alternative to linear interpolation the use of data increments is suggested. This section will first outline the method in general. Subsequently we apply it to the specific example of wind interpolation.

3.2.1 Increment interpolation - general method

The process of increment interpolation is summarized in Fig. 3.2 for a generic data set $y(n)$ sampled at every tenth point (indicated by blue dots in Fig. 3.2a).[6]

For two points of the data set $y(n)$ a fixed distance r apart, the data increment is defined as:

$$\Delta y_r(n) = y(n+r) - y(n) \tag{3.2}$$

[6] Note that in general the process $y(n)$ can be sampled in space or time or combined in space and time (as shown in next section).

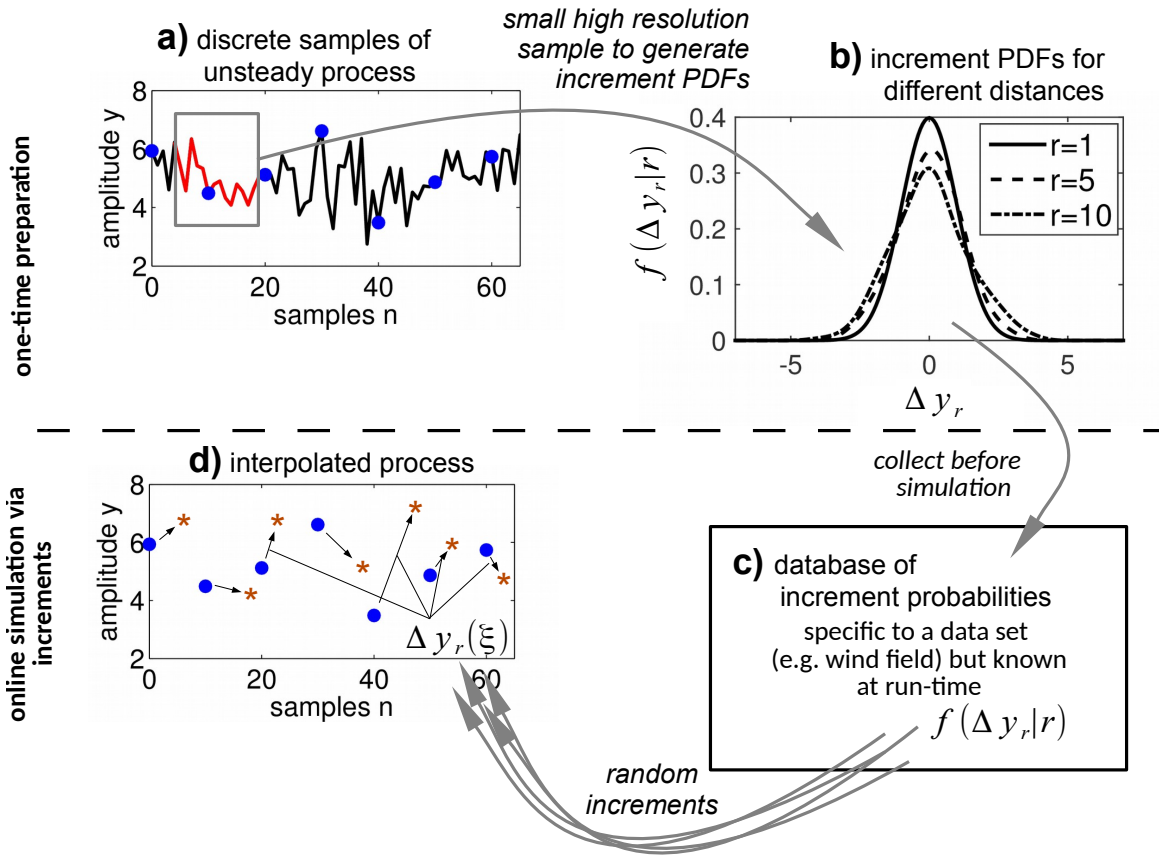

Figure 3.2: Flow chart for interpolating an unsteady process with random increments.

For an unsteady process and a given r, $\Delta y_r(n)$ is a function of the sample index n and is at first hard to grasp. Yet, for a stationary stochastic process such as turbulent wind Δy_r can also be interpreted as a stochastic variable. To indicate this we write $\Delta y_r(\xi)$, where ξ is a random variable. As discussed by Boettcher et al. (2007), for each distance r a conditional probability density function (PDF) $f(\Delta y_r|r)$ can be found. Each $f(\Delta y_r|r)$ then represents the likelihood of a certain increment Δy_r for a specific distance r (Fig. 3.2b). If $f(\Delta y_r|r)$ cannot be constructed analytically from the original process an alternative option is extracting an estimate from a short high resolution sample of the data (see e.g Simonoff (1996), indicated in Fig. 3.2 a→b). Eventually all the PDFs for each distance r can be combined into one joint PDF $f(\Delta y, r)$ of data increments. For interpolating a discrete data set of low resolution the joint increment PDF can then be used to simulate a (random) data increment $\Delta y_r(\xi)$ of appropriate probability for any required interpolation distance r. Various statistical

methods are available for this step. For our example we cast the increment PDFs into cumulative probability functions (CDFs) $F(\Delta y_r)$ and use the inverse transform method (as e.g. described by Kroese et al. (2011)) to obtain a random $\Delta y_r(\xi)$ for any required distance r from a uniformly distributed random variable ξ. This $\Delta y_r(\xi)$ now represents the increment from a point R of known data to an arbitrary intermediate point Q a distance $r = \overline{RQ}$ away. Eq. 3.2 can now readily be used to construct data at *any* intermediate point (indicated by stars in Fig. 3.2d):

$$y(n + r) = y(n) + \Delta y_r(\xi) \tag{3.3}$$

It is important to note that although this method does not reproduce the original process exactly it conserves the statistical properties by generating random data increments of correct probability. Moreover, using random increments does not require much more effort than linearly interpolating, since only step c→d (Fig. 3.2) has to be performed during the simulation, while steps a through c are calculated only once and in advance.

3.2.2 Increment interpolation applied to atmospheric wind

Turbulent wind is one example where data cannot easily be described by a continuous analytic function. Therefore data points must be recorded and supplied to further analysis as samples discrete in space and time (Rai et al., 2015). Moreover, for wind turbine analysis the instantaneous (turbulent) wind speed u at varying blade positions has to be found. For most instances the blade is not aligned with the grid and hence inter-grid values of wind speeds have to be obtained. The standard procedure as described by Moriarty and Hansen (2005) linearly interpolates the on-grid values to the required inter-grid positions. However, as discussed in Section 3.1 this distorts the wind statistics, which are important for turbine load and fatigue analysis as well as power output predictions (Wächter et al., 2012; Calif and Schmitt, 2012; Milan et al., 2013; Calif et al., 2013). This deficit can be overcome by applying wind speed increment interpolation instead.

Key to using wind speed increments is obtaining the joint PDF of the wind speed increment Δu. While the generic (one-dimensional) process from the previous section provided a simple way to introduce the suggested method, turbulent atmospheric wind is a three dimensional field correlated in space and time. To preserve the (auto

and cross) correlation Eq. 3.3 must be extended to include both, the space and time components. To achieve this an inverse distance average is combined into the (one dimensional) wind speed increment interpolation. Thus we arrive at a higher dimensional interpolation yielding the wind speed u_i at intermediate points as shown in Fig. 3.3[7]:

$$u_i(t_j) = \frac{\frac{a}{\Delta x_t}\left(u_i(t_{j-1}) + \Delta u_t(\xi_j)\right) + \sum_{k=1}^{K}\left(\frac{1}{\Delta x_k}\left(u_k(t_j) + \Delta u_k(\xi_j)\right)\right)}{\frac{a}{\Delta x_t} + \sum_{k=1}^{K}\frac{1}{\Delta x_k}} \tag{3.4}$$

Here the sum extends over K neighbors in space, a is a weighting factor discussed later, $u_k(t_j)$ is the wind speed at the neighboring grid point $\#k$ at the current time instance t_j, $u_i(t_{j-1})$ is the interpolated wind speed at the intermediate point at the previous time step, Δx_k and $\Delta x_t = \bar{u}\Delta t$ are the interpolation distances in space and time respectively. To preserve the statistics the wind speed increments $\Delta u_k(\xi)$ and $\Delta u_t(\xi)$ now have to be generated from two separate conditional distribution functions $f(\Delta u_k | r = \Delta x_k)$ and $f(\Delta u_t | t = \Delta t)$ respectively.

It is important that all increments are generated from one random number ξ_j for each time step, because otherwise Eq. 3.4 would again result in averaging of uncorrelated data. Also note that Eq. 3.4 reduces to a tri-linear interpolation in space and time with the random increments $\Delta u_k(\xi)$ and $\Delta u_t(\xi)$ vanishing. Hence, the increment interpolation can indeed be understood as an stochastic extension of the conventional linear interpolation.

To adequately represent the auto- and cross-correlation a weighting factor a is introduced to shift the influence between the spacial and temporal neighbors. Since the correlations are functions of the fluctuation frequency (e.g. IEC 61400-1, Ed. 3 (2005); Veers (1988)), the factor a has to be adapted with the interpolation time step Δt. Fig. 3.4 shows the root mean square of the relative error $\Delta\sigma$ between the standard deviation of the original process and the interpolated one obtained from nine different interpolation points. To get statistically stable results the average of ten realizations

[7] For clarity only two neighbors are shown here, but the same principle holds for a three dimensional field. Moreover u is considered a scalar. For an extension to a Cartesian velocity vector the method can directly be repeated for all three components independently.

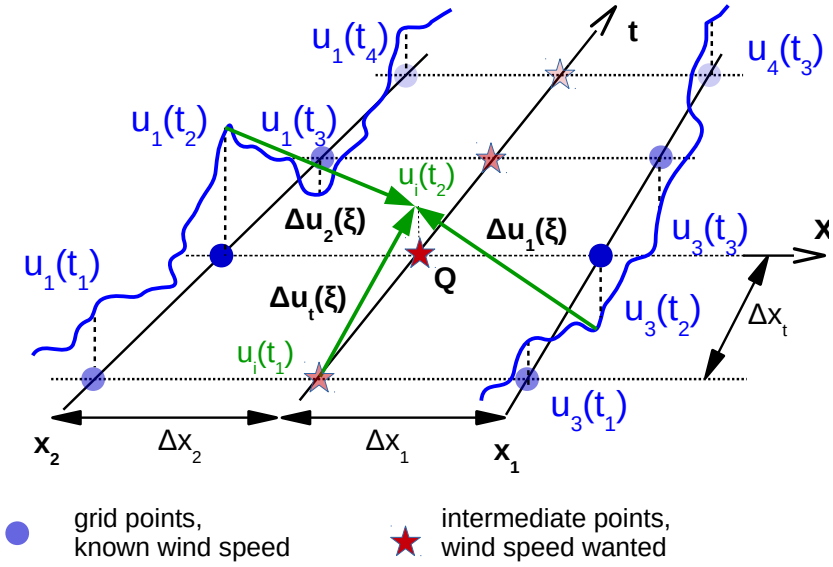

Figure 3.3: The increment interpolation for a two dimensional field correlated in time and space.

was taken for the standard deviation σ of the increment interpolated process. As can be seen from Fig. 3.4 leaving $a \approx 1$ would yield the lowest error. However, to also reproduce the spectrum, the correlation functions have to be matched, and a has to be adapted further. Best agreement of spectrum and variance was found with $a = 2$ for time steps $\Delta t = 0.1$ s and $\Delta t = 0.05$ s, and $a = 4$ for $\Delta t = 0.2$ s respectively. Although the existence of an analytic relation between the cross- and auto-correlation functions and the weighting factor a seems to be reasonable, at this point empiric fitting was found to be sufficient.

Here, the increments $\Delta u_k(\xi)$ and $\Delta u_t(\xi)$ were again generated as random variables via the inverse transform method from the conditional CDFs $F(\Delta u_k|r)$ and $F(\Delta u_t|t)$. Note that in general r can be a multidimensional vector $\vec{r}$ and $F(\Delta u_{\vec{r}}|\vec{r})$ its joint multidimensional conditional CDF. For wind in particular $\vec{r}$ is usually a distance vector and the CDF dependent on its direction as well as its magnitude. However, for clarity and to focus on the method as such, homogeneous turbulence was assumed. Hence r_k simplifies for the present study to a scalar distance between the point of interest Q on the blade and the nearest grid points R_k. Again, if the joint wind speed increment CDF $F(\Delta u_r, r)$ is not known from the statistics of the considered wind, it can be estimated from a short wind sample of sufficiently high resolution via the

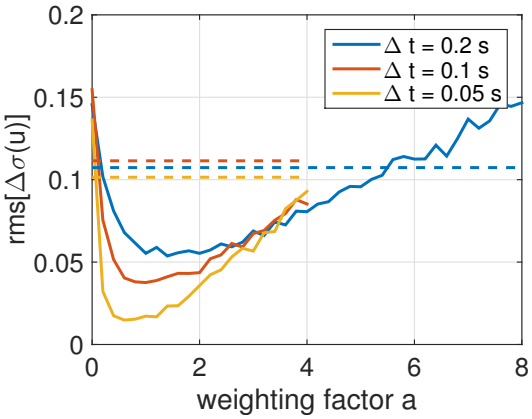

Figure 3.4: RMS relative error of standard deviation between original and interpolated process. Solid line: increment interpolation; dashed line: linear interpolation.

discrete cumulative mass function (CMF) (Simonoff, 1996).

Note that although only the nearest neighbors are used for the interpolation this procedure must not be misunderstood as a simple nearest neighbor interpolation. Instead, it should be recognized that the generated joint CDF contains the statistics of the original process and together with the inverse distance averaging it conserves the correlations. Thus the increment interpolation is based on the fundamental properties of the *whole* process.

3.3 Results

In the previous section the stochastic increment interpolation method was introduced and subsequently used to interpolate turbulent atmospheric wind. In this section we will compare the results obtained from the new method to the results form the current standard procedure, linear interpolation.

3.3.1 Wind speed data set and increment probability distributions

To study the performance of the proposed method and compare it to the existing procedure a high resolution data set is required. With that set an interpolation can be performed between two distant points, and the interpolated results can be compared to the original intermediate points. Although the presented method can be applied to various other fields, for the time being we focus on wind turbine engineering, where wind speed interpolation is a very common task. The international standard

IEC 61400-1, Ed. 3 (2005) governs turbine certification and prescribes wind inflow conditions. Since in engineering practice many designs have to be evaluated quickly in many different conditions, the standard uses a spectral wind model for turbine load calculations. This model generates a sample wind field via an inverse Fourier transform (with randomly generated component phases) from a generic wind speed spectrum together with a coherence function (both prescribed by the standard). Thus a simplified, yet very general sample wind field is provided, which is equally valid at different turbine locations.

'Real' atmospheric wind is very complex and it has been shown repeatedly that a spectral model as used by IEC 61400 does not capture the true physics completely (Emeis, 2012; Park et al., 2015). However, to fully account for the dynamic effects of the atmospheric boundary layer, possibly including buoyancy, requires computationally expensive large eddy simulations (LES) (Vijayakumar et al., 2016) or vast sets of experimental data (Dörenkämper et al., 2014). In applied (wind) engineering, both are not an option as time and computational resources are limited. Moreover, both are very specific to particular locations. Hence they are problematic for use in general turbine design, which should be certified for and sold to wind farms in various different conditions. Due to these limitations the standard uses a simplified, yet very practical spectral wind model.

The stochastic wind simulator *TurbSim* (described by Kelley and Jonkman (2007)) is implemented around this spectral wind model. It is widely used in wind turbine engineering (Graf et al., 2016; Wang et al., 2016) and considered an appropriate engineering model (Lavely et al., 2012; Choe et al., 2015). Hence *TurbSim* was used to generate a high resolution sample wind field to be used as base line for: a) a linear interpolation of wind speeds and b) a stochastic increment interpolation. Thus the two results can be compared directly for the kind of data that is used in wind turbine engineering. The presented method is in principle not limited to this specific wind model. However, at this point we focus on demonstrating its value for the wind model used by the industry. A study and discussion of other models is left for future work.

For this study the increment CDFs $F(\Delta u_k|r_i)$ and $F(\Delta u_t|t_j)$ were extracted from a synthetic field of 91 wind speed points, each 1 m apart, extending over 50 s sampled at 10 Hz for $r_i \in \{1, 2, ...10\}$ m. Based on these 45,500 wind speed values a normal

distribution was fitted to the results via the built-in Matlab function *fitdist()*. Although real wind is known to be not a Gaussian process (Boettcher et al., 2007; Calif and Schmitt, 2012), for the used synthetic wind speed data set the normal distribution was found to be a very good fit. If a more complex wind model is used, or experimental data is available, a different distribution might be a better choice. In that case the presented method is not limited to normally distributed increments. Instead, if the available data suggests a different distribution, any other CDF can be used and the same procedure will be equally viable. If, on the other hand, the considered process is not stationary, the presented method will fail, since increment CDFs valid for the whole process do not exist. In that case the process has to be broken down into several consecutive quasi stationary segments. However, in practical wind engineering this case has already been taken care of by the standard (IEC 61400-1, Ed. 3, 2005), as it requires the use of several short (ten minute) samples, which are each considered stochastically stationary.

3.3.2 Wind speed increments vs. linear interpolation

For wind modeling, a loss in wind speed variance, as incurred through linear interpolation (cf. section 3.1, Fig. 3.1), directly translates to a loss of turbulence intensity $TI = \sigma/\overline{u}$ ($\overline{u}$ denoting the mean wind speed). For illustration a turbulent wind data series was studied. Wind speed data was synthesized at $f = 10$ Hz through *TurbSim* for 91 horizontal high resolution points, each 1 m apart. Only the velocity component u in the main flow direction was considered. From the high resolution data set wind speeds u_L and u_R at two points $d = 10$ m apart were interpolated onto the middle point ($r = 5$ m) via either linear interpolation or stochastic increment interpolation.

Fig. 3.5 compares the results. In the left plot 100 s from linear interpolation is compared to the original data. The right plot compares the original data to one 100 s realization of an increment interpolation. Because the increment interpolation is based on a stochastic increment, which is generated from a random number, each realization of the interpolation is different. Hence, the interpolation will in general not reproduce the original time series exactly. However, the time series resulting from increment interpolation closely resembles the original process, while linear interpolation results in a significant smoothing of the signal. One should also note that although the process is not exactly reproduced, longer trends (on the time scales of roughly ten seconds)

are retained. Hence the general coherence of the wind field is preserved.

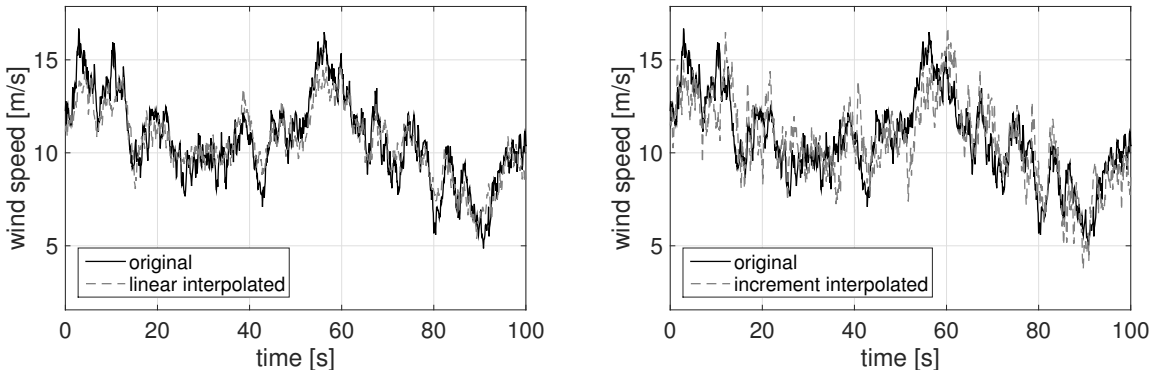

Figure 3.5: Wind speed time series original process vs. interpolation; $d = 10$ m, $r = 5$ m.

Table 3.1 shows the statistics for the resulting time series. The first column shows the statistics of the original wind speed data from the high resolution set at the middle point. The second column gives the statistics for u_M, resulting from linearly interpolation between the outer points onto the middle according to

$$u_M = \left((d - r)\, u_L + r\, u_R \right) / d \tag{3.5}$$

To minimize stochastic errors the presented data is averaged from the nine point pairs spread over the 90 m wind field. The loss of variance and thus turbulence intensity from linear interpolation is obvious.

The data in the third column is generated from increment interpolation via Eq. 3.4 with $K = 2$ for a single left and a single right neighbor, $\Delta x_k = r = 5$ m, and $\Delta t = 1/f = 0.1$ s. The weighting factor was set to $a = 2$. To obtain stable stochastic results an ensemble average over ten independent wind speed realizations was analyzed. As can be seen, using increment interpolation preserves the variance of the original data in the interpolated results.

Fig. 3.6 shows the change in resulting turbulence intensity with changing grid spacing. Now u_L and u_R are taken from two points with increasing separation d. The

Table 3.1: Statistics of wind data series.

($d = 10$ m, $r = 5$ m)	original process	linearly interpolated	increment interpolated
sample frequency [Hz]	10	10	10
sample length [s]	1009	1009	1009
mean [m/s]	10.00	10.00	10.00
variance [m^2/s^2]	3.99	3.17	4.26
turbulence intensity [%]	20.0	17.8	20.6

blue dots show the turbulence intensity resulting from a linear interpolation onto a point in the middle, $r = 0.5d$. The original turbulence intensity is marked for reference. While the turbulence intensity is better conserved when linearly interpolating between very close grid points (i.e. between well correlated wind speeds), the loss increases when linearly interpolating between wind speeds at increasing distances, i.e. with decreasing correlation. Increment interpolation, on the other hand, conserves the variance much better for a wide range of grid spacings d. Only for $d > 12$ m deviations become slowly noticeable even with the increment method.

Fig. 3.7 compares the probability distribution histograms of wind speeds from the original *TurbSim* data set to the wind speeds obtained through interpolation. As for Table 3.1 nine points at $d = 10$ m, $r = 5$ m were considered. Again, for linear interpolation the loss in variance is obvious through a narrower probability distribution. Moreover, it can be seen that this directly corresponds to a reduction in the likelihood of extreme events. Considering ultimate load analysis this leads to an overestimation of return periods, which could have drastic consequences for the structural design process and hence the structure's lifetime. Turning to the increment interpolation we see that now the PDF is conserved much better all the way into the tails of the distribution. Especially for extreme load extrapolation this is a significant improvement, as now return periods of extreme events can be estimated more accurately.

Finally Fig. 3.8 shows a comparison of the power spectral density (PSD) $S(f)$ at the half way point in the middle of the wind field, again for $d = 10$ m, $r = 5$ m. The results from the original wind speed sample at this point are compared to the interpolated data as obtained before. To filter noise the average PSD for eight subsets of the data, each 1024 s long, is shown. Not surprisingly, the loss in turbulence

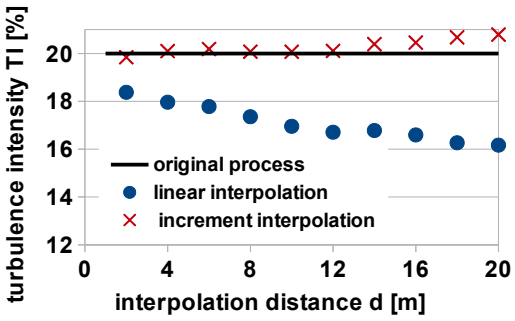

Figure 3.6: Turbulence intensity: original process vs. interpolation for increasing grid spacing.

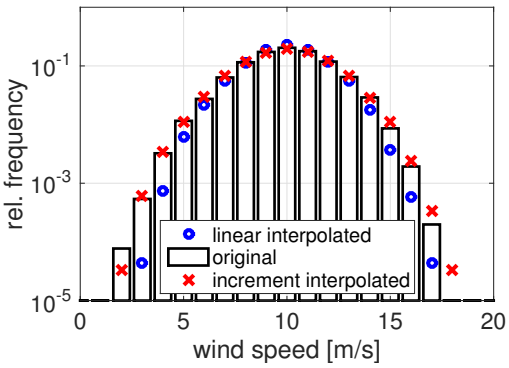

Figure 3.7: Wind speed PDF: original process vs. interpolation. Average from nine points; $d = 10$ m, $r = 5$ m.

intensity found before for the linearly interpolated data is reflected here in reduced power across the sampled spectrum (Fig. 3.8, left plot). The total variance as obtained from an integral over the PSD drops from $\mathrm{Var}_{\mathrm{orig}} = 3.33\ \mathrm{m}^2/\mathrm{s}^2$ for the original wind speed at the middle point to $\mathrm{Var}_{\mathrm{lin}} = 2.36\ \mathrm{m}^2/\mathrm{s}^2$ for the linearly interpolated data onto the same point. Since the spectrum determines loading cycles this divergence will have implications on the fatigue life analysis (Burton et al., 2011).

The right plot in Fig. 3.8 shows the wind speed PSD at the central point for original and increment interpolated data. It can be seen that in contrast to the linear interpolation the original spectrum is now better reproduced. The variance contained in the spectrum amounts to $\mathrm{Var}_{\mathrm{incr}} = 3.37\ \mathrm{m}^2/\mathrm{s}^2$, close to $\mathrm{Var}_{\mathrm{orig}} = 3.33\ \mathrm{m}^2/\mathrm{s}^2$ for the original PSD.

To study the impact of using wind speed increments further, another block of frozen wind with mean wind speed $\bar{u} = 10$ m/s and turbulence intensity $TI = 20\%$ was generated with *TurbSim*. This block covered a 90×90 m^2 domain resolved on 15×15 grid points corresponding to a transverse grid spacing of $d = \Delta y = \Delta z = 6.43$ m, a usual distance for wind turbine analysis[8]. In the streamwise direction the block extended over $x = 8$ km resolved at $\Delta t = 0.1$ s. With Taylor's hypothesis and the set mean wind speed this translates to a streamwise grid spacing of $\Delta x = 1$ m. No wind shear was included for the sake of simplicity of this presentation and only the velocity

[8]The *Bladed* Theory Manual suggests a grid point spacing of 6 – 7 m (Bladed, 2012).

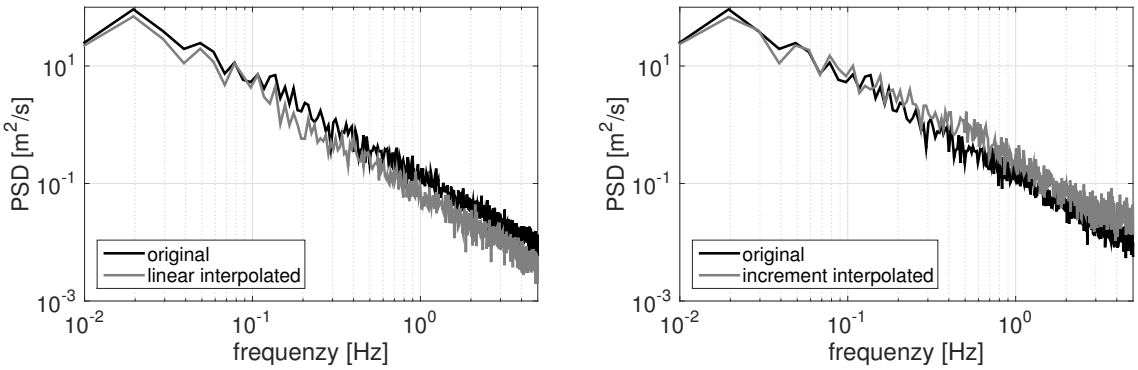

Figure 3.8: Power density spectrum from interpolated wind speeds vs. original wind speeds; $d = 10$ m, $r = 5$ m.

component u in the main flow direction was considered.

Fig. 3.9 shows the apparent wind power density spectrum sampled at 10 Hz on a reference point at $R = 35$ m radius on a turbine blade rotating at $\Omega = 15$ rpm through the wind field. Naturally, the reference point Q on the rotating blade rarely coincided with a grid point of known wind speed. To get instantaneous wind speeds at Q the discrete on-grid wind speed values were once bilinearly interpolated from the four nearest grid points and once computed using the increment interpolation with the instantaneous distances Δx_k, with $k \in \{1, 2, 3, 4\}$, to the four nearest grid points and the 'distance' $\Delta x_t = \Delta t \bar{u} = 1$ m to the wind speed at the current position Q and the previous time step. The wind speed increment PDFs $f(\Delta u_k|r)$ and $f(\Delta u_t|t)$ were initially created for $r \in \{1, 2, ..., 10\}$ m and $t = 0.1$ s on a 90×3 m^2 grid over 100 s resolved at $d = 1$ m and $\Delta t = 0.1$ s.

In average (over ten realizations of the random increment series) the linear interpolation resulted in a rotationally sampled wind speed signal with 12 % less variance. Fig. 3.9 compares the rotationally sampled spectra. As discussed by Burton et al. (2011) the usual peaks at multiples of the turbine rotation frequency are found. As can be seen from the figure the apparent wind power spectra are considerably different at higher frequencies ($f > 1$ Hz). The damping of high frequencies found when using linear interpolation obviously corresponds to the variance loss discussed in the previous sections. The spectrum obtained from increment interpolation on the other hand conserves the statistical properties and most likely reflects the true wind speeds more

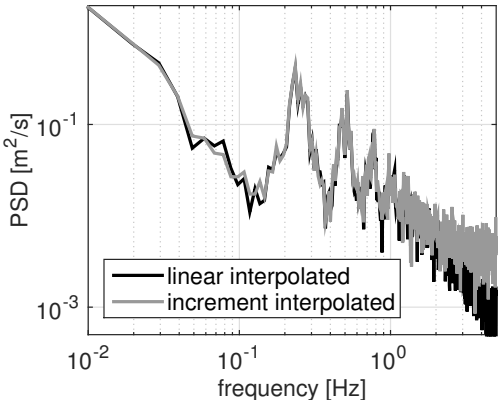

Figure 3.9: Apparent wind speed power density spectrum for a wind turbine blade rotating at 15 rpm.

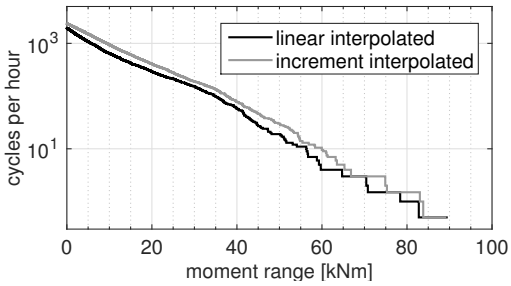

Figure 3.10: Cumulative rainflow cycle count for root bending moment.

closely. These differences are significant for wind turbine design because the affected frequencies ($f \in [1, 10]$ Hz) are well within the range of relevant structural response frequencies: Burton et al. (2011) present spectra of different hub and blade load responses of a turbine operating in turbulent wind. Their plots reach up to 5 Hz and it can clearly be seen that loads do not vanish at these frequency. Milan et al. (2013) show that wind turbine power output is sensitive to wind speed fluctuations down to time scales of a few seconds. Hence, when using an overly damped apparent wind spectrum (as resulting from linear wind speed interpolation) for turbine simulations the loss in higher frequency content may introduce significant error into the resulting load and power output predictions.

For a rough idea about the implication of the different interpolation methods on turbine analysis a minimal turbine example was studied. Since it is the aim of this contribution to introduce an alternative interpolation method a more detailed aerodynamic/ structural analysis is postponed to future work. Here we simply assumed a 2d airfoil section (NACA64-618, 5° geometric angle of attack) rotating at the control point Q as above. From this the time series were calculated for:

- ◇ the section's instantaneous angle of attack α,
- ◇ the force coefficient $c_f(t) = \frac{2F/dr}{\rho u_\infty^2 c}$ (based on F/dr, the resultant force from lift and drag per unit span, c the section's chord length, and u_∞ the free stream wind speed),
- ◇ the power coefficient $c_p(t) = \frac{2F/dr}{\rho u_\infty^3 c} f$ (with $f = \Omega/60$),

◇ and the root bending moment $m(t) = Fr$.

While the resulting peak loads ($\max[c_f(t)]$ and $\max[m(t)]$) from ten different ten minute wind field realizations hardly changed, the lower variance of the linearly interpolated wind speeds yielded less extreme angles of attack. A difference of $\Delta\alpha = -3.6$ % for the most extreme angle of attack was found. Due to the non-linear lift and drag curves this resulted in $\Delta c_p = -4.7$ % less peak power. Fig. 3.10 gives the cumulative rainflow cycle count for the root bending moment induced by this one section. The analysis is obtained from NREL's Crunch tool (Buhl, 2008) from one ten minute realization. Although the peak root bending moment hardly changed with different interpolation methods, Fig. 3.10 shows that linear interpolation consistently yields lower load cycle counts for any moment range. Again, this underestimation through the linear interpolation is critical, as it might lead to premature failure of the structure.

3.4 Conclusions

Data values of weakly correlated highly unsteady or statistical processes are usually recorded only at discrete steps, while often inter-step values are needed as well. It was shown that the common method of linearly interpolating between discrete values distorts the statistical properties of these kinds of data series. Hence this approach was deemed critical since a considerable error may be introduced into the interpolated data set. As an alternative, increment interpolation was introduced. Here a random data increment is generated from an increment probability as a function of the interpolation distance. While the presented increment interpolation procedure is computationally hardly any more expensive than linear interpolation, it conserves the statistical properties of the original process much better.

Both methods, linear and increment interpolation, were evaluated based on the example of the turbulent wind sampled by a rotating wind turbine blade. Here conserving turbulence intensity and the wind spectrum is vital for correct wind loading calculations. Turbine fatigue loading for example is a direct result of unsteady (turbulent) wind excitation and is key to rotor structural design. However, fatigue loading can only be calculated correctly if the correct wind spectrum is conserved. It was shown that the conventional method of linearly interpolating the a priori generated wind speeds results in a considerable smoothing of the original wind speed time series, which causes a loss in turbulence intensity and a damping of the higher

frequency content in the wind power density spectrum. Compared to using wind speed increments, linear interpolation resulted in 27% less power in the apparent wind spectrum for frequencies $f \in [0.01, 5]$ Hz with most losses occurring for $f > 1$ Hz.

Increment interpolation, on the other hand, demonstrated very good conservation of statistical properties. The variance, and thus the turbulence intensity, and the probability distribution, as well as the spectrum of the data were maintained. Hence using data increments is suggested as a better approach for interpolating highly unsteady processes such as turbulent atmospheric wind.

In a next step the method is to be extended to be applicable to a 3D wind vector field, including wind shear. This transition merely turns the wind speed increment and the distance into vector valued variables, while the method itself remains the same. This work and a more detailed quantification of the error introduced by the different interpolation methods will be studied within the context of an aero-elastic wind turbine simulation in future work.

Chapter 4

An Engineering Model for 3D Turbulent Wind Inflow Based on a Limited Set of Random Variables

This chapter presents the latest version of a paper accepted for public discussion in Wind Energy Science Discussions:
Fluck, Manuel and Crawford, Curran: "*An engineering model for 3D turbulent wind inflow based on a limited set of random variables*", Wind Energy Science Discussions, **2017**, in review; DOI: 10.5194/wes-2017-7

In this paper we address the 'curse of dimensionality' encountered later on. When employing stochastic models for wind turbine aerodynamic calculations we will find that the number of random variables that our stochastic model can handle is limited. Hence, we seek a wind inflow model that relies only on a limited set of random variables. Since no adequate model was available previously, we derive and validate a reduced order wind model in this section.

See Appendix C.3 for further information regarding the MATLAB code used to generate results for this section.

Abstract

Emerging stochastic analysis methods are of potentially great benefit for wind turbine power output and loads analysis. Instead of requiring multiple (e.g. ten-minute) deterministic simulations, a stochastic approach can enable quick assessment of a turbine's long term performance (e.g. 20 year fatigue and extreme loads) from a single stochastic simulation. However, even though the wind inflow is often described as a stochastic process, the common spectral formulation requires a large number of random variables to be considered. This is a major issue for stochastic methods, which suffer from the 'curse of dimensionality' leading to a steep performance drop with an increasing number of random variables contained in the governing equations. In this paper a novel engineering wind model is developed which reduces the number of random variables by 4–5 orders of magnitude compared to typical models while retaining proper spatial correlation of wind speed sample points across a wind turbine rotor. The new model can then be used as input to direct stochastic simulations models under development. A comparison of the new method to results from the commercial code *TurbSim* and a custom implementation of the standard spectral model shows that for a 3D wind field the most important properties (cross-correlation, covariance, auto- and cross-spectrum) are conserved adequately by the proposed method.

Nomenclature

Latin Letters:

e	Euler's number
$\vec{f} = [f_m]$	frequency
$i = \sqrt{-1}$	imaginary unit
N_F	number of frequencies
N_P	number of wind speed points
N_R	number of random variables
P	a point in Euclidean space
S_{kk}	(auto) power spectrum
S_{kj}	cross power spectrum
t	time
U	wind speed Fourier coefficient
u	wind speed

Greek Letters:

θ	phase angle
$\Delta\theta$	phase angle increment
ξ	random number
$\vec{\omega} = [\omega_m]$	angular frequency

Indices:

j, k	points in space
m	frequencies

4.1 Introduction

Engineering design tasks frequently face uncertain or random model parameters (e.g. imprecise component geometries), system properties (e.g. tolerances on manufacturing quality), and/ or boundary conditions (e.g. varying wind conditions). In a deterministic modeling framework the analysis of such uncertain systems produces one specific solution for each realization of the random quantity. A 'realization' (also referred to as one 'sample') is one specific observation of the random quantity, for example a specific solution for one specific geometry, or one specific set of inflow conditions. In a numerical experiment a realization is usually obtained based on the generation of one specific random seed. However, through this process the stochastic dimension of the problem at hand is either ignored entirely, by analyzing the most likely case only (the purely deterministic approach), or it requires multiple parallel solutions to assess the statistics of the results a posteriori, for example via extreme value, sensitivity analysis, or Monte Carlo simulation. Often the first two options are insufficient, and the latter is computationally too expensive. To solve this dilemma the focus of recent research has lately moved towards stochastic analyses and uncertainty quantification (Sudret, 2007; Najm, 2009; Le Maître and Knio, 2010; Sullivan, 2015). Rather than generating one specific solution for each realization of a random input or model quantity, a stochastic analysis can help assess uncertainties quicker and even

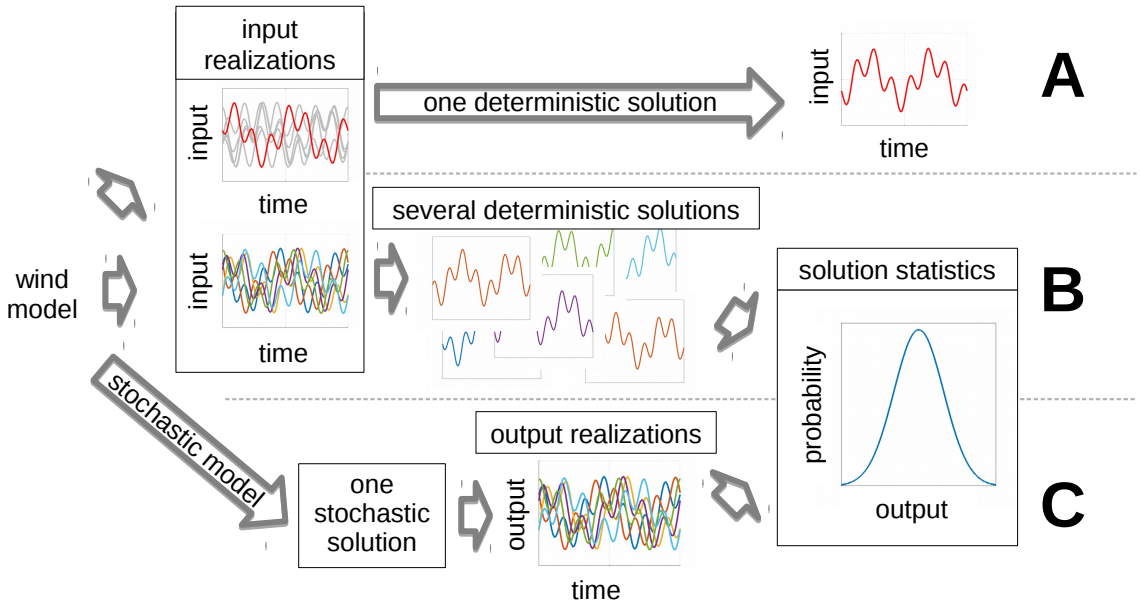

Figure 4.1: Comparison of the solution processes in a pure deterministic (A), a deterministic-statistic (B), and a stochastic framework (C).

include uncertain quantities directly into the system analysis. This is because it not only provides one specific solution, but it solves the problem for the whole ensemble of all possible realizations at once, see Fig. 4.1. This is made possible via stochastic methods that transform the problem from multiple deterministic realizations with random seeds to a formulation of the govening equations that directly describe the stochastic variables in the system. The stochastic solution then directly describes the statistics (e.g. the probability distributions) of the outputs, based on the properties given for the input variables in the forcing terms of the governing system equations.

In wind turbine engineering, the driving force, the turbulent atmospheric wind, is commonly described as a stochastic field, derived from turbulent wind models developed around stochastic ten-minute mean wind speed distributions. This naturally invites the use of stochastic methods to assess extreme and fatigue loads, annual power production, power fluctuations, etc. in a stochastic sense and thus exploit the advantages of stochastic methods. However, wind turbine design and analysis is usually carried out in a deterministic fashion, or at best as a Monte-Carlo-like set of several subsequent deterministic solutions (path A and B in Fig. 4.1 respectively). The wind turbine design standard IEC 61400-1, Ed. 3 (2005) is indicative of this

deterministic framework. It bases the turbine load analysis on multiple deterministic simulations, carried out at many different mean wind speeds, for about 20 different load cases, each simulated for ten minutes and repeated several times with different realizations of the turbulent inflow, each generated from a different numerical random seed. For a land based turbine this quickly amounts to evaluating several hundred ten-minute samples. For offshore turbines, where various wind conditions (wind speed and direction) additionally have to be combined with various sea states (combinations of wave height and direction) this number increases to several thousand ten-minute evaluations. However, even with a large number of deterministic simulations, extrapolation to extreme loads is a delicate exercise and results can vary greatly (Moriarty, 2008; Burton et al., 2011). Moreover, Zwick and Muskulus (2015) show that basing a wind turbine analysis on six ten-minute wind speed simulations, generated from six different random seeds, results in a difference of up to 34% in the ultimate loads for the most extreme 1% of seed combinations. Tibaldi et al. (2014) present a study, which indicates that turbine loads extracted even from 20 different ten-minute wind fields, generated from 20 different random seeds, vary greatly. This shows that in a deterministic framework load variations from different random seeds can dominate effects from design parameter changes even with a fairly large number of realizations analyzed. Obviously this constitutes a severe problem, particularly when concerned with gradient-based optimization where not only relatively fast solutions times, but also reliable design variable gradients are vital.

A direct stochastic treatment of the wind loading (path C in Fig. 4.1), on the other hand, considers the wind as a stochastic process throughout the turbine simulation procedure. It postpones the generation of realizations until after the calculation of a solution for the system equations, which thus become stochastic equations. Hence it can be a means to efficiently include stochastic parameters, directly obtain a stochastic solution, and arrive at the statistics of the resulting loads much quicker. Fluck and Crawford (2017b) present an example of a stochastic analysis for wing loads in turbulent inflow, and show that such a stochastic approach does not rely on the repeated analysis of multiple (e.g. 600 s) realizations of the wind field. Instead one (possibly short, e.g. 10 s) stochastic result yields all possible realizations and hence contains the full spectrum of uncertainties. Thus it will enable the analyst to obtain a more complete description of the resulting load ensemble at large, calculate its statistics, and eventually arrive at more precise estimates of e.g. the probability of exceedance

of some load threshold more quickly.

Recently, progress has been made towards stochastic analysis of wind turbines. For example, results have been shown for an aeroelastic analysis with one uncertain system parameter, stiffness or damping (Desai and Sarkar, 2010), and for the a stochastic formulation of airfoil lift, drag, and pitching moment in stall conditions (Bertagnolio et al., 2010). Moreover, stochastic models have been used for wake modeling, treating wake center and shape as random processes (Doubrawa et al., 2017). However, only very early steps have been completed to include the biggest source of uncertainty: the uncertain inflow from turbulent atmospheric wind. On a wind farm scale Padrón et al. (2016) recently presented a layout optimization based on a polynomial chaos formulation for the freestream wind speed and direction. Finally Guo (2013) offers a stochastic wind model used for a stochastic analysis of wind turbine loads. However, he still bases the stochastic analysis on deterministic sampling (i.e. path B in Fig. 4.1). Moreover this model driven by the decomposition (bi-orthogonal and Karhunen-Loève) of a specific set of wind field data. It hence is not generally applicable, but relies on the availability of sufficient data.

As turbulent wind is already represented as a stochastic field in many common wind models, a transition from a deterministic aerodynamic model for specific wind realizations, to a stochastic model yielding the whole stochastic load ensemble at once, seems an obvious step. However, this step comes with a simple, yet fundamental challenge: current wind models, even simple spectral models, rely on a large number of random variables to set the wind sample's phase angles. Since realizations of large sets of random variables can be generated very quickly, this is not a problem for deterministic load analyses. However, the computational cost of stochastic analysis methods increases dramatically with the number of random variables included, a fact commonly known as the 'curse of dimensionality' (Majda and Branicki, 2012). This renders current wind models inaccessible to stochastic methods, and thus poses a major barrier to the further development of stochastic models for the analysis of wind turbine loads based on a stochastic description of the turbulent wind input.

To address this problem we reformulate an industry standard wind model into a reduced order engineering model. The aim of our work is to develop a wind model that can generate a realistic wind field with appropriate (long term) dynamic properties

from considerably less random variables than the current models. In the last three decades numerous turbulent wind models have been proposed. Kleinhans et al. (2008) summarizes a few. However, none of the previous models had an application in stochastic aerodynamic models in mind. Hence, as generating a large set of random numbers as a seed for a wind field realization is usually no problem, the existing models we are aware of rely on a large number of random variables – too large to be applicable to a direct stochastic modeling of the aerodynamic wind turbine equations (path C in Fig. 4.1).

In the following we focuses on a formulation for the IEC standard spectral wind description (IEC 61400-1, Ed. 3, 2005), so that it may be directly useful in industry. Veers' model (Veers, 1988) was chosen as baseline and starting point. This model is widely used, for example in the stochastic wind simulator *TurbSim* (described by Jonkman and Kilcher (2012)), which synthesizes a sample of turbulent atmospheric wind from Veers' spectral formulation. Although it is well known that Veers' model does not capture all physical details of 'real' atmospheric wind (e.g. Mücke et al. (2011); Morales et al. (2012); Lavely et al. (2012); Park et al. (2015)), it is for many cases an appropriate engineering model (Nielsen et al., 2007). Due to its comparatively high independence of site specific parameters, ease of use, and low resource requirements, Veers' model is the preferred model for many applications (Lavely et al., 2012). Moreover, it is endorsed by the governing wind turbine design standard IEC 61400-1, Ed. 3 (2005), and thus is widely used in the wind energy industry. This underlines that its fidelity is accepted as a reasonable compromise in engineering practice for wind energy. As such, Veers' model provided a well accepted foundation to base further development on. Note that our goal is not improving on known deficiencies of Veers' model, but to arrive at a model that can generate a wind samples of comparable (and accepted) fidelity with significantly less random variables, geared towards eventual inclusion in a stochastic wind turbine simulation.

The following sections will first briefly review Veers' model to set the stage for the proposed modifications. Subsequently, the new reduced order wind model is introduced, and finally results are presented, which confirm that key statistical properties (cross-correlation, covariance, auto- and cross-spectrum) are conserved by the new model. The paper concludes by giving direction for continued work on integrating the wind model into a turbine simulation and on refinements with other

turbulent wind descriptions. To not overload this paper, the focus is solely on the details and validation of the stochastic wind inflow model itself. Interested readers should refer to Fluck and Crawford (2017b) for the basic stochastic aerodynamic model, or Fluck and Crawford (2016c) for an example how the reduced order wind model is used to calculate stochastic loads on a stationary wing.

4.2 Method

In this section we first briefly summarize Veers' method, as it represents the established method for synthesizing turbulent wind (Nielsen et al., 2007; Lavely et al., 2012), and at the same time is the baseline for our contribution. Subsequently, we will introduce our new reduced order method. Note that Section 4.2.1 is only meant as a summary to lay out the basics for the following work. For a complete introduction, the reader is referred to Veers' original paper (Veers, 1988) and successive work, e.g. Kelley (1992); Nielsen et al. (2004); Burton et al. (2011).

4.2.1 Veers' method

In a spectral method, the wind speed time series $u_k(t)$ at each point P_k, $k = 1...N_P$, in the sampled wind field is obtained through the inverse discrete Fourier transform of a set of discrete frequencies components from the double-sided (symmetric) spectrum U_{mk} at $\omega_m = 2\pi\, f_m$, $m = -N_F...N_F$

$$u_k(t) = \sum_m U_{mk} e^{i\omega_m t} \tag{4.1}$$

Here m is used to index the frequency bins, and k is used to index the points in space where wind speed data is recorded. Usually, the terms U_{mk} are binned Fourier amplitudes centered at the frequency ω_m, prescribed by the wind speed spectrum $S(\omega_m)$ at each point P_k. Often a Kaimal spectrum is used (IEC 61400-1, Ed. 3, 2005).

Following Veers' method (Veers, 1988), $U_{mk} \in \mathbb{C}$ contains not only the amplitude but also the random phase angles at point P_k for each frequency ω_m. To obtain the desired coherence for all frequencies and between any two points in the wind field, all phase angles

$$\theta_{mk} = \arctan\left(\frac{\mathrm{Im}(U_{mk})}{\mathrm{Re}(U_{mk})}\right) \tag{4.2}$$

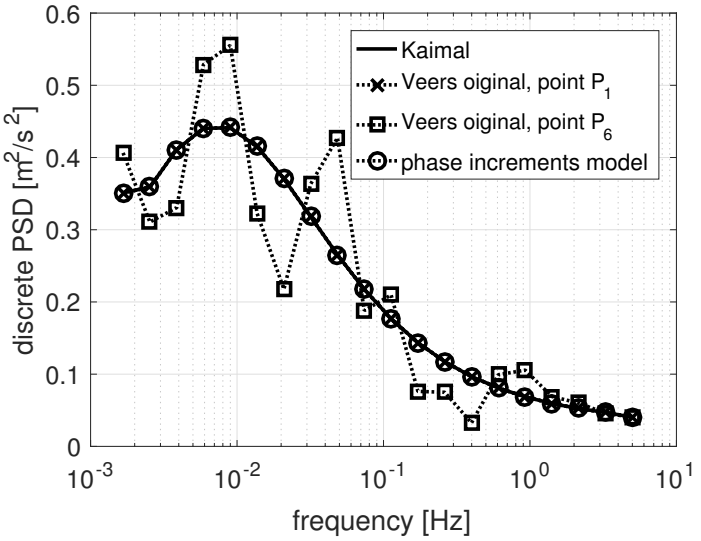

Figure 4.2: Raw wind spectra from a single wind speed sample, no averaging. Kaimal: the analytic spectrum; Veers: sample of the spectrum resulting from Eq. 4.3 at two different points P_1 and P_6; Phase increments: the spectrum from the reduced order phase increment model Eq. 4.8 (identical for all points).

need to be correlated correctly. To achieve this, Veers multiplies the set of $N_R = N_F \cdot N_P$ independent, uniformly distributed random variables $\xi_{jm} \sim U(0,1)$ with the weighting tensor H_{jkm}, obtained from the discrete cross spectrum $S_{jk}(\omega_m)$, to obtain the complex Fourier coefficients U_{mk} at each frequency band ω_m:

$$U_{mk} = \sum_{j=1}^{k} H_{jkm}\, e^{i\,2\pi\xi_{jm}} \tag{4.3}$$

where $S_{jk}(\omega_m)$ is given by the relevant design standard or physics model. Note that through Eq. 4.3 the phase angles at point P_k are related to the phases at all previously computed points $P_{j<k}$. Thus, correctly correlated Fourier coefficients are obtained, which can now be inserted into Eq. 4.1 to obtain a correlated wind field.

This method works well to generate multiple (deterministic) data sets at many points. However, as already noted by Veers in his original publication (Veers, 1988), Eq. 4.3 changes the amplitude of each Fourier coefficient, such that $|U_{mk}| \neq \sqrt{S_{kk}(\omega_m)}$ for all but the point computed first. Thus, the prescribed (e.g. Kaimal) spectrum $S_{kk}(\omega_m)$ is not conserved anymore at each point for any single realization, see

Fig. 4.2. However, if spectra are averaged over either several points or several realizations, the wind field's average spectrum converges to the prescribed spectrum as $\lim_{N\to\infty} 1/N \sum_{k=1}^{N} |U_{mk}(\omega_m)| = \sqrt{S_{kk}(\omega_m)}$, with N the number of samples or realizations. This means the field still is stochastically homogeneous, as expected. However, for a stochastic analysis where only a limited number of samples might be used, this may pose a challenge. In the following we introduce a reduced order model based on phase angle increments. This model not only yields a significant reduction in random variables required to synthesize a stochastic wind field, but it also analytically preserves the prescribed spectrum at any single point for each realization (see Fig. 4.2 'phase increments').

4.2.2 The reduced order model with phase increments

To arrive at a reduced order model we follow a two step process. First is a reduction in the number of frequencies necessary for the spectral composition of the wind speed time series at a single point in space, and with it a reduction in the number of random phase angles associated with each frequency. This frequency reduction has been done before. For example Fluck and Crawford (2017b) showed that with ten frequencies from the IEC Kaimal spectrum, logarithmically spaced in $[0.003, 5]$ Hz (a $T = 333$ s sample, resolved at 10 Hz, a reasonable time step for wind turbine simulations, cf. Bergami and Gaunaa (2014)), a realistic wind speed time series can be produced, with probability distribution (and thus turbulence intensity), as well as the wind speed auto-correlation similar to results from a full *TurbSim* simulation at 10 Hz for 10,000 s (roughly $5 \cdot 10^4$ frequency bins). Ten frequencies, and thus ten random variables for the phase angles is manageable as input to a stochastic model. However, when dealing with a wind field big enough to be used for wind turbine calculations, many points (typically a grid in the order of 15×15 points over the rotor disk) of correlated wind speed are necessary. The challenge is to extend this limited frequency wind description from a single point to a spatially varying wind field without excessively increasing the number of random variables required. Fung et al. (1992) introduced a wind model which models both the spatial and the temporal dimension through Fourier modes. They reduced the number of modes down to as little as 38, however, the model then relied on several random numbers associated with each mode. Fung et al. (1992) did not report in detail how many random variables they used for their model, but the

equations indicated that this number was still considerably larger than manageable by stochastic methods. The following paragraphs will introduce a new approach, which will allow to create a stochastic wind field from a significantly reduced number of random variables, independently of the (spatial) size of the wind field, i.e. independently of both, the number of data points over the rotor disc as well as the lateral extent.

In Veers' model the phase angle matrix $\mathbf{\Theta} = [\theta_{mk}]$ is populated with random numbers. We note that random phase angles in the rows and columns of $\mathbf{\Theta}$ carry out two distinctly different functions. At each individual point P_i the different phase angles in the column vector $[\theta_m]_i = \vec{\Theta}_i$ generate constructive/ destructive interference of the ensemble of base sinusoids. Thus, different realizations of $\vec{\Theta}_i$ generate the "gusty" nature of the wind speed time series at that point. This is indeed the *temporal* variability of the wind.[9] On the other hand, the wind speed structure in space, for example the fact that strong winds at one point correlate with strong winds at a nearby point, is captured through the relation of phase angles for the one particular frequency ω_l at different points P_i and P_j – that is in each row of $\mathbf{\Theta}$, $[\theta_k]_l = \bar{\vec{\Theta}}_l$. This is the *spatial* variability of the wind.

While the phase angles at each point (the columns $\vec{\Theta}_i$) are uncorrelated, the phase angles between two points (the rows $\bar{\vec{\Theta}}_l$) have to be correlated to reproduce the spatial structure correctly. For two column vectors $[\theta_m]_i$ and $[\theta_m]_j$ this means while the entries within each vector are uncorrelated the two vectors themselves are element-wise correlated, Fig. 4.3. For wind, this correlation decreases with both, increasing frequency and increasing distance.

For our use-case of turbulent wind as input to dynamic wind turbine analysis, we observe the following:

1. The temporal variability is of primary importance, since it drives the dynamic excitation of the system under investigation. This is the duration of gusts and lulls, captured by the energy distribution in the frequency spectrum of the wind sample.

[9] Note that one dimension of the block of wind, in the average wind direction, corresponds to a temporal correlation as the wind moves downwind.

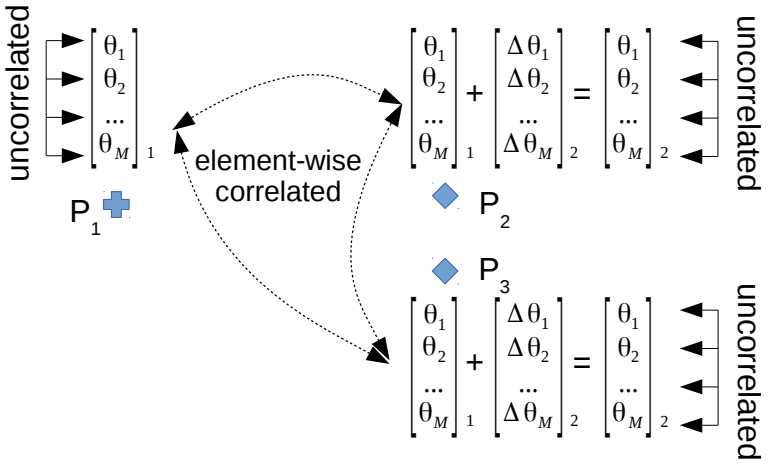

Figure 4.3: Schematic of random phase angle vectors and deterministic phase increments.

2. The spatial variability needs to be represented correctly to yield representative wind loads, since the length scale of spatial wind structures needs to be correct to result in the correct integral loads. For example, for any instance when a sensor A on the blade experiences an increased load, another sensor B a certain distance away from A needs to experience a load correctly correlated to the load at A.

3. For each point, all elements in each column vector $\vec{\Theta}_i$ are independent (Fig. 4.3). However, the column vectors $\vec{\Theta}_i$ and $\vec{\Theta}_j$ at two points P_i and P_j are element-wise correlated. This means the phases in each row vector $\bar{\Theta}_l$ are *not* independent. Following Veers' method, only the elements in $\bar{\Theta}_1$ are independent, while the phases at all other points are mapped from i.i.d. random variables ξ_{mi} such that they are correlated to the phases at the base point P_1 (and thus to each other), Eq. 4.3.

To obtain a reduced order model which requires fewer random variables we propose splitting the complex Fourier coefficients U_{mk}, into a temporal and a spatial part. The temporal part will contain the amplitude of each Fourier mode as well as the random phase angles. It therefore will determine the structure of the wind speed sample in time. The spatial part will contain the phase correlation between different points across the wind field. It will thus set the wind field structure in space. To reflect this

approach we can write:

$$U_{mk} = \underbrace{U_{m1}}_{\text{temporal}} \cdot \underbrace{e^{i\Delta\theta_{mk}}}_{\text{spatial}} \tag{4.4}$$

The temporal part contains the amplitude according to the prescribed power spectrum $S(\omega_m)$ and a vector of random phase angles $\theta_{m1} = 2\pi\xi_m$ at an arbitrary base point P_1 within the wind field:

$$U_{m1} = \sqrt{S(\omega_m)}\, e^{i\theta_{m1}} \tag{4.5}$$

with independent and identically distributed $\xi_m \sim U(0,1)$ as before. Similar to the wind speed increments used for wind interpolation by Fluck and Crawford (2016b), the spatial part is based on the idea of phase increments $\Delta\theta_{mk}$, which are specific to each point and each frequency relative to the base point P_1:

$$\Delta\theta_{mk} = \theta_{mk} - \theta_{m1} \tag{4.6}$$

The increment $\Delta\theta_{mk}$ holds the correlated phase information to generate the correct spatial structures. Since θ_{mk} and θ_{m1} are random numbers, the increments $\Delta\theta_{mk}$ are random, too. In contrast to Veers' approach of employing the cross spectrum to map a set of uncorrelated random variables to a set of correlated phases for each point in the wind field, we neglect the random nature of $\Delta\theta_{mk}$ and consider the phase increments deterministic constants to move between points as illustrated in Fig. 4.3. Note that $\Delta\theta_{mk}$ only contains the spatial structure, but not the temporal part. That means 'gusty' features of the wind (lulls and gusts at different points) are still generated from random numbers; only the wind field's structure in space is fixed with each specific set of phase increments. Based on the three observations above (1-3) this seems justified for two reasons. Firstly, the phases in each row vector $\bar{\Theta}_l$ are correlated, while the phases in each column vector $\vec{\Theta}_i$ are uncorrelated (3). This means there is more 'randomness' in the temporal dimension then in the spatial dimension. Secondly, for the dynamic analysis of a wind energy device, the temporal part is of primary importance. While the spatial structures have to be represented correctly, their variability can be considered secondary (1,2).

It is important to note that focusing on the temporal part does not mean that each realization of the reduced order wind field will exhibit the same spatial structure of gusts and lulls, i.e. that a gust at point P_i would e.g. necessarily come with a lull

at another point P_j. IN contrary, the proposed method does not alter the original correlation between wind speeds at two distinct points which is generally smaller than unity. Graphically speaking gusts and lulls result from the interference of different frequency component sinusoids and phase offsets. Based on the specific realization θ_{m1} the phase angles at each point $\theta_{mk} = \Delta\theta_{mk} + \theta_{m1}$ will be different each time. Thus, the interference between the frequency components and consequently the structure of the gusts and lulls will be different with each different realization of phases at the base point θ_{m1}. Figure 4.6, which will be discussed later, demonstrates this fact. Nonetheless, the proposed reduction of random variables necessarily causes a certain increase in dependence of wind speeds across the wind field. An investigation into how this dependence actually looks like in detail is left for future work.

Inserting Eqs. 4.5 and 4.6 into Eq. 4.4 yields the Fourier coefficients based on only one vector of random phases $[\theta_{m1}]$ and the (auto-) spectrum:

$$U_{mk} = \sqrt{S(\omega_m)}\, e^{i(\theta_{m1} + \Delta\theta_{mk})} \tag{4.7}$$

Substituting $\theta_{m1} = 2\pi\xi_m$ with $\xi_m \sim U(0,1)$ as before, Eq. 4.1 can be turned into our reduced order model:

$$u_k(t) = \sum_m \sqrt{S(\omega_m)}\, e^{i(\omega_m t + 2\pi\xi_m + \Delta\theta_{mk})} \tag{4.8}$$

Note that while Eq. 4.3 changes the amplitude of each Fourier coefficient and thus distorts the spectrum at each point, Eq. 4.8 fully conserves the spectrum.

In contrast to Veers' original model, where $N_R = N_F \cdot N_P$, in the reformulated model $N_R = N_F$. This means the number of random variables N_R only depends on the number of frequencies N_F used for the wind Fourier series, not on the number of wind speed measurement points N_P in the 3D wind field. With the available strategies to reduce the number of frequencies required in a spectral wind model Eq. 4.8 now allows expression of a turbulent wind field consistent with Veers' model, but with significantly fewer frequencies.

What remains is to obtain the phase angle increments $\Delta\theta_{mk}$. Since these determine the cross-correlation between any two points in the wind field, and since

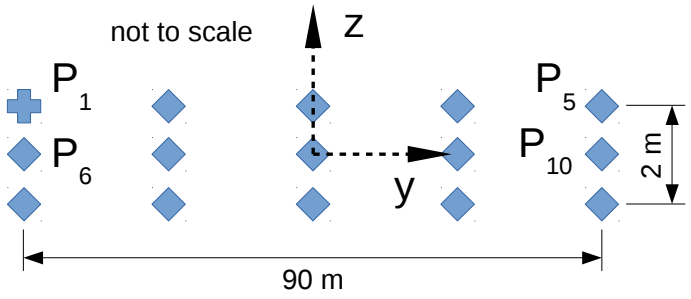

Figure 4.4: Schematic of grid points of wind speed data (minimal test case). We arbitrarily chose the right hand top point (P_1) to be the base point.

the cross-correlation and the cross-spectrum are linked as a Fourier transform pair (correlation theorem, see e.g. (Kauppinen and Partanen, 2011)), it should be possible to analytically generate one set (one realization) of phase increments directly from the cross-spectrum. For now, however, we extract one phase angle increment set from one realization of Veers' Eq. 4.3, with an analytic solution left to future work.

4.3 Results and discussion

In the following we will take a closer look at statistical metrics of the synthetic reduced order wind field. As mentioned earlier our goal is not to develop a more physically faithful wind model, but rather to reduce the number of random variables required while retaining similar fidelity as the methods currently in use. *TurbSim* (Jonkman and Kilcher, 2012) is widely used in industry and the de facto standard to generate synthetic wind fields for wind turbine analysis. Hence we use *TurbSim* wind speed data sets as the benchmark. In the following we compare results obtained from *TurbSim* to two different reduced order models.

The first is our implementation of Veers' model, which allowed us to freely choose the number of frequencies at each data point and the frequency binning. As suggested by Veers equations implementation relies on the conventional inverse discrete Fourier transform with random phase angles at each frequency bin. This model was validated directly against *TurbSim*. If many frequencies are used and identical phase angles are enforced perfect agreement of the resulting data set was found as

expected. As shown by Fluck and Crawford (2017b) the wind speed time series at a single point for a 333 s sample can be well represented with $N_f = 10$ logarithmically spaced frequencies $\vec{f} = \vec{\omega}/(2\pi) = [f_m] \in [f_1, f_{N_F}] = [0.003, 5]$ Hz with $f_m = 10^{a_m}$ and $a_m = \log_{10}\left(\frac{f_{N_F}}{f_1}\right)\frac{m-1}{N_F-1}$ for $m = 1, \ldots, N_F$. For better comparison (equal sample length $T = 600$ s) we use $N_F = 20$ frequencies in $\vec{f} = [f_m] \in [1/600, 5]$ Hz. The results of this model are labeled '**Veers** $_{\mathbf{red}}$' in the following discussion. This model does not include new theory, yet it is a critical step between *TurbSim* (and thus Veers' original model) and our reduced order model. The second model presented is our reduced order model as described above (Eq. 4.8). The newly introduced theory of deterministic phase increments $\Delta\theta$ is employed here, together with a limited number frequencies $N_F = 20$ and thus a reduced number of stochastic variables $N_R = 20$. These results are labeled '**Veers** $_{\mathbf{red,\ \Delta\theta}}$'.

Table 4.1: Comparison of random numbers used in different wind models for a common grid size.

	TurbSim	Veers $_{\text{red}}$	Veers $_{\text{red, }\Delta\theta}$
sample length	10 min	10 min	10 min
grid size $N_{Py} \times N_{Pz}$	15×15	15×15	15×15
frequencies N_F	~3,000	20	20
total number of random variables N_R	$6.75 \cdot 10^5$	4,500	20

Tab. 4.1 gives a comparison of the three models. Note particularly the total number of random variables required by each model, assuming a typical grid resolution in the order of 15×15 points over a rotor disk of $D = 90$ m diameter. While the use of a limited set of frequencies (Veers $_{\text{red}}$) yields a noticeable reduction in random numbers, for a turbulent wind field with several wind speed data points in x- and y-direction, this alone is not enough to arrive at a wind model with few enough random numbers to be applicable in a stochastic method (several dozen random variables to be tractable). Only the additional introduction of deterministic phase increments (Veers $_{\text{red, }\Delta\theta}$) to decouple the number of random variables from the number of wind speed data points reduces the number of random variables drastically enough to obtain a wind model which can be reasonably handled by a stochastic method.

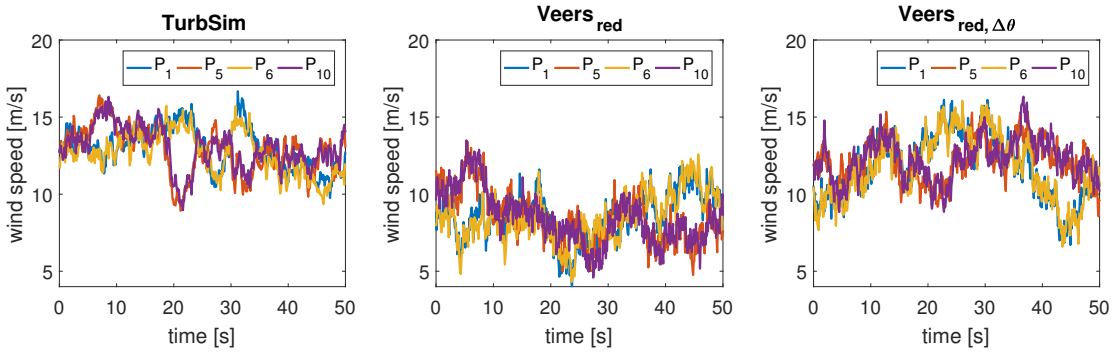

Figure 4.5: Three 50 s excerpt of a wind speed time series sample at four points generated from different models and different random seeds. TurbSim: NREL's original *TurbSim* model; Veers $_{\text{red}}$: Veers model with a limited number of frequencies ($N_F = 20$); Veers $_{\text{red, }\Delta\theta}$: Veers model with a limited number of frequencies and phase increments to model spatial structures at different points, see Tab. 4.1.

As a test case we study a wind field generated on $N_{Py} \times N_{Pz} = 5 \times 3 = 15$ points located on a regular grid as depicted in Fig. 4.4. The origin of the wind field was located 100 m above ground with mean wind speed $\bar{u} = 10$ m/s and no wind shear. The IEC class A normal turbulence model with a Kaimal spectrum (IEC 61400-1, Ed. 3, 2005) and homogeneous turbulence was used. Data was sampled at 10 Hz. We arbitrarily chose the top left hand point (P_1) as the base point. Note that the grid used here contains fewer points than the usual grid for the analysis of a modern $D = 90$ m rotor diameter wind turbine (where $N_{Py} = N_{Pz} = 15$ is more likely). However, the reduced number of grid points enabled us to solve the equations quickly with all models and more clearly illustrate the method. At the same time, the configuration of Fig. 4.4 still allowed us to study both the wind speed time series of points in close proximity (e.g. P_1 and P_6), as well as at more distant points (e.g. P_1 and P_5).

Fig. 4.5 shows realizations of the wind speed time series sampled at four points (P_1, P_5, P_6, and P_{10} in Fig. 4.4) from the three different models. For each model the samples are generated from different random seeds. Thus the time series are not identical. Still, it can be seen that the fundamental structures are conserved through both reduced order models. In particular, even if wind samples are synthesized with only 20 random numbers and deterministic phase increments (Veers $_{\text{red, }\Delta\theta}$) the wind speeds at two points in close proximity (P_1 and P_6, or P_5 and P_{10}) are highly correlated, while at more distant points (e.g. P_1 and P_5) the correlation is weaker. It is important to note that this holds not only for points in relation to the base point, but for all

point pairs. For example, points P_5 and P_{10} are both far away from the base point, but close to each other. As expected, the wind speeds at these two points are well correlated.

Fig. 4.6 shows three realizations of wind speed time series plots at three points obtained from the new phase increment model (Veers $_{\text{red, }\Delta\theta}$), Eq. 4.8. The phase increments are considered deterministic, and $\Delta\theta_{mk}$ is fixed for all realizations. The randomness enters the time series only via random phase angles at the base point P_1 with $\theta_{m1} = 2\pi\xi_m$. As can be seen from the figure, this does *not* result in a complete determination of the spatial relation between wind speeds at different points, since the samples still contain different gusts and lulls at different instances in time.

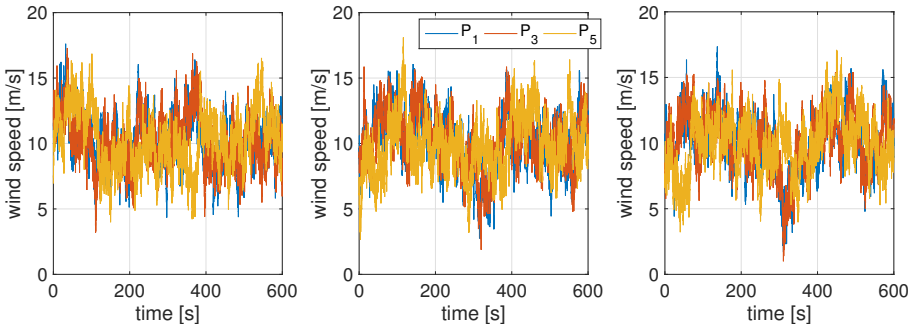

Figure 4.6: Three realizations of wind speed time series at three points generated from the the new reduced order model with fixed phase increments (Veers $_{\text{red, }\Delta\theta}$ model).

Beyond this qualitative visual comparison of the wind speed time series the remainder of this section will show that the phase increment model produces the same statistics as Veers' original model (with only 20 frequencies) as well as the full *TurbSim* model (with the full set of frequencies) for the most important statistical metrics.

4.3.1 Cross-correlation

Fig. 4.7 compares the cross-correlation for two different point pairs, P_1-P_5 (90 m apart) and P_1-P_6 (1 m apart) as obtained from six 99 s windows from a 600 s sample from our reduced model with fixed phase increments (Veers $_{\text{red, }\Delta\theta}$), from Veers' model with 20 frequencies (Veers $_{\text{red}}$), and from the full *TurbSim* simulation. To reduce noise and compare meaningful (rather than possibly extreme) values the results are presented

as averages of 100 realizations from different random seeds for both phase angles and phase increments.

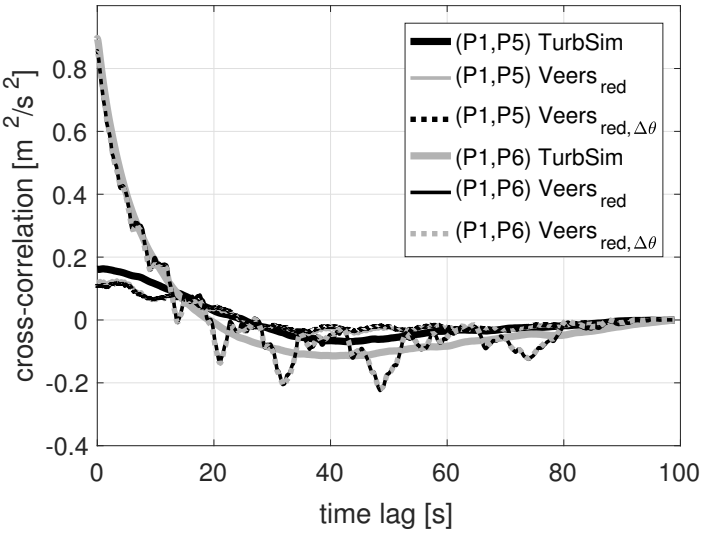

Figure 4.7: Wind speed cross-correlation for two point pairs generated from different models; a close pair (P_1,P_6) and a distant one (P_1,P_5).

As can be seen from the figure the cross-correlation in general agrees very well for both the close points and the distant point pair. The results from our implementation of Veers' model and from the phase increment model are almost identical and hence difficult to distinguish in Fig. 4.7. Note that the *TurbSim* data is smoother, presumably due to the significantly higher number of frequencies contained in the *TurbSim* data set.

Further investigation with the pair P_5 and P_{10}, two points close to each other but far away from the base point P_1 (not included in Fig. 4.7), shows that for all three models the cross-correlation is almost identical to the curve for P_1-P_6. This confirms that with our phase increment model the cross-correlation of the homogeneous turbulence field, and with it the length scale of spatial structures, is indeed only dependent on the distance between two points, but not on the two specific points themselves.

4.3.2 Covariance

Now we look at the covariance as a function of the distance between two points and compare data from *TurbSim* to the 20 frequency of Veers' model (Veers $_{\text{red}}$) and to our reduced model with phase increments (Veers $_{\text{red, }\Delta\theta}$). As above we use averages from 99 s windows out of 100 realizations of 600 s samples.

From Fig. 4.8 it can be seen that our implementation of Veers' model agrees well with the results from *TurbSim*. The phase increment model, however, yields slightly, but consistently less covariance. A more detailed investigation reveals the reason for this: the covariance depends on the cross-spectrum and thus the spectrum at each individual point. Consequently the discrepancy between the covariance functions is connected to the fact that Veers' model distorts the spectrum at each individual point, such that with Eq. 4.3 $|U_{mk}| = \sqrt{\tilde{S}_{mk}} \neq \sqrt{S_{mk}}$ (see discussion in section 4.2.1). When we replace S by the distorted spectrum $\tilde{S}$ at each particular point P_k in Eq. 4.8 all three curves do match. However, $\tilde{S}$ does not in fact represent the prescribed Kaimal spectrum. Thus we conclude that our phase increment model actually represents the desired covariance better than Veers' original model and *TurbSim*.

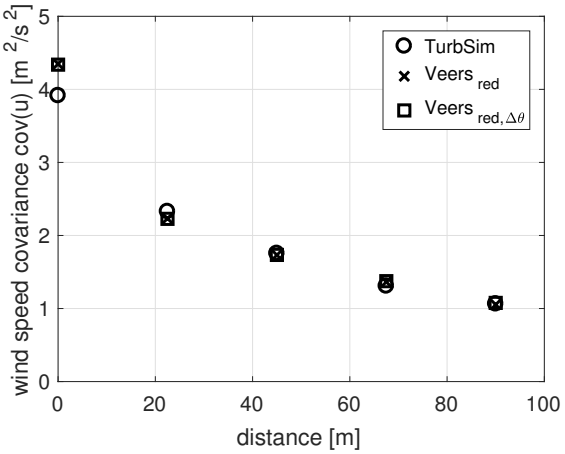

Figure 4.8: Wind speed covariance for points different distances apart.

4.3.3 Cross-spectrum

Next we compare the cross-spectrum, which is again obtained as the average spectrum from 100 realizations (from different random seeds). However, this time 6,000 s

were sampled to obtain sufficiently long data sets for a proper resolution of the low frequency components. Note that the same set of 20 frequencies $[f_k] \in [1/600, 5]$ Hz are used for both the 20 frequency (Veers $_{\text{red}}$) and the phase increment (Veers $_{\text{red, }\Delta\theta}$) implementations. Hence the $T = 6,000$ s signal repeats after 600 s. The spectrum is binned into discrete bins of frequencies f_m equal to the logarithmically spaced frequencies initially used to generate the wind speed time series. Fig. 4.9 shows a comparison of the cross-spectra estimates for different point pairs obtained through Welch's periodogram method employed on the full 6,000 s samples with no extra windowing (Welch, 1967). We study the base point, and its closest neighbor (P_1-P_6); the base point and a point far away (P_1-P_5); and a point pair close together, but far away from base point (P_5-P_{10}). For reference, the prescribed Kaimal spectrum S is included, as well as the analytic cross-spectrum obtained by:

$$S_{ij} = Coh\,\sqrt{S_{ii}S_{jj}} \tag{4.9}$$

from the (auto-) spectra $S_{ii} = S$ and the coherence function Coh as defined by the standard IEC 61400-1, Ed. 3 (2005).

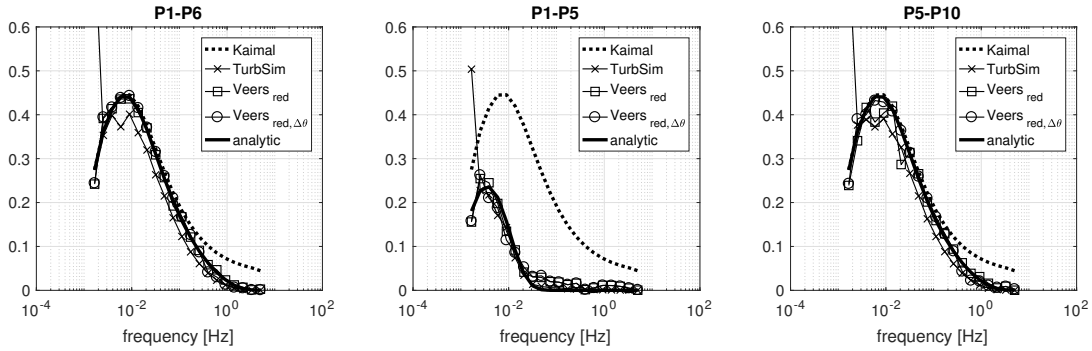

Figure 4.9: Wind speed cross power spectral density for three point pairs from different models, together with the analytic results (Eq. 4.9) and the prescribed Kaimal auto-spectrum. Left: the base point, and its closest neighbor. Middle: the base point and a point far away. And right: a point pair close together, but far away from base point.

Again, the phase increment model (Veers $_{\text{red, }\Delta\theta}$) in all cases reproduces the analytic spectrum well with only 20 random variables. This time, however, the *TurbSim* results do not match as well. The reason is that *TurbSim* chooses the lowest frequency f_1 and the frequency bin width Δf such that $\Delta f = f_1 = 1/T$, and thus uses a wider

frequency band for the first bin compared to our logarithmically spaced bins. When re-binning to the logarithmic range this results in excess power (and an artificial peak) in the first bin and hence less power in higher frequency bins. Note, however, that this is an artifact of the discrete spectrum and the frequency binning, and not a discrepancy in the underlying data.

4.3.4 Outlook: wind turbine rotor blade loads

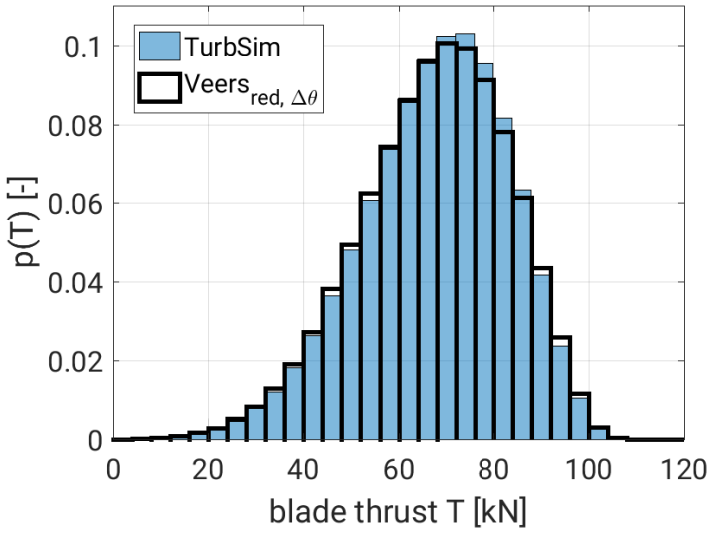

Figure 4.10: Blade thrust load probability distribution from BEM model based on wind fields generated with either *TurbSim* or from the reduced order Veers model with constant phase increments.

To further assess the validity of the reduced order wind model, loads were calculated for one single blade on a three bladed $R = 35$ m diameter wind turbine rotor spinning at a tip speed ratio $\lambda = 6.1$. Loads were obtained at $\Delta t = 0.1$ s time steps through a simple blade element momentum model supplied with wind generated either from *TurbSim*, or from our reduced model with fixed phase increments (Veers $_{\text{red, }\Delta\theta}$) on a 15×15 grid of data points over the rotor disc. The hub height is set to $h_{hub} = 90$ m, with the hub height mean wind speed $\bar{u} = 12$ m/s, power law wind shear with power law exponent $a = 0.2$ (according to Jonkman and Kilcher (2012)), and IEC normal turbulence model, class A (IEC 61400-1, Ed. 3, 2005). Fig. 4.10 shows the probability distribution $p(T)$ of thrust loads T on one blade calculated from 100 realizations of a

600 s wind field. *TurbSim* used the full set of roughly 3,000 frequencies at each of the 15×15 grid points. The reduced order model, on the other hand, relied on only 20 frequencies with all 100 realizations generated one set of fixed phase increments. It can be seen, that the reduced order model, although relying on significantly fewer random variables ($N_R = 6.75 \cdot 10^5$ versus $N_R = 20$ for each realization, see Tab. 4.1), produces almost the same load probability distribution.

4.3.5 Discussion

As shown by the results presented in this section the phase increments wind model presented in section 4.2.2 can reproduce important statistics (both of a wind field, as well as for resulting wind loads) with the same accuracy as the full model. At the same time, the phase increments model requires significantly less random variables. As indicated by Fig. 4.6 the phase increments model does *not* produce identical spatial structures with each realization, even thought a large part of the spatial randomness is neglected is Eq. 4.8. This further illustrates the method's ability to retain important stochastic information.

The results from sections 4.3.1-4.3.3 are generated from a set of 100 different phase increments generated from 100 different random seeds. This was necessary because, due to the random equations, it was not possible to compare the results from a single realization. This might have resulted in uncharacteristically bad (or good) agreement only by the chance of comparing 'bad' (or 'good') realizations. Instead only the averages over multiple realizations could be compared. For a stochastic analysis as outlined in the introduction, however, only a very limited set of phase increment realizations would be used. Hence, some part of the randomness of the wind field will be lost. This is the price to be payed for using a reduced order model. In section 4.2.2 we justify this choice. The results, particularly Figs. 4.6 and 4.10, support the notion that a very limited set of phase increment realizations, or even a single one, can be sufficient. It is still to be determined, however, how many sets will actually be necessary for adequate results, and how the associated reduction in randomness influences the relevant output quantities, e.g. for a wind turbine analysis the resulting loads, especially the probability of extreme loads. Preliminary results for wind turbine blade loads calculated from a Blade Element Momentum model indicate that only one single set of phase increments is sufficient to obtain almost the

same statistical load distribution as from the conventional analysis based on standard *TurbSim* wind fields.

4.4 Conclusions

Stochastic analysis and uncertainty quantification are generally very active fields of research in engineering with the developed methods increasingly adopted by industry. To enable practitioners to apply these methods to wind turbine aerodynamics and more generally wind loading analysis on various structures, we presented a new method, which significantly reduces the number of random variables used in the wind model. This reduction is critical, because the computational effort of the common stochastic solutions is very sensitive to the number of random variables involved.

The model introduced here employs a separation of the temporal (correlation in time) and spatial (coherence in space) part of the random dimension of turbulent wind. While the temporal part is still determined from random variables, the spatial part is collapsed into deterministic phase increments. Thus the number of random variables is reduced by several orders of magnitude compared to the commonly used model developed by Veers and implemented in *TurbSim*, currently the (de facto) standard tool for synthetic wind generation. A comparison of the most important stochastic metrics (cross-correlation, covariance, auto- and cross-spectrum) showed that the reduced order model based on phase increments still reproduces these metrics as accurately as Veers' equations or *TurbSim*. Moreover, preliminary results were presented, which indicate that the reduced order wind model based on phase increments also preserves wind turbine blade loads well. A detailed study quantifying the impact of using deterministic phase increments on the overall statistics of wind turbine loads is yet to be carried out. Subsequent to the implementation of this reduced order wind model in a full wind turbine simulator, which is the focus of ongoing work, these ultimate questions can be addressed.

Chapter 5

Fast Analysis of Unsteady Wing Aerodynamics via Stochastic Models

This chapter is a slightly corrected version of a paper first published as:
Fluck, Manuel and Crawford, Curran: "*Fast Analysis of Unsteady Wing Aerodynamics via Stochastic Models*", AIAA Journal, **2016**, article in advance;
DOI: 10.2514/1.J054983

In this paper we derive stochastic solutions for a very simple Lagrangian vortex model with linear aerodynamics. We model only one spanwise vortex element, and are concerned only with the auto-correlation. Thus we deal with a simple aerodynamic model and focus on deriving the basics of a stochastic solution. We present and validate two approaches:

(A) A new, time resolved polynomial chaos expansion, and
(B) the Fourier-Galerkin method, similar to (A), but based on Fourier basis functions (complex exponentials).

See Appendix C.4.1 for further information regarding the MATLAB code used to generate results for this section.

Abstract

Lifting surfaces often operate in highly unsteady inflow conditions, such as gusty wind or waves. These inflows are unsteady on many time scales and have to be considered stochastic processes. For fluid dynamics practitioners, this leads to a challenge: how can long term, random design loads (e.g. fatigue or 20-year return extreme) be quantified efficiently? The conventional approach involves analysis of a large set of short term inflow realizations and extrapolates the results to long term loads via their assumed probability distributions. However, this requires separately solving many simulations. This is computationally expensive and presents a handicap, especially in early design stages (optimization), where rapid evaluations of candidate designs and performance gradients are required. To tackle this problem, we introduce two alternative stochastic methods: one based on a Galerkin projection onto Fourier modes, and the other based on a polynomial chaos expansion. This approach enables us to carry the randomness though the solution process to directly obtain a stochastic result. Thus, long term loads can be directly constructed from the stochastic solution, without having to analyze specific realizations of the inflow inputs. The new processes are illustrated and discussed with an example based on a rectangular wing lifting line model.

Nomenclature

A	wing geometry parameter, m
B	current bound circulation coefficient
C	previous bound circulation coefficient
$\mathbb{C}^n$	n-dimensional complex number space
c_l	sectional lift coefficient
E	expected value operator
$\mathcal{F}$	Fourier space
$\boldsymbol{f}$	$= [f_k]$, k-th Fourier frequency, Hz
G_i	geometry term for i-th element, 1/m
$\boldsymbol{g}$	$= [g_k]$, solution series Fourier coefficients, m^2/s
$\hat{\boldsymbol{g}}$	$= [\hat{g}_r]$, solution PCE coefficients, m^2/s
i	$= \sqrt{-1}$, imaginary unit
K	number of frequencies
L	$= \{\Lambda_{mn}\}$, a set of multiple multi-indices
$\mathbb{N}_0$	set of integers
P	set of chaos polynomials
$\mathcal{P}$	polynomial chaos space
p	polynomial order
R	number of polynomial chaos functions
T	$= 1/f_1$, sample period
u_∞	inflow speed, m/s
$\boldsymbol{u}$	$= [u_k]$, inflow Fourier coefficients, m/s
$\hat{\boldsymbol{u}}$	$= [\hat{u}_r]$, inflow PCE coefficients, m/s
Var	variance operator
w	induced velocity, m/s
α_g	geometric angle of attack, rad
Γ_i	circulation of i-th vortex element, m^2/s
δ_{ij}	Kronecker delta
Λ	$= \{\lambda_k\}$, a multi-index
σ	standard deviation operator
Φ_k	k-th Fourier basis function
$\boldsymbol{\xi}$	$= [\xi_k]$, random number
Ψ_r	r-th multivariate PCE function
ψ_{λ_k}	λ_k-th univariate PCE function
$\boldsymbol{\Omega}$	stochastic sample space
$\boldsymbol{\omega}$	$= [\omega_k]$, k-th Fourier frequency, rad/s
*	conjugate complex
[ ]	a vector, matrix, or interval
{ }	a set
| |	absolute value
$\langle \square, \square \rangle$	an inner product

5.1 Introduction

Various types of wings, and lifting surfaces in general, operate in highly unsteady apparent inflow conditions where the driving physics (wind, waves) have to be considered stochastic: e.g. low speed/ low altitude aircraft during take-off or landing (Etkin, 1981; Patel and Kroo, 2006) and wind turbines (Milan et al., 2013) in the turbulent conditions of the atmospheric boundary layer, or floating marine systems (ship sails (Le Maître et al., 1999), floating wind turbine blades (Karimirad, 2014; Graf et al., 2016), tidal turbine blades (Gant and Stallard, 2008; Shives, 2011)) rolling in waves and thus subject to highly unsteady relative inflow. For preliminary analysis and design optimization of these lifting surfaces, where fast solution times are paramount to allow the quick analysis of multiple candidate designs, Lagrangian vortex models are often employed (Junge et al., 2010; Fluck et al., 2010; McWilliam et al., 2013b; Aubin et al., 2016). While full time-domain CFD simulations based on a discretized solution of the Reynolds Averaged Navier Stokes (RANS) equations potentially offer a high fidelity analysis, their high costs in terms of computational demand as well as pre- and post-processing time (mesh generation, quality control, etc) is often prohibitive for their use in early design stages. On the other hand, Lagrangian vortex models, such as e.g. a lifting line model (Prandtl, 1918, 1919; Phillips and Snyder, 2000), represent the lifting surface and the flow around it as a set of vortex elements, which are advected with the flow. These models offer medium fidelity results. They are relatively fast to solve and do not require any meshing, while still flexible enough to model even unconventional geometries (Fluck and Crawford, 2014). Moreover, Lagrangian methods may achieve accuracy similar to RANS solutions, as the latter often struggle with an numerically accurate resolution of the complicated physics involved.

When working with stochastic unsteady inflow conditions long time series have to be simulated to capture extreme evens. As an example, wind turbine standards (such as IEC 61400-1, Ed. 3 (2005)) base the load analysis on ten-minute simulations, which are required at many different wind speeds for 22 different load cases, each repeated six times with different random seeds for the turbulent inflow field. This results in a very large number of ten-minute simulations. But even with this, extrapolation to extreme loads is a delicate exercise and results can vary by a large amount (Moriarty, 2008; Burton et al., 2011). Zwick and Muskulus (2015) for example showed recently

that when basing a wind turbine analysis on six ten-minute wind speed simulations a difference of up to 34% occurs in the ultimate load results for the most extreme 1% of seed combinations. Moreover, recent research (Tibaldi et al., 2014) indicates that turbine loads extracted even from 20 different ten-minute wind fields generated from 20 different random seeds for each wind speed vary greatly. Often load variations from different random seeds dominate effects from design parameter changes – obviously a severe problem, especially when concerned with gradient-based optimization where obtaining reliable design variable gradients is vital.

Clearly, all these factors call for longer or more simulations based on more random seeds to accurately capture extreme events. However, the simulations are usually run in time-stepping solvers based on blade element momentum (BEM) theory. These solvers achieve solution times of up to 0.1 real time, i.e. 1 minute of simulation time to obtain ten minutes of (real) wind turbine operation. For the various different load cases and wind speeds prescribed by the standards this adds up to about 1 hour for one candidate design for on-shore turbines. When looking at floating structures with high-dimensional combined load cases of wind and wave data from different directions the situation gets even worse, requiring an even higher number of simulations (Graf et al., 2016).

Having to perform many and/ or long simulations to capture unsteady effects renders optimization for unsteady conditions difficult, since here the computational cost for each design evaluation is critical. However, reverting to a much faster steady-state study is dangerous as extreme load responses are not captured accurately and fatigue loads and unsteady power output may be misrepresented. Picking up our example of wind power again, Zhou et al. (2016) show that the peak power fluctuation for wind turbines can reach 22% of its average. Hence a steady state optimization potentially fails to find a solution close to the 'real' (unsteady) optimum. To tackle this dilemma the available model has to be extended, such that the full set of unsteady inflow conditions with all extreme loads can be modeled, while keeping the computational cost down. To do so, we will present a stochastic lifting line model, which will include stochastic unsteady effects, while keeping the computational effort low.

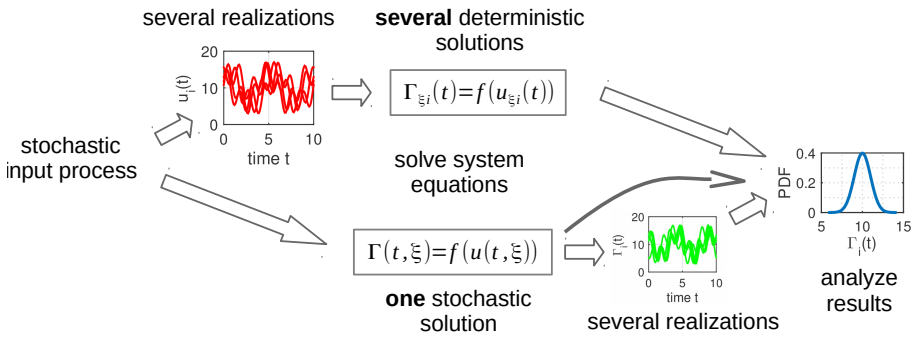

Figure 5.1: Alternate solution methods. Top route: conventional with realisations generated before solution; Bottom route: the new process with a stochastic solution.

When dealing with systems in turbulent wind or relative motions driven by waves, the wind/ waves are usually represented by a stochastic model, typically specified in the frequency domain by the governing standards (Burton et al., 2011; Faltinsen, 2005). However, instead of dealing with the notion of stochasticity during the system modeling, several realizations of the stochastic input wind/wave field are usually generated from different random seeds at the outset of the simulation (Karimirad, 2014). This means instead of using the abstract stochastic equations describing the wind/ wave fields, several concrete deterministic time-series are computed; see Fig. 5.1, upper path. While the benefit of this approach is its ability to use standard time-marching simulation codes, it removes the advantages of a stochastic description during the system modeling phase. Consequently, an analysis of many different realizations is required (Zwick and Muskulus, 2015), which leads to the problematic increase of computational cost discussed earlier.

In this paper we assume that a spectral model exists that describes the source term (i.e. the inflow) adequately. Form there on we demonstrate two ways of conducting the analysis of the system model in the stochastic space (lower path in Fig. 5.1). This will eliminate the need for multiple realizations of the input flow while retaining stochastic properties and thus the effects captured with different random seeds. Hence the costly time-domain analysis for various different random seeds is avoided and unsteady optimization based on Lagrangian vortex models becomes feasible. The aim of this work is to derive two different stochastic solutions for the aerodynamic system equations. The first method, polynomial chaos expansion (PCE), has been used to deal with stochastic models, particularly in the field of uncertainty quantification. However, the

available literature (e.g. Ghanem and Spanos (1991); Le Maître et al. (2001); Le Maître (2006); Sudret (2007); Najm (2009); Constantine et al. (2009)) deals with stochastic but constant boundary conditions or system parameters, i.e. random variables. Our problem, on the other hand, is concerned with a stochastic time varying source term, i.e. a random process. To the authors knowledge, this has not been addressed yet in the engineering literature. The second method, a stochastic Galerkin projection onto Fourier modes, is a combination of two well-know techniques. Again, while both parts, Fourier expansion and Galerkin projection, are well-known, the combination of both is novel as it retains the stochastic dimension of the problem. Thus it can be used to obtain a stochastic solution to a problem driven by a stochastic time varying source term.

In the following we will focus on unsteady aerodynamics in turbulent wind. Here the governing design standard (IEC 61400-1, Ed. 3 (2005)) requires the use of a spectral wind model (Veers or Mann model) to describe the inflow. It is well known that these models do not fully capture the detailed physics of 'real' wind (Mücke et al., 2011; Morales et al., 2012; Emeis, 2012; Park et al., 2015), and more advanced models are available, e.g. (Stresing and Peinke, 2010; Morales et al., 2012). Nonetheless, spectral models have been widely accepted for years as an adequate compromise between accuracy, generality, complexity, and computational cost (Nielsen et al., 2007; Lavely et al., 2012), with the incurred inaccuracy covered by safety factors included in the design. In the sequel we are not going to challenge the wind model prescribed by the standard, but work with the established model and focus on introducing the new stochastic method.

In section 5.2 the basic mathematical concepts will be revisited. Section 5.3 will take a lifting line model, apply the stochastic concepts introduced before, and thus arrive at a novel stochastic lifting line model. Here we only use a very simple horseshoe lifting line model to illustrate the method. Thus, the focus is on a concise introduction of the new concept, rather than blurring the fundamental ideas in a complicated aerodynamic model. Nonetheless the novelty of the approach will become apparent: through the projection on a stoachstic space the random dimension of the problem, introduced through the random source term, is retained up to the final solution for the blade loads. Thus, the statistics of the aerodynamic loads can be extracted directly and quickly from a single (stochastic) solution, the deterministic analysis of multiple realizations becomes unnecessary, and long term loads become accessible for

optimization. Eventually a more involved lifting line (or other aerodynamic model) can be analyzed similarly, and by introducing a hydrodynamic model the results are equally applicable to unsteady relative motions driven by waves, aeroelastic calculations, or any other stochastically driven simulations. This, however, will be left for other work. For now, section 5.4 concludes with some key results, followed by discussion of limitations, and a brief study of the computational costs in the light to our long term goal: an implementation of the presented fundamentals to a complete multidisciplinary stochastic wind turbine model.

5.2 Background: basic concepts

In this paper two related stochastic solutions to the lifting line equations are suggested. Both alternatives rely on a stochastic Galerkin projection as well as the stochastic formulation of the driving source term. Both, the stochastic Galerkin projection itself, as well as the stochastic description of the source term, are known concepts, which will only be reviewed briefly in this section to set the stage. The emphasis will be on the next section, where the novel combination of both concepts is introduced to project aerodynamic system equations onto a stochastic space and thus arrive at our principle goal: a stochastic solution of wing loads to directly arrive at long term loads without having to analyze multiple realizations deterministically.

5.2.1 Stochastic Galerkin projection

Both the discussed alternatives presented in the sequel are based on a stochastic Galerkin projection, which projects a stochastic equation onto a random space spanned by stochastic basis functions. Thus a system of deterministic equations for the solution's coordinates in the stochastic space is obtained. This leads to a split between the stochastic and the deterministic part of the equation: the stochasticity is contained in the basis functions, while the coordinates are purely deterministic and can therefore be solved for in a deterministic manner.

Let f_i and f_j be any two functions in $\mathbb{C}^n$, and let f^* denote the conjugate complex function of f. For the projection we define the inner product of two functions over

some space Ω, $\boldsymbol{x} \in \Omega$, with the weighting function $p(\boldsymbol{x})$:

$$\langle f_i(\boldsymbol{x}), f_j(\boldsymbol{x}) \rangle = \int_{\Omega} f_i(\boldsymbol{x}) f_j^*(\boldsymbol{x}) p(\boldsymbol{x}) \, d\boldsymbol{x} \tag{5.1}$$

With appropriate scaling s the scaled functions $s_i f_i$ and $s_j f_j$ constitute a set of orthonormal functions if $\langle s_i f_i(\boldsymbol{x}), s_j f_j(\boldsymbol{x}) \rangle = \delta_{ij}$, where δ_{ij} is the Kronecker function. In a stochastic sample space Ω with an appropriate probability measure p replacing $\boldsymbol{x}$ with a random number $\boldsymbol{\xi} \in \Omega$ gives convenient extra properties to this inner product: for a certain set of functions $\Phi(\boldsymbol{\xi})$, the so-called chaos polynomials, $p(\boldsymbol{\xi})$ is the probability distribution of the random variable $\boldsymbol{\xi}$ and hence the inner product equals the expected value operation $\langle \Phi_i, \Phi_j \rangle = \mathrm{E}[\Phi_i, \Phi_j]$. Note, however, that for this property to hold the chaos polynomials have to be chosen according to the probability function $p(\boldsymbol{\xi})$. Examples include Legendre polynomials for uniformly distributed random variables; Hermite polynomials for normally distributed random variables. For a full list see e.g. Xiu and Karniadakis (2002).

Similar to the usual Galerkin projection, two steps are executed in the stochastic Galerkin projection to find an approximate solution to some system of governing equations:

1. Restrict the approximate solution to lie within some finite dimensional Hilbert space $\mathbb{K}$ equipped with an inner product as defined in Eq. 5.1, and spanned by a set of independent basis functions. For the stochastic case these are stochastic basis functions.
2. Employ the inner product of Eq. 5.1 to project the governing equation onto the space $\mathbb{K}$ to obtain a system of equations for the coordinates of the solution in $\mathbb{K}$. For a linear governing equation and orthogonal basis functions this will result in a decoupled system of equations.

The key here is to find a space $\mathbb{K}$ that provides a sufficient approximation of the solution with a convenient number of basis functions. By virtue of its definition the inner product (an orthogonal projection) will then ensure an optimal approximation, i.e. a solution where the residual is orthogonal to all provided basis functions (Naylor and Sell, 1971).

5.2.2 The stochastic source term and the approximation space

Before looking at our lifting line example we need to clarify what approximation space $\mathbb{K}$ to use. For the cases considered here the only source of stocasticity is in the turbulent inflow. Hence we follow the argument by Le Maître and Knio (2010) and assume that the stochastic solution will be in the same stochastic space as the stochastic input. But how is the stochastic input best described?

The atmospheric sciences provide various different, more or less involved, and more or less accurate stochastic models for atmospheric wind (e.g. Kantz et al. (2004); Nielsen et al. (2007); Kleinhans et al. (2008); Morales et al. (2012); Calif et al. (2013) to only cite a few). If we want to present a method applicable to industrial wind turbine design, however, we are constrained by the governing design standard (IEC 61400-1, Ed. 3, 2005). This standard uses either Veers' (Veers, 1988) or Mann's (Mann, 1994, 1998) wind model, and thus considers the homogeneous, stationary, and Gaussian description associated with these spectral models adequate (Nielsen et al., 2007). Since the goal of this work is to develop an improved method for wind turbine design optimization, and since the design is governed by the IEC standard, we adopt the prescribed models without further discussion, although we acknowledge that there are more accurate models available.

The wind models from the IEC standard typically build up the turbulent inflow u_∞ as a truncated Fourier series of K discrete frequencies ω_k, each with discrete amplitude u_k and a random phase angle $\pi\xi_k$, where each $\boldsymbol{\xi} = [\xi_k]$ is a vector of mutually independent uniformly distributed random variables in the sample space $\boldsymbol{\Omega} = [-1, 1]^K$ and the imaginary unit $i = \sqrt{-1}$:[10]

$$u_\infty(t_n, \boldsymbol{\xi}) = \sum_{k=0}^{K} u_k e^{i(\omega_k t_n + \pi\xi_k)} \tag{5.2}$$

Note that this formulation intrinsically provides the possibility to separate time and random variables into a function purely of time $T(t_n)$ and a pure random function $X(\boldsymbol{\xi})$:

$$u_\infty(t_n, \boldsymbol{\xi}) = T(t_n)X(\boldsymbol{\xi}) \tag{5.3}$$

[10] N.B.: Here and in the following we implicitly assume the correct symmetry of amplitudes u_k and frequencies ω_k in order to arrive at real valued wind speed u_∞.

This will become important later, when we move to a chaos polynomial representation. For simplicity and clear notation we use a one-dimensional homogeneous inflow here, but the extension to a three dimensional (correlated) field is possible following for example Veers (1988).

In general and for the specific case in Eq. 5.2 the inflow $u_\infty(t_n, \boldsymbol{\xi})$ is a stochastic process. Based on a wind spectrum (e.g. the isotropic Kaimal spectrum from the IEC standard (IEC 61400-1, Ed. 3, 2005), which defines u_k for each ω_k) and a specific set (i.e. a realization) $\boldsymbol{\xi}_0$ a wind speed time series sample $u_\infty(t_n, \boldsymbol{\xi}_0)$ can readily be generated via the inverse Fourier transform. Veers (1988) and Mann (1994, 1998) explain this process in detail. Note that each time series $u_\infty(t_n, \boldsymbol{\xi}_0)$ is based on one specific realization $\boldsymbol{\xi}_0$. It is only one specific sample path of the random process $u_\infty(t_n, \boldsymbol{\xi})$, and each sample path may be more benign or more extreme depending on the specific phase angle combination determined by $\boldsymbol{\xi}_0$. Thus, extreme events will only be encountered if by chance an extreme combination of random variables is realized in $\boldsymbol{\xi}_0$ and the time series is long enough to capture all possible component interactions. Once a sample path is generated a deterministic wind time series is available which can be processed conveniently in the usual deterministic fashion. However, this is also where the problem discussed around Fig. 5.1 arises: Using one sample path cuts down the multitude of stochastic possibilities into one single sample path. To still capture extreme events, a very long time series or many different realizations (from different $\boldsymbol{\xi}_i$) have to be analyzed (the upper path in Fig. 5.1; (Zwick and Muskulus, 2015)) this is costly and time consuming. The remainder of this paper will look at a simple example and introduce a new alternative (lower path in Fig. 5.1) to avoid this problem.

5.3 A stochastic horseshoe vortex system

In this section the aerodynamic equations of a horseshoe vortex model will be solved in the stochastic space. As a base line the classic (deterministic) lifting line model will be briefly summarized first. Then the lifting line equation is projected onto a space spanned either by complex exponentials or polynomial chaos functions to obtain the solution in the stochastic space (lower path in Fig. 5.1). The first method is a new combination of a Fourier expansion with a Galerkin projection, which avoids the

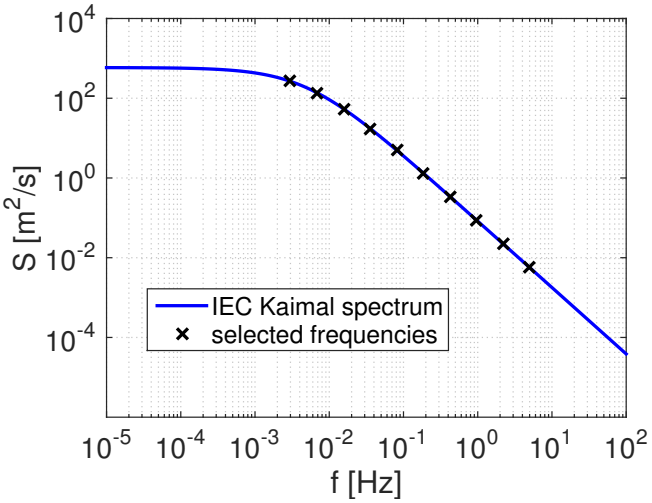

Figure 5.2: The Kaimal spectrum for turbulent wind inflow.

linearization typically required in Fourier-based approaches and enables the random phase shifts to be passed directly through the system equations. We call this method the Fourier-Galerkin (FG) solution. The second approach, known as a polynomial chaos expansion (PCE), was introduced by Ghanem and Spanos (1991) in the context of finite element analysis. It has recently become more popular for uncertainty quantification when dealing with stochastic inputs or stochastic system parameters (Sudret, 2007; Najm, 2009) and has also been applied to fluid dynamic problems. However, so far only static stochastic parameters (e.g. unknown but constant viscosity (Le Maître et al., 2001) or oscillation amplitude (Le Maître, 2006)) and stochastic boundary or initial conditions (e.g. unknown temperature (Constantine et al., 2009)) have been considered. To our knowledge a polynomial chaos representation has not been used with stochastic processes (like wind or waves) where the stochastic input evolves through time and preserving the auto-correlation becomes important. A detailed assessment on which of the two stochastic methods is more suitable for our problem of wind turbine optimization is left to forthcoming work.

5.3.1 The deterministic baseline model

A simple lifting line vortex system as introduced by Prandtl (1918, 1919), extended with shed wake elements representing the wing loading history, will be used as an example to show a way of retaining the stochasticity through the solution process of

an unsteady aerodynamic analysis. Thus the need to analyze multiple realizations is avoided. For the sake of clarity when illustrating the stochastic approach the simplest possible model of a rectangular lifting surface in unsteady flow is used (Fig. 5.3). This model can readily be extended to more complicated wing and wake geometries by simply adding more vortex elements (Anderson Jr, 1985; Phillips and Snyder, 2000). For the time being, the wake element positions are assumed fixed. Adding more elements and relaxing the wake positions will not fundamentally change the presented method, it will merely add more unknowns – with solution strategies known (Anderson Jr, 1985; Phillips and Snyder, 2000). For now we assume small angles of attack α_g, small induced velocities w, and thus linear airfoil properties ($c_l = 2\pi(\alpha_g + w/u_\infty)$) and arrive at the well known lifting line equation (for details see e.g. Anderson Jr (1985); Phillips and Snyder (2000)):

$$\Gamma_0(t_n) = A \cdot u_\infty(t_n) + B \cdot \Gamma_0(t_n) + C \cdot \Gamma_0(t_{n-1}) \tag{5.4}$$

with $u_\infty(t_n)$ the unsteady inflow speed, $A = c\pi\alpha_g$, $B = c\pi(G_1 + G_2 + G_3 - G_5)$, $C = c\pi(G_1 + G_4 + G_5)$ and G_i geometry terms representing the induced downwash according to Biot-Sarvart's law from each vortex element Γ_i at the middle of the lifting line (Γ_0). For a specific realization $\boldsymbol{\xi}_0$, and thus one specific deterministic wind speed time series $u_\infty(t_n, \boldsymbol{\xi}_0)$, Eq. 5.4 is solved in the well known deterministic time-stepping manner:

$$\Gamma_0(t_n) = \frac{A \cdot u_\infty(t_n) + C \cdot \Gamma_0(t_{n-1})}{1 - B} \tag{5.5}$$

Through the Kutta–Joukowski equation the wing lift can then be obtained immediately.

In the next two sub sections Eq. 5.5 will be solved directly for the stochastic inflow $u_\infty(t, \boldsymbol{\xi})$ in general.

5.3.2 Expansion in time (Fourier-Galerkin solution)

To retain the stochasticity though the model equations let us first look at the wing load solution $\Gamma_0(t_n, \boldsymbol{\xi})$, now a function of time t and the random variable $\boldsymbol{\xi}$. We can express Γ_0 in some suitable stochastic space as a linear combination of some basis function $\Phi_l(t_n)$, unknown coefficients g_l, and a random phases $e^{i\pi\xi_l}$ for each basis

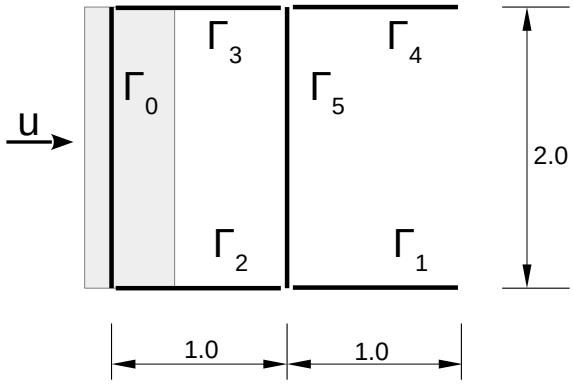

Figure 5.3: Unsteady horseshoe vortex system. Dimensions in meters.

function: [11]

$$\Gamma_0(t_n, \boldsymbol{\xi}) = \sum_{l=0}^{L} g_l \, \Phi_l(t_n) \, e^{i\pi\xi_l} \tag{5.6}$$

In general Eq. 5.6 requires $L \to \infty$. However, if the input is adequately represented by a truncated Fourier series of $K < \infty$ terms then setting $L = K$ gives a fair approximation for an engineering solution. Moreover, the Fourier series of the input Eq. 5.2 itself can be understood as a projection of the inflow time series $u_\infty(t)$ onto the K-dimensional complex Hilbert space $\mathcal{F}$ spanned by the K Fourier modes $e^{i\omega_k t_n}$ and equipped with an inner product as defined in Eq. 5.1. Hence it is straight forward to express the solution Γ_0 in the same space $\mathcal{F}$:

$$\Phi_l(t_n) = \Phi_k(t_n) = e^{i\omega_k t_n} \tag{5.7}$$

Since the models we will consider do not introduce any extra randomness themselves (besides the one introduced through the input), the output random variables $\boldsymbol{\xi}$ are drawn from the same sample space $\boldsymbol{\Omega}$ (Le Maître and Knio, 2010). Thus we have $\xi_l = \xi_k$. With this we can express the system equation 5.4 in terms of the basis functions Φ:

$$\sum_{k=0}^{K} g_k \, \Phi_k(t_n) \, e^{i\pi\xi_k} = A \sum_{k=0}^{K} u_k \Phi_k(t_n) \, e^{i\pi\xi_k} + B \sum_{k=0}^{K} g_k \, \Phi_k(t_n) \, e^{i\pi\xi_k} + C \sum_{k=0}^{K} g_k \, \Phi_k(t_{n-1}) \, e^{i\pi\xi_k} \tag{5.8}$$

[11] Again we assume the correct symmetry in order to arrive at real valued circulations Γ_0.

As we chose $K < \infty$ this restricts the solution to a finite dimensional approximation space, which is the first step of the Galerkin projection. Hence the problem is recast from finding the bound circulation $\Gamma_0(t_n)$ as a function of time directly to determining the solution coordinates g_k. The advantage is that we do retain the stochasticity, as Eq. 5.8 does not require obtaining one specific realization of $\boldsymbol{\xi}$ anymore.

We recognize that, at least in the case of our linear example, $\Phi_k(t_{n-1}) = \Phi_k(t)e^{-iw_k\Delta t}$ with $\Delta t = t_n - t_{n-1}$. With the inner product $\langle \square, \Phi_k(t_n) \rangle$ over $\Omega = [0, T]$, both sides of Eq. 5.8 can now easily be projected onto $\mathcal{F}$ to complete the Galerkin projection. By canceling $e^{i\pi\xi_k}$ on both sides this transforms Eq. 5.8 directly into a system of K decouppled equations for the K unknown solution coordinates g_k:

$$g_k = A\, u_k + B\, g_k + C\, g_k e^{-iw_k\Delta t} \tag{5.9}$$

Thus the solution for g_k is straight forward:

$$g_k = \frac{A}{1 - B - Ce^{-iw_k\Delta t}} u_k \tag{5.10}$$

Pluging this back into Eq. 5.6 yields the sought stochastic expression of the time series of the bound circulation as a function of the random variable $\boldsymbol{\xi}$. The orthogonality of the Fourier modes Φ guarantees an optimal solution approximation, because the residual will be orthogonal to the truncated solution retained in $\mathcal{F}$.

To obtain this result we used a Galerkin projection of the governing equation onto the Fourier modes of the inflow. Hence we refer to this method as *Fourier-Galerkin* (FG) method in the sequel. In contrast to the usual deterministic solution for one specific inflow realization (Eq. 5.5) the stochastic nature of the inflow (e.g. the forcing wind) is now carried through the equations and contained in the load solution of $\Gamma_0(t_n, \boldsymbol{\xi})$. This is obtained by decoupling the random phase angles from the time history. Consequently the realization of different sample paths is postponed until after the solution of the governing equation of the stochastic system, i.e. until after the computationally expensive part of the solution of the system (cf. lower path in Fig. 5.1). Note that increasing the complexity of the problem will naturally render Eq. 5.6 more complicated, but it will not not change the method per se.

For independent uniformly distributed $\boldsymbol{\xi}$, mean and variance of the wing load $\Gamma_0(t_n, \boldsymbol{\xi})$ are readily (i.e. without even creating a set of realizations) available from the expression of Eq. 5.6 and the solution from Eq. 5.10:

$$\mathrm{E}\left[\Gamma_0\right] = g_0 \tag{5.11}$$

$$\mathrm{Var}\left[\Gamma_0\right] = \sum_{k=1}^{K} |g_k|^2 \tag{5.12}$$

with $|g_k|$ denoting the absolute value of the complex g_k.

Note that after the projection Eq. 5.10 is no longer a function of time. In contrast to the PCE method introduced next, here the time dimension is pulled into the Fourier modes $\Phi_k(t_n)$, and the solution coefficients $\boldsymbol{g} = [g_k]$ themselves are not only independent of the stochastic component $\boldsymbol{\xi}$, but also independent of time. Hence with one solve of Eq. 5.10 for $\boldsymbol{g}$ the evolution of the vortex system for all time steps (up to the longest period of the input expansion for the wind signal) is obtained at once. For a steady state inflow, where the Fourier series contains only the DC term but no phase angles, this method thus collapses to the deterministic solution.

On first glance these results may seem like merely a Fourier transform as known for a linear time-invariant systems from control theory. But this similarity only arises in our simple example, where the projection of Eq. 5.8 results in a set of decoupled linear equations. In fact, when going through Eqs. 5.6–5.10 we never assumed linearity and actually have two important advantages:

1. In contrast to a conventional Fourier transform, the approach presented here is similarly valid for a non-linear system. The only difference is that for non-linear systems projecting Eq. 5.8 will not result in decoupled coefficients g_k but rather turn Eq. 5.10 into a coupled system of equations, requiring a matrix inversion for the solution. With a limited number K of coupled equations this inversion should not pose any serious problem.
2. In future work the constant mean inflow speed, included in Eq. 5.6 via the zero frequency $\omega_0 = 0$, can easily be replaced with another random variable, representing the long term variation of the short term mean inflow speed. In contrast to a conventional Fourier transform, the proposed method can thus be expanded directly to a long time analysis (e.g. for 20-year extreme loads)

without significant extra effort.

Moreover, our stochastic Fourier-Galerkin method, in contrast to the usual Fourier transform, also retains the stochastic dimension of the problem, and hence provides a means to obtain a stochastic solution.

5.3.3 Expansion of random phase angles (polynomial chaos expansion)

Instead of using the Fourier representation of the inflow directly, the input and the output can also be cast into a polynomial chaos expansion (PCE), see e.g. Le Maître and Knio (2010). Since time and stochastic variables can be separated as established in Eq. 5.3 we can write:

$$u_\infty(t_n, \boldsymbol{\xi}) = \sum_{r=0}^{R-1} \hat{u}_r(t_n)\, \Psi_r(\boldsymbol{\xi}) \tag{5.13}$$

and

$$\Gamma_0(t_n, \boldsymbol{\xi}) = \sum_{r=0}^{R-1} \hat{g}_r(t_n)\, \Psi_r(\boldsymbol{\xi}) \tag{5.14}$$

with the multivariate polynomial chaos (PC) $\Psi_r(\boldsymbol{\xi})$ of the K-dimensional vector of independent random phases $\boldsymbol{\xi} = [\xi_k]$, and the input and output coefficients $\hat{u}_r(t_n)$ and $\hat{g}_r(t_n)$ respectively. As before the same random variables are used for the input and output. Based on these expansions, the PCE method then follows the same Galerkin procedure as the Fourier-Galerkin solution presented above. The construction of the chaos polynomials Ψ_r will be outlined next, before the expansion of Eqs. 5.13 and 5.14 will be applied to our lifting line example.

For concise notation let $\Lambda = \{\lambda_1, \ldots, \lambda_K\} = \{\lambda_k\}$ denote a multi-index, with each $\lambda_k \in \mathbb{N}_0$. Further, let $L(p) = \{\Lambda_{mn}\}$ be a set of multi-indices for a set of polynomials of order up to p, such that (cf. Le Maître and Knio (2010)):

$$L(p) = \left\{ \Lambda_{mn} \;\middle|\; \sum_{k=1}^{K} \lambda_k = n;\ n \leq p \right\} \tag{5.15}$$

with $m \in \mathbb{N}$ a numbering index without particular order for different multi-indices for any constant n. Combining the indices mn into $r \in \{0, \ldots, R-1\}$ for notational convenience, the r-th multivariate PC is then given by

$$\Psi_r(\boldsymbol{\xi}) = \Psi_{mn}(\boldsymbol{\xi}) = \prod_{\lambda_k \in \Lambda_{mn}} \psi_{\lambda_k}(\xi_k) \tag{5.16}$$

with

$$R - 1 = \frac{(K+p)!}{K!p!} \tag{5.17}$$

Since the phase angles $\pi\xi_k$ in the stochastic input are distributed uniformly in $[-\pi, \pi]$ Legendre polynomials are are chosen for $\psi_{\lambda_k}(\xi_k)$ to achieve optimal (exponential) convergence of the series (Xiu and Karniadakis, 2002). With the normalization factor $q_{\lambda_k} = \sqrt{\lambda_k + 0.5}$ the univariate Legendre polynomials are:

$$\psi_{\lambda_k}(\xi_k) = \frac{q_{\lambda_k}}{2^{\lambda_k}} \cdot \sum_{l=0}^{\lambda_k} \binom{\lambda_k}{l}^l (\xi_k - 1)^{\lambda_k - l} (\xi_k + 1)^l \tag{5.18}$$

Choosing $K = 3$ and $n = 2$ as example we get $\{\Lambda_{m2}\} = \{\{2,0,0\}, \{0,2,0\}, \{0,0,1\}, \{1,0,1\}, \{1,1,0\}, \{0,1,1\}\}$ leading to e.g. $\Psi_{12} = \psi_2(\xi_1) = \frac{1}{2} q_2 (3\xi_1 - 1)$ and $\Psi_{42} = \psi_1(\xi_1)\psi_1(\xi_3) = q_1^2\, \xi_1 \xi_3$.

By construction the chaos polynomials are orthonormal and the set P of all polynomials Ψ of order up to p derived through Eq. 5.16:

$$P = \left\{ \bigcup_{\Lambda_{mn} \in L(p)} \Psi_{mn} \right\} \tag{5.19}$$

forms an R-dimensional PC basis of the sample space Ω (for $p \to \infty$). Since the Legendre polynomials (a special case of Jacobi polynomials) are member of the Askey polynomial scheme this basis is complete (Xiu and Karniadakis, 2002). Thus the expansions of Eqs. 5.13 and 5.14 express the input and the output via coordinates ($\hat{u}$ and $\hat{g}$ respectively) in a stochastic Hilbert space $\mathcal{P}$, equipped with the inner product as defined in Eq. 5.1, and spanned by P. Through the Cameron–Martin theorem (Cameron and Martin, 1947), extended to general PC by Xiu and Karniadakis (2002), the expansions converge in $\mathcal{P}$ in the L_2 sense for $p \to \infty$. For any practical application R has to be limited to a finite number. Eq. 5.17 determines this number based on the

count of random variables K and the order of the polynomial p.

Setting Eq. 5.2 equal to Eq. 5.13, employing the inner product $\langle \square, \Psi_r(\boldsymbol{\xi}) \rangle$, and taking advantage of the orthonormality of the PC approximation basis, the input wind series coefficients $\hat{u}_r$ of Eq. 5.13 are now readily found:

$$\hat{u}_r(t_n) = \sum_{k=1}^{K} u_k e^{i\omega_k t_n} \left\langle e^{i\pi\xi_k}, \Psi_r(\boldsymbol{\xi}) \right\rangle \tag{5.20}$$

Note that we use the stochastic inflow formulation $u_\infty(t_n, \boldsymbol{\xi})$, and not just one wind speed sample path $u_\infty(t_n)$. Thus all possible realizations are projected into the stochastic space through the stochastic variable $\boldsymbol{\xi}$. Next the PC definitions of Eqs. 5.13 and 5.14 are inserted into the governing equation 5.4. This yields:

$$\sum_{r=0}^{R-1} \hat{g}_r(t_n)\, \Psi_r(\boldsymbol{\xi}) = A \sum_{r=0}^{R-1} \hat{u}_r(t_n) \Psi_r(\boldsymbol{\xi}) + B \sum_{r=0}^{R-1} \hat{g}_r(t_n)\, \Psi_r(\boldsymbol{\xi}) + C \sum_{r=0}^{R} \hat{g}_r(t_{n-1})\, \Phi_k(\boldsymbol{\xi}) \tag{5.21}$$

In contrast to Eq. 5.8 for the Fourier-Galerkin method, where the evolution through time is contained in the time dependent basis functions $\Phi(t)$, here the basis functions $\Psi(\boldsymbol{\xi})$ contain the stochastic part of the solution, while time is carried by the coordinates $\hat{u}(t)$ and $\hat{g}(t)$ respectively. By choosing $R < \infty$ (and thus requiring $p < \infty$) we again restrict the solution to a finite dimensional approximation space. This completes the first step of the Galerkin projection for the PCE method.

Next Eq. 5.21 is projected onto $\mathcal{P}$ by applying the inner product $\langle \square, \Psi_r(\boldsymbol{\xi}) \rangle$ again. Taking advantage of the orthogonality of the chaos polynomials, this reduces Eq. 5.21 to a system of R decoupled deterministic equations in the chaos coordinates $\hat{g}_r$:

$$\hat{g}_r(t_n) = A\hat{u}_r(t_n) + B\hat{g}_r(t_n) + C\hat{g}_r(t_{n-1}) \tag{5.22}$$

Since the input wind coefficients $\hat{u}_r(t_n)$ are known through Eq. 5.20 this can now be solved in the same way as the original unsteady lifting line equation (Eq. 5.4) for each chaos coordinate $\hat{g}_r$ at each instance t_n:

$$\hat{g}_r(t_n) = \frac{A\hat{u}_r(t_n) + C\hat{g}_r(t_{n-1})}{1 - B} \tag{5.23}$$

The orthogonality of the chaos polynomials Ψ guarantees an optimal solution approximation as the truncated part of the solution will be orthogonal to the solution retained in $\mathcal{P}$.

Inserting these coefficients into Eq. 5.14 again yields the stochastic response $\Gamma_0(t_n, \boldsymbol{\xi})$ to any wind forcing $u_\infty(t_n, \boldsymbol{\xi})$. Since the time domain is now no longer contained in the basis functions Ψ_r, the coordinates $\hat{\boldsymbol{g}}(t_n) = [\hat{g}_r(t_n)]$ are a function of the (discrete) time t_n. Hence $\hat{g}_r(t_{n+1})$ has to be found from $\hat{g}_r(t_n)$ through Eq. 5.23 in the usual time-stepping manner. However, now a short analysis time (just long enough to overcome initialization effects in the wake and to capture the smallest relevant frequency) is sufficient to produce all possible responses, and thus all possible wing loads from all possible phase combinations.

Note that $\hat{\boldsymbol{g}}(t_n)$ still contains all possible realizations and one solution for a short time (just long enough to overcome initialization effects in the wake and to capture the smallest relevant frequency) is sufficient to produce all possible responses, and thus all possible wing loads from all possible phase combinations. Again we have traversed to the lower path in Fig. 5.1.

As earlier, the mean and variance of the wing load $\Gamma_0(t_n, \boldsymbol{\xi})$ can be directly computed. Since $\boldsymbol{\xi}$ is independent of t_n and $\mathrm{E}[\Psi_r] = \prod \sqrt{q_{\lambda_k}} = 0.5^{K/2}$ only for $r = 0$ but zero in all other cases we obtain:

$$\mathrm{E}[\Gamma_0] = \sum_{r=0}^{R-1} \mathrm{E}[\hat{g}_r \Psi_r] = \sum_{r=0}^{R-1} \mathrm{E}[\hat{g}_r]\,\mathrm{E}[\Psi_r] = 0.5^{K/2} \mathrm{E}[\hat{g}_0] \tag{5.24a}$$

Moreover, by construction, the covariance $Cov[\hat{g}_r \Psi_r, \hat{g}_s \Psi_s] = 0$ for $r \neq s$, and $\mathrm{E}[\Psi_r^2] = 0.5^K$. Hence:

$$\mathrm{Var}[\Gamma_0] = \sum_{r=0}^{R-1} \mathrm{Var}[\hat{g}_r \Psi_r] = \sum_{r=0}^{R-1} \mathrm{E}\left[\hat{g}_r^2\right] \mathrm{E}\left[\Psi_r^2\right] - (\mathrm{E}[\hat{g}_r]\,\mathrm{E}[\Psi_r])^2 = 0.5^K \cdot \left(\sum_{r=0}^{R-1} \mathrm{E}\left[\hat{g}_r^2\right] - (\mathrm{E}[\hat{g}_0])^2 \right) \tag{5.24b}$$

In the same way higher order moments can be calculated, and as before the load probability distribution can be directly obtained from the coefficients $\hat{\boldsymbol{g}}_r$ via an

appropriate reconstruction method (Williams, 2012).

5.4 Results and discussion

The FG and the PCE methods were applied to solve the lifting line model presented in section 5.3.1. In this section, after looking at the approximation basis used to obtain the stochastic solutions, the obtained results will discussed and compared to the traditional deterministic time marching solution. As discussed earlier, the relevant design standard (IEC 61400-1, Ed. 3, 2005) bases wind turbine analysis on spectral wind models. Consequently, we limit our discussion here to a comparison of our stochastic results to deterministic results obtained from wind samples generated from TurbSim (Kelley and Jonkman, 2007), a full-field numerical turbulence simulator developed in line with the IEC standard, and the the most common tool for wind input generation in the wind energy industry.

5.4.1 The approximation basis

In accordance with the IEC standard (IEC 61400-1, Ed. 3, 2005) both presented methods express the system equations in a finite dimensional approximation space, $\mathcal{F}$ or $\mathcal{P}$, spanned by Fourier exponentials or PC functionals respectively. In both cases, the number of basis functions depends on K, the number of terms contained in the Fourier series representing the input, i.e. the driving wind in our example. To limit the computational effort when obtaining a solution it is necessary that these spaces provide an adequate approximation with a limited number of dimensions. Hence it is vital that the input can be represented with few terms. Discussing how a turbulent wind field can be represented with few frequencies while still preserving the relevant qualities, mainly the wind speed variance, probability distribution, and the correlation functions (spatial and temporal), is beyond the scope of this paper and is left to a forthcoming publication. However, to confirm feasibility of the presented methods in the following, one such reduced order representation is introduced here.

Fig. 5.4 shows the variance of the time series synthesized at 10 Hz from the reduced order model with an increasing number K of logarithmically spaced frequencies $\boldsymbol{f} = \boldsymbol{\omega}/(2\pi) = [f_k] \in [0.003, 5]$ Hz from the IEC Kaimal spectrum, a common model in the wind industry (IEC 61400-1, Ed. 3, 2005; Burton et al., 2011). For comparison the

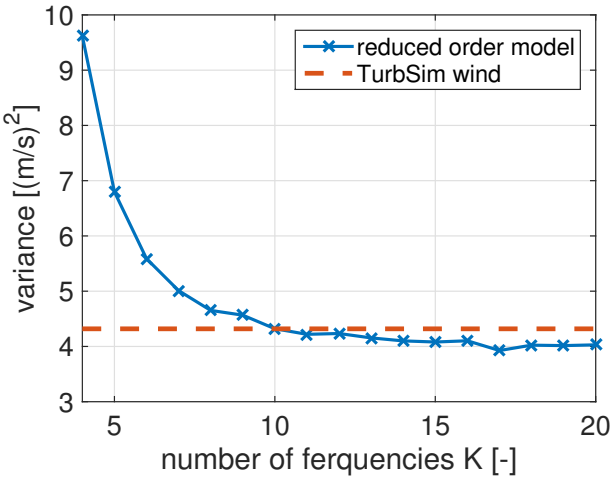

Figure 5.4: Variance of a wind speed time series synthesized from the reduced order model with an increasing number of frequencies.

variance of a 10,000 s wind sample generated though TurbSim (Kelley and Jonkman, 2007) is included. TurbSim uses the full spectrum, and for a wind field sampled at 10 Hz for 10,000 s roughly $5 \cdot 10^4$ frequencies are needed for the full synthesis. From the figure it can be seen that for $K = 10$ the variance is almost converged for the reduced order model. Moreover, note that because only a limited frequency range is covered, the reduced order model converges to a smaller variance than the TurbSim results, which contain a larger frequency range. Hence $K = 10$ frequencies with $f_k \in [0.003, 5]$ Hz will be used for the following study. The highest frequency $f_K = 5$ Hz is set according to the dynamic response of the considered structure and the highest relevant structural frequency. For wind turbines Bergami and Gaunaa (2014) show that 5 Hz captures all relevant fatigue contributions well. The stochastic methods assessed in the following are based on analyzing short time windows (just long enough to cover the development of wake dynamics) with random phase angles. For this work, we chose a window length of $d = 100$ s, assuming that the wake elements older than this will usually not have any meaningful influence on the model anymore. With a period $T = 1/f_1 \approx 5.56$ min well above d the chosen frequency range ensures a signal without repetitions. Later on the sample length d may be further reduced, leading to the possibility of increasing f_1. In this case the variance left over from all $f < f_1$ has to be included, e.g. by a stochastically varying mean for each short window. Again, details are postponed to a forthcoming paper. At this point it is only relevant that turbulent wind can adequately be represented with a few frequencies.

Fig. 5.5 shows the probability distribution (PDF) and auto-correlation function (ACF) for a single point wind speed time series, as well as the time series itself. As above the original time series generated in TurbSim. The mean wind speed was set to $\bar{u} = 10$ m/s and type A (normal) IEC turbulence characteristic was simulated 100 m above ground leading to a turbulence intensity of $TI = \sigma[u]/\bar{u} = 21\%$. Again, 10,000 s were sampled at 10 Hz ($5 \cdot 10^4$ frequencies) from the Kaimal spectrum. As above the reduced order model is synthesized at 10 Hz from ten logarithmically spaced frequencies. Fig. 5.5a shows the time series for the first 100 s of the original TurbSim wind data and the reconstruction from the reduced order model. By inspection it can be seen that the two signals exhibit similar stochatic properties and time scales of variation; however, the two signals do not match, and the mean of neither agrees with the 10 m/s prescribed. Yet, this is not surprising, because: i) the random phase angles from the reconstruction do not match the original ones and ii) correct statistics (such as the mean) can not be extracted from such an individual short sample of realized wind speeds. To evaluate these properties 500 different 100 s long realizations were generated from the reduced model with 500 different sets of phase combinations. Fig 5.5b shows that this replicates almost exactly the same PDF as the original 10,000 s TurbSim wind sample (mean: 9.998 m/s and 9.999 m/s; standard deviation: 2.078 m/s, 2.082 m/s for TurbSim and reduced order model respectively). Fig 5.5c shows that the auto correlation is well matched, too. Here the mean ACF from the 500 short sets of the reduced order model is compared to the mean of the ACF from 100 consecutive sets of 100 s duration drawn from the TurbSim data set.[12]

Note that the data analyzed in Fig. 5.5 is generated from one long (TurbSim) or 500 short (reduced order model) realizations, respectively. For the methods presented here, however, the input will never be turned into a concrete realization. Instead, the solution is based on the stochastic representation of the short input. This facilitates the significant reduction in frequencies needed to represent the wind's dynamics; while with a conventional approach the range of frequencies is determined by the duration of the sample (f_{min}) and the sampling rate (f_{max} or Nyquist frequency), the stochastic approach is only limited by the sampling rate. The frequencies to be included in the reconstructed signal then need to be only chosen such that the signal variance

[12] The TurbSim output file limits the maximum duration to 9,999.999 s, hence 100 sets of 100 s. On the other hand, due to fewer random numbers, 500 realizations were necessary for converged statistics in the reduce order data.

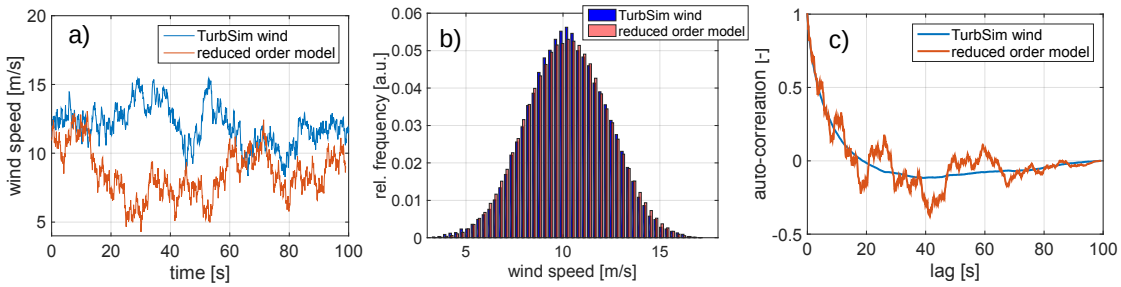

Figure 5.5: Comparison of the original and reconstructed wind speed data: a) time series (only first 100 s); b) probability distribution; c) auto-correlation for $k = 10$.

is reproduced over many different realizations (with many different random seeds). Again, a detailed discussion of this is beyond the scope of this paper and hence postponed to a forthcoming separate publication.

5.4.2 Stochastic solution

In accordance with the arguments above, we base our analysis on a spectral wind model as prescribed in the relevant design standard IEC 61400-1, Ed. 3 (2005). Consequently we deal with Gaussian inflow and are thus content with second order statistics only. We recognize that this (just as the standard methods in current wind turbine engineering) does not capture all details of atmospheric wind, particularly the "fat tails" encountered in wind speed probability distributions. However, for the time being we consider the Gaussian model sufficient based on the following two arguments: Firstly, our main concern is not the detailed analysis of a specific load case, but a qualitative comparison of different candidate designs for optimization. While it would be convenient to include the details of the tails of a the load distribution, they are secondary to a consistent qualitative comparison. Currently design optimization neglects long term loads at large. As our engineering tools evolve incrementally, a even simplified quantitative long term load comparison is already a significant improvement over the current status quo. Secondly, for the analysis (and certification) of a final design the IEC standard established safety factors, which are included to cover residual uncertainties, such as e.g. uncertainties incurred with inaccurate representation of non-Gaussian effects. While this is surely not an ideal solution, it is a convenient and thus well established procedure in engineering practice, which will be equally valid with our stochastic models. Having said this, however, we acknowledge that Gaussian

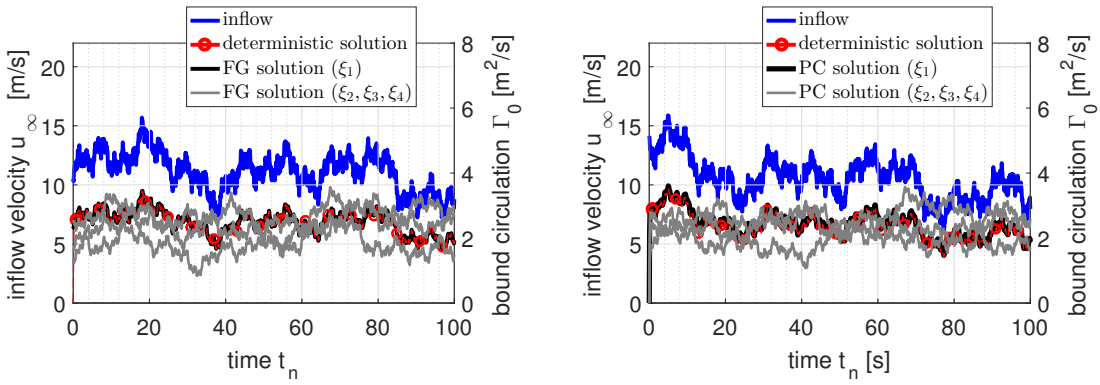

Figure 5.6: The evolution of the bound circulation from the deterministic solution and for different realizations of the stochastic solution. Left: the Fourier-Galerkin solution; Right: polynomial chaos solution

wind models can not be the final step. Further improvement is mandatory in the future.

To illustrate the proposed stochastic methods, the lifting line system from Fig. 5.3 is first solved via the conventional deterministic time-stepping approach (Eq. 5.5), then via the stochastic Fourier-Galerkin solution (Eqs. 5.6 and 5.10) and finally via the stochastic polynomial chaos method (Eqs. 5.14 and 5.23). For a first comparison, the input wind field is directly generated from Eq. 5.2. Following the discussion above, ten input frequencies are used. This results in $K = 10$ random variables for the stochastic models. For the PC method multidimensional Legendre polynomial chaos functions up to order $p = 4$ are used, since this choice was found to reproduce the input (Eq. 5.13) well. A time step of 0.1 s is used according to $f_K = 5$ Hz. At this stage, the projection integrals over the ten-dimensional domain $\Omega = [-1, 1]^{10}$ from the inner product in Eq. 5.20 are solved simply via a crude Monte Carlo integration (Davis and Rabinowitz, 1984) with 10^6 random points in each dimension.

Fig. 5.6 compares the first 100 s of the resulting bound circulation $\Gamma_0(t_n, \boldsymbol{\xi}_k)$ as obtained from either the deterministic solution or through four realizations for $k \in \{1, 2, 3, 4\}$ of the PCE or FG equations respectively. The corresponding inflow $u_\infty(t_n, \boldsymbol{\xi}_{k=1})$ as well as the deterministic solution (Eq. 5.5) based on this inflow are overlaid. With $\boldsymbol{\xi}_1$ (the same phase angles that generating the inflow realization) both methods reproduce the deterministic solution almost exactly (cf. Fig. 5.6 'deterministic solution' and 'FG solution (ξ_1)' or 'PC solution (ξ_1)' respectively). But instead of only

Table 5.1: Comparison of mean in and variance from different models.

	$\mathrm{E}[\Gamma_0]$ (rel. error)	$\mathrm{Var}[\Gamma_0]$ (rel. error)
units	$[\mathrm{m}^2/\mathrm{s}]$ ([-])	$[(\mathrm{m}^2/\mathrm{s})^2]$ ([-])
deterministic model	2.232	0.213
Fourier-Galerkin model	2.232 (-0.002 %)	0.216 (+1.350 %)
polynomial chaos model	2.231 (-0.012 %)	0.219 (+3.146 %)

a single solution to one specific time series, both the FG and the PCE solution contain all possible phase angle combinations. Thus, instead of solving for several time series with different random seeds $\boldsymbol{\xi}_k$ one stochastic solution is enough. If needed, different solutions realizations can be obtained *a posteriori* by realizing different phase angles (e.g. Fig. 6 solutions for ξ_2 - ξ_4).

As for the input wind the wing load PDF and ACF from the stochastic models (not shown) from 100 different realization of $d = 100$ s reproduce the deterministic curves very well (in the same way as for the wind input shown above). However, once the stochastic solution is available the construction of the PDF is unnecessary as the expected value, variance, as well as higher moments can be directly calculated via Eqs. 5.12 and 5.24 respectively. As an illustration a deterministic wing load solution was calculated for the full 10,000 s TurbSim wind sample (with all $5 \cdot 10^4$ frequencies) used as base line in section 5.4.1. Table 5.1 compares the mean $\mathrm{E}[\Gamma_0]$ and the variance $\mathrm{Var}[\Gamma_0]$ of the deterministic solution to the results from the FG and PCE methods. As can be seen, the metrics from a 10,000 s long deterministic solution can be extracted directly from *one* short-time stochastic solve almost exactly.

5.4.3 Computational costs

The proposed stochastic methods solve an unsteady aerodynamic problem driven by a random process input in the stochastic space. Thus they eliminate the need for costly analysis of several longer samples to obtain long term fatigue and extreme load estimates (Fig. 5.1, upper path). Instead, the signal PDF can be obtained from one stochastic solution and thus the long term extreme loads can be estimated directly

(Fig. 5.1, lower path). This offers the potential to save significant computational effort and thus make a long term load analysis accessible in an optimization routine.

At this point a quantitative comparison of the computational costs is difficult for two reasons. Firstly our example is implemented in an experimental Matlab code, where an easy development of the method had higher priority over computational efficiency. Thus any time analysis would be significantly biased by code efficiency. Secondly the considered simple horseshoe lifting line model provides a small system of equations, which is solved very quickly (within milliseconds on a laptop computer). This was intended and helpful for developing the method, but naturally makes performance differences difficult to quantify. A detailed quantitative comparison of computational costs is hence left for a forthcoming publication based on the study of a full wind turbine rotor model. However, while a *quantitative* comparison is deferred to future work, a *qualitative* discussion will show the potential of the new stochastic approach. The computational cost for both, the deterministic and the PCE method, scales with the number of equations and the number of time steps to be solved. We will look at both in the sequel.

Required simulation time

As an example, Fig. 5.7 shows the evolution of the wing load variance $Var[\Gamma_0(t < T)]$ with an increasing sample size T for the deterministic solution based on three different 20,000 s realizations of the TurbSim wind sample from above. Obviously, due to the (long term) unsteady effects in the wind, the sample variance converges only slowly. At 10,000 s the fist and third sample differ by 2.51 %, and even for T between 10,000 s and 20,000 s significant variance fluctuations are found. This puts the error found in Table 5.1 into perspective, and shows again that very long simulations are necessary to obtain a sufficiently accurate variance estimate to be able to extrapolate the results to long term extreme loads. For a computationally more demanding model a similar convergence behavior can be expected (Tibaldi et al., 2014). For long term load estimates this results in a considerable computational effort to obtain reliable results – presumably too much effort to be feasibly within an optimization routine. The stochastic methods, on the other hand, yield the load variance instantaneously from only one stochastic solution of limited length, only long enough to advect start-up transients downstream.

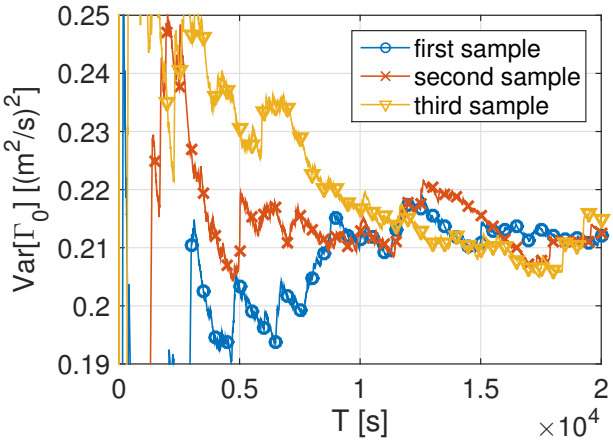

Figure 5.7: Evolution of the wing load variance with an increasing sample length of the deterministic solution.

Number of equations

In the deterministic case a single equation is solved for a long time sample with many time steps and/ or several different realizations from different random seeds to make sure rare extreme events are captured. The stochastic methods, on the other hand, require the solution of several equations. Therefore only a short time sample needs to be evaluated, because extreme events are inherently contained in the stochastic solution and random numbers are never realized. Thus generating different solutions from different random seeds is not an issue. The analyzed sample window needs to be only long enough to capture relevant wake effects, i.e. the time during which previous wing loads influence the current conditions. For illustrative purposes we analyzed a $d = 100$ s window in the example above. However, in most practical cases d will usually be much smaller. For a 10 m rectangular wing of aspect ratio 10 in 10 m/s inflow $d = 1$ s will cover the wake of ten chord lengths – presumably enough for most practical cases. Hence, the savings from fewer time steps required will in most cases far outweigh the increased computational costs from the additional equations. At this stage, significant additional computational costs are faced for the Monte Carlo integration of the projection from Eq. 5.20. However, in an optimization environment this will not be of greater concern since i) the projection has to be performed only once for a given wind input (it is not specific to the geometry to be analyzed and thus can be re-used), and ii) a significant speed-up can be expected by utilizing a more elaborate multidimensional integration technique.

For our simple example, the FG method results in a set of $K = 10$ decoupled

equations for the K frequencies. Since the time evolution is contained in the Fourier modes $\Phi_k(t_n)$ with the solution coefficients g_k independent of time, solving these K equations once yields the solution for all times. Hence a solution can be obtained very fast, comparable to solving only K time steps in the deterministic case.

After all, the feasibility of either stochastic method will be determined by the computational cost associated with the transition to the stochastic space, and whether this cost is smaller than the costs for several long realizations in the deterministic case. This will obviously be dependent on the specific equations associated with the model under consideration. A first test with a FG solution for a wind turbine blade showed significant acceleration potential in the range of several orders of magnitude.

5.5 Concluding remarks

In this paper we introduced two (different but related) new methods to solve aerodynamic load calculations under turbulent inflow. In line with the wind turbine design standard IEC61400-1 Ed. 3, the stochastic inflow is represented by a spectral model with random phase angles. Instead of solving several time series realizations, the new methods solve the governing equations in a stochastic space and hence retain the stochastic variables all the way to the final solution. Stochastic properties, such as mean load, load variance, and thus extreme and fatigue loads, are thus accessible directly from the stochastic solution without having to generate multiple realizations from different random seeds. A detailed derivation of both methods was given, including the necessary fundamentals regarding orthogonal basis functions and the stochastic Galerkin projection.

The efficiency of either of the proposed methods depends on the number of random variables. In the example case presented, this is the number of random phases, thus the number of frequencies included in the spectral model representing the inflow. It was shown that for a typical wind sample (obtained from TurbSim, a widely used numerical tool to generate synthetic wind speed data) the wind speed PDF and its auto correlation can be reproduced adequately with only ten frequencies.

Based on the example of a simple lifting line model it was shown that both suggested stochastic methods are capable of constructing the response for all possible

inflow realizations quickly from only one stochastic solution. This avoids the costly evaluation of multiple time series and will allow fatigue and extreme loads to be calculated quickly, thus enabling us to include these effects directly into an aerodynamic (or aero-structural) optimization routine in future work.

At this point, results of comparable accuracy are obtained from both stochastic models. Once more sophisticated (possible non-linear) system equations come into play a decision about which model is more favorable can be made. It is expected that this decision will eventually depend on the specific nature of the equations at hand and the details of the respective Galerkin projections involved in each stochastic method.

Chapter 6

A Stochastic Aerodynamic Model for Stationary Blades in Unsteady 3D Wind Fields

This chapter is a slightly corrected version of a paper presented at *The Science of Making Torque from Wind* (TORQUE 2016), Munich, Germany, October 5-7 2016. It was first published as:
Fluck, Manuel and Crawford, Curran: "*A stochastic aerodynamic model for stationary blades in unsteady 3D wind fields*", Journal of Physics: Conference Series, **2016**;
DOI: 10.1088/1742-6596/753/8/082009

In this paper we extend the stochastic models derived previously to a more complex Lagrangian vortex model, consisting of several spanwise vortex elements on the blade. We show that the stochastic model not only captures one-point (auto-correlation), but also two-point statistics (cross-correlation, covariance, cross-spectrum). We remain with linear aerodynamic equations, and study a translating blade in turbulent wind.

See Appendix C.4.1 for further information regarding the MATLAB code used to generate results for this section.

Abstract

Dynamic loads play an important roll in the design of wind turbines, but establishing the life-time aerodynamic loads (e.g. extreme and fatigue loads) is a computationally expensive task. Conventional (deterministic) methods to analyze long term loads, which rely on the repeated analysis of multiple different wind samples, are usually too expensive to be included in optimization routines. We present a new stochastic approach, which solves the aerodynamic system equations (Lagrangian vortex model) in the stochastic space, and thus arrive directly at a stochastic description of the coupled loads along a turbine blade. This new approach removes the requirement of analyzing multiple different realizations. Instead, long term loads can be extracted from a single stochastic solution, a procedure that is obviously significantly faster. Despite the reduced analysis time, results obtained from the stochastic approach match deterministic result well for a simple test-case (a stationary blade). In future work, the stochastic method will be extended to rotating blades, thus opening up new avenues to include long term loads into turbine optimization.

6.1 Introduction

Today, aerodynamic optimization of wind turbines faces two major challenges. First, the computational tools commonly at hand (BEM solvers) are inherently limited to planar rotor designs (Burton et al., 2011), while more flexible simulations, based on the full time-domain solution of the discretized Reynolds Averaged Navier Stokes equations (CFD methods), are too expensive to be viable for optimization (McWilliam et al., 2013a). Second, it is computationally difficult to include long term (fatigue and extreme) loads into the optimization loop (Graf et al., 2016), because this kind of analysis requires the simulation of long load samples in order to be able to extract consistent statistics and thus reliably extrapolate to long term loads. IEC 61400-1, Ed. 3 (2005), for example, bases the long term analysis of every load case on ten minute simulations, run at different mean wind speeds, each repeated six times with different random seeds for the turbulent inflow field. Obviously this results in a large number of ten-minute simulations. Still, it has been shown (Moriarty, 2008; Burton et al., 2011) that even with this many simulations, extrapolation to extreme loads is a delicate exercise and results may vary significantly. Zwick and Muskulus (2015) for example showed recently that when basing a wind turbine analysis on six ten-minute wind speed realizations a difference of up to 34% occurs in the ultimate load results for the most extreme 1% of seed combinations. Other recent research (Tibaldi et al., 2014) indicates that turbine loads extracted even from 20 different ten minute wind fields generated from 20 different random seeds for each wind speed vary greatly. Moreover, often load variations from different random seeds dominate effects from design parameter changes, obviously a severe problem, especially when concerned with gradient-based optimization where obtaining reliable design variable gradients is vital.

As a result of these two challenges, current wind turbine optimization is inherently limited, as it a) cannot explore unconventional, but potentially beneficial designs such as winglets, swept or downwind coning rotors, etc., and b) is blind to the important (Kareem, 2008) cost savings of modified long term loads and power production from different blade designs operating in unsteady conditions. For example, Zhou et al. (2016) show that the peak power fluctuation for wind turbines can reach 22% of its average. A steady state optimization potentially fails to find a solution close to the 'real' (unsteady) optimum.

Lagrangian vortex models (LVM) (Junge et al., 2010; Fluck et al., 2010; McWilliam et al., 2013b; McWilliam, 2015) based on Prandtl's lifting line theory (Prandtl, 1918, 1919) are an attractive solution to the first challenge. They are relatively fast to solve, but flexible enough for unconventional geometries, see e.g. Fluck and Crawford (2014). However, time stepping through multiple LVM solutions to obtain data for extrapolation to long term loads is not an option within the time budget of optimization. To tackle this dilemma, the available model has to be extended, such that the full set of unsteady inflow conditions with all extreme loads can be modeled, while keeping the computational cost down. To do so, we present a stochastic lifting line model to obtain long term loads and power output relatively quickly from a single stochastic solution. Besides a faster solution, the stochastic formulation potentially captures true extreme loads better than relying on the extrapolation of limited short term loads from short term time stepping simulations.

In this paper we present a stochastic blade load model, resolved with several span-wise lifting line elements in a stochastic unsteady (coherent) three dimensional wind field. Section 6.2 will give an introduction to the approach. Starting from a basic aerodynamic LVM blade model in its deterministic formulation (6.2.1) and the stochastic inflow formulation (section 6.2.2), the transition to the stochastic blade model with correlated wing blade sections will be presented (section 6.2.3). For clarity of the method and its presentation we direct our focus to a stationary blade. In section 6.3 we will compare the load time series as well as the statistics from a deterministic lifting line solution to the results from the proposed stochastic method. Moreover, the reduction of the computational cost will be discussed. Future steps will extended the model to stochastic unsteady aerodynamics simulations of a full wind turbine in operation.

6.2 Approach and methods

When dealing with wind turbine optimization, the driving wind inflow is usually represented by a stochastic model, typically specified in the frequency domain. However, instead of dealing with the notion of stochasticity during system modeling, several realizations of the stochastic input wind are usually generated prior to the simulation procedure (Karimirad, 2014). For wind turbine analysis several ten minutes wind speed

samples (deterministic blocks of frozen wind) are generated and then each analyzed consecutively (Burton et al., 2011). This means that instead of using the abstract stochastic equations, several deterministic time-series are obtained (see Figure 6.1, upper path). While the benefit of this approach is its ability to use standard (and more intuitive) deterministic, generally non-linear, time-marching simulation codes, it discards the advantages of a direct stochastic description during the system modeling phase.

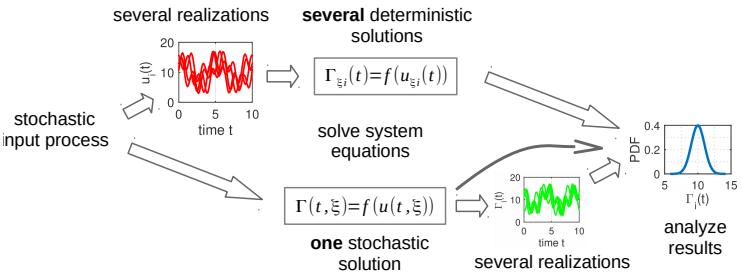

Figure 6.1: Alternate solution methods. Upper path: conventional with realizations generated before solution; Lower path: the new process with a stochastic solution.

In Fluck and Crawford (2016a, 2017b) we demonstrated two ways of conducting the system model analysis directly in the stochastic space, thus eliminating the need for multiple realizations of the inflow. Instead of the common practice of repeatedly solving the aerodynamic equations for multiple deterministic realizations (Figure 6.1, upper path) one single stochastic solution is sought (Figure 6.1, lower path). This stochastic solution will contain all possible realizations. Thus long term loads can either be extracted quickly from several realizations of the stochastic solution, or directly from the statistics of the solution's random variables. For the case of a very simple horseshoe vortex lifting line model of a stationary rectangular wing, resolved with a single spanwise lifting line element, we were able to retain stochastic properties and thus the effects captured with different random seeds within one stochastic solution. Obviously, the single spanwise element misses significant effects from the spatial variability and cross-correlation of the wind field and hence it omits the spacial coupling of the blade loads. In the remainder of this section we will introduce the necessary model components to arrive at a stochastic lifting line model for the coupled loads along wind turbine blades.

6.2.1 Aerodynamic model

For the blade load calculations, a LVM in unsteady lifting line formulation (Prandtl, 1918, 1919) will be used.[13] The vortex system is set up as indicated in Figure 6.2 with an arbitrary number N_b of bound (linearly spaced) elements. Trailing and shed elements of variable strength are included to capture shed vorticity and the resulting time lagged variation of the induced velocity from the inflow changes at the wing as well as the delayed vortex shedding downstream. The wake length N_t can be chosen freely. For the time being, wake element positions are assumed fixed and in the x-y-plane.

At each station I along the blade we assume small angles of attack $\alpha_{g,I}$, small induced velocities w_I, and thus use linear airfoil properties ($c_{l,I} = 2\pi(\alpha_{g,I} + w_I/u_\infty)$) to arrive at the well known unsteady lifting line equation:

$$\Gamma_I(t_n) = A_I \cdot u_{\infty,I}(t_n) + \sum_i \sum_j H_{I,ij} \cdot \Gamma_i(t_{n-j}) \tag{6.1}$$

With this equation we calculate the bound circulation (and thus load) $\Gamma_I(t_n)$ at each station I for each time step $t_n = n \cdot \Delta t$ implicitly from the current free stream wind at the respective station $u_{\infty,I}(t_n)$ and the previous blade loads $\Gamma_i(t_{n-j})$ at all wake stations i; here $A_I = c_I \pi \alpha_{g,I}$. The tensor $H_{I,ij}$ contains the Biot-Savart influence from each wake element ij onto the blade element I, as well as the coupling of the current wake strength and blade load history: $\Gamma_{t,ij} = \gamma_{ij} - \gamma_{(i-1)j}$ and $\Gamma_{s,ij} = \gamma_{ij} - \gamma_{i(j-1)}$ respectively, with $\gamma_{ij} = \Gamma_i(t_{n-j})$ (see Figure 6.2).

With a known, deterministic inflow u_∞ equation 6.1 can readily be solved with the common methods.

6.2.2 Stochastic wind model

To calculate blade loads, deterministic models use random, but correlated wind speed data $u_I(t_n, \boldsymbol{\xi}_I)$ generated in advance at many locations P_I over the rotor disc from adequately correlated realizations of the random vectors $\boldsymbol{\xi}_I$. In Veers' model (Veers,

[13] For a detailed introduction to lifting line models see Prandtl's original publications (Prandtl, 1918, 1919) or one of the many more recent works, e.g. Schlichting and Truckenbrodt (2000); Anderson Jr (1985); Phillips and Snyder (2000).

1988), which is widely used in industry (e.g. in NREL's *TurbSim* (Kelley and Jonkman, 2007)), the wind speed time series at each location P_I is generated though an inverse Fourier transform

$$u_I(t_n) = \sum_m V_{mI}\, e^{i(\omega_m t_n)} \tag{6.2}$$

Here each (complex) Fourier coefficients V_{mI} for each frequency ω_m at each location P_I is initially generated from the wind speed spectrum and an independent random variable ξ_{mI} (i.e. a random phase angle), uniformly distributed in $[0, 1]$. We implicitly assume correct symmetry of V_{mI} and m containing all necessary (positive and negative) frequencies in order to arrive at real valued wind speed u_I. To correctly model the coherence of the random wind field correlation of the Fourier coefficients at different locations is subsequently enforced via the coherence matrix (for details see e.g. Veers original publication (Veers, 1988)). With this procedure Veers' approach requires $N_R = N_I \cdot N_f$ independent random variables for N_I locations and N_f frequencies. Since the computational cost of our stochastic method is highly sensitive to the number of random variables N_R, we first split Veers' complex Fourier coefficients into amplitude and phase, $V_{mI} = \sqrt{S_m}\, e^{i\theta_{mI}}$, with $\theta_{mI} = 2\pi\xi_{mI}$ the (correlated) phases at each point and each frequency and the amplitude prescribed by the discrete wind speed power spectrum S_m. Next we split the phase angles into the phases at one arbitrary base point P_0 and a set of correlated phase increments: $\theta_{mI} = \theta_{m0} + \Delta\theta_{mI}$. Thus equation 6.2 becomes:

$$u_I(t_n) = \sum_m \sqrt{S_m}\, e^{i(2\pi\xi_m + \Delta\theta_{mI})}\, e^{i\omega_m t_n} \tag{6.3}$$

Now $\boldsymbol{\xi} = [\xi_m]$ is a single vector of uncorrelated random variables specified at one (arbitrary) base point P_0. The phase (and thus wind speed) correlation between the points P_I and P_0 is contained in the correlated phase increment vectors $\Delta\boldsymbol{\theta}_I = [\Delta\theta_m]_I$. Details of this reduced order wind model will be given in a forthcoming publication. In the following, we focus on the aerodynamic blade model and its stochastic solution.

With Veers' model one wind field realization is obtained from first generating independent phase vector realizations for all points and subsequently correlating the phase angles. Equation 6.3, on the other hand, finds one wind field realization with one random phase vector $\boldsymbol{\xi}$ at one base point P_0 only and a set of random phase increments $\Delta\boldsymbol{\theta}_I$ for each other point. For a stochastic analysis equation 6.3 has a major advantage: the generation of random phases angles and the correlation between two points is

now separated into $\boldsymbol{\xi}$ and $\Delta\boldsymbol{\theta}_I$ respectively. While all ξ_m are independent, $\Delta\boldsymbol{\theta}_I$ are correlated, which provides the opportunity to establish a reduced order model. If we assume that the random dimension of the wind field is sufficiently approximated by $\boldsymbol{\xi}$ only, than $\Delta\boldsymbol{\theta}_I$ can be considered a deterministic variable. This reduces the number of necessary random variables by several orders of magnitude. A detailed discussion of the consequences of this split between stochastic phases and deterministic phase increments is beyond the scope of this paper. A comprehensive study is currently underway and will be available shortly.

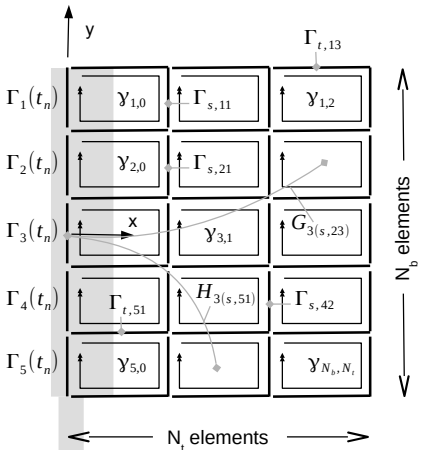

Figure 6.2: Illustration of the vortex system used to model blades loads.

Figure 6.3 shows a comparison of the input wind obtained from *TurbSim* and two realizations of the reduced order model for the wind speed at four points with the coordinates (horizontal, vertical): P_1 (1,0) m; P_5 (1,90) m; P_6 (0,0) m; P_{10} (0,90) m. By inspection, it can be seen that the properties of the wind seem to be reproduced well. Note that the reduced order model of equation 6.3 does not result in a complete determination of the spatial relation between wind speeds at different points, as the samples still contain different constructive/ destructive phase interference and thus gusts/ lulls at different instances in time. Both the theoretical details of this model as well as a comprehensive discussion of the resulting wind speed time series are beyond the scope of the present paper and will be discussed in a separate publication. Here, Figure 6.3 and the wing load results presented later shall suffice as justification to use this model.

6.2.3 Stochastic blade load model

For the stochastic solution we follow the process of stochastic projection (Fourier-Galerkin method) presented by Fluck and Crawford (2017b), expanded to the multi-element lifting line equation 6.1. We directly use equation 6.3 in the reduced order stochastic formulation with $\Delta\boldsymbol{\theta}_I$ understood as deterministic phase increments and $\boldsymbol{\xi}$

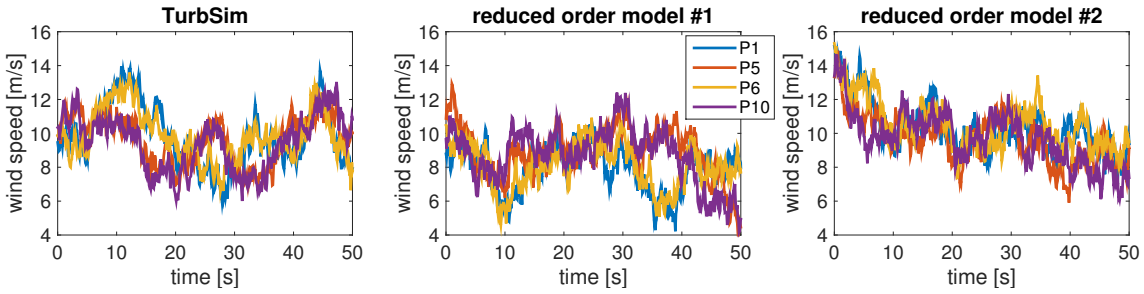

Figure 6.3: Samples of wind speed time series at four points generated from *TurbSim* and two different realizations of the reduced order model.

a random phase angle vector to represent the correlated random wind field. Similar as presented by Fluck and Crawford (2017b) the wing load can be expressed in terms of the same complex Fourier series as the inflow:

$$\Gamma_I(t_n) = \sum_l g_{lI} \Phi_l(t_n) e^{i \cdot 2\pi \xi_l} \tag{6.4}$$

with $\Phi_l(t_n) = e^{i\omega_l t_n}$. As fir the wind imput we implicitly assume correct symmetry and l containing all necessary modes (of positive and negative frequencies) in order to arrive at real valued wind speed u_I. Recognizing that thus $l = m$, equations 6.3 and 6.4 can be inserted into equation 6.1. With $t_n = n\Delta t$ and basic algebra we can write $\Phi_l(t_{n-j}) = \Phi_l(t_n)\Phi_l(-j\Delta t)$. Thus, after truncating the series to a reasonable number of frequencies N_f and projecting onto the basis functions $\Phi_l(t_n)$, we arrive at a system of equations in the stochastic space $I = 1...N_f$ (for a detailed derivation and a discussion of this method refer to Fluck and Crawford (2017b)):

$$g_{Il} = \sqrt{S_l} \cdot A_I e^{i\Delta\theta_{Il}} + \sum_i \sum_j H_{I,ij}\, g_{Il}\, \Phi_l(-j\Delta t) \tag{6.5}$$

Note that although equation 6.5 yields the coefficients g_{Il} of the stochastic solution (equation 6.4), it is a deterministic equation itself. Hence it can be solved with common (deterministic) approaches in the same way as equation 6.1. However, since the stochastic solution (equation 6.4) still contains the random vector $\boldsymbol{\xi}$, it contains all possible realizations. Hence this one solution contains all possible long term blade loads that can possibly result from any phase combination in the inflow wind (lower path in Figure 6.1).

At the moment linear airfoil properties are assumed. This results in equation 6.5 being conveniently decoupled for each frequency. Moving forward to the optimization of wind turbine blades in turbulent wind conditions two more steps are necessary. First, the equations need to be applied to a rotating blade. This will be straight forward through the introduction of a rotating coordinate system. Secondly, non-linear airfoil properties, such as (dynamic) stall, need to be included. This will turn equation 6.5 into a more complicated set of coupled equations. To proceed we currently see three options:

1. Deal with the non-linear, coupled equations in the current framework;
2. Find and include a stochastic surrogate model of the non-linear on-blade effects;
3. Move from a Fourier expansion of Eqs. 6.3 and 6.4 to a polynomial chaos expansion (PCE) (Fluck and Crawford, 2017b). Since the PCE retains the time domain through the solution it will likely be easier to handle non-linear effects in the equations.

An investigation of these options and advancing to wind turbine blade optimization will be the subject of future work.

6.3 Results

In this section we compare lifting line results for blade loads from the stochastic model (equation 6.5) to deterministic results (equation 6.1). We consider a blade of $b = 60$ m span with constant chord $c = 4$ m, stationary 100 m above ground in $\bar{u}_\infty = 10$ m/s mean wind (IEC normal turbulence model, class A (IEC 61400-1, Ed. 3, 2005)). The blade and wake are resolved with $N_b = 6$ spanwise and $N_t = 5$ trailing elements. Loads are calculated at $\Delta t = 1$ s intervals. Wind is calculated from $N_f = 20$ frequencies logarithmically spaced at $f_m = \omega_m/(2\pi) \in [1/600, 0.5]$ Hz. For the deterministic case the usual process was followed: one wind speed realization was calculated first using Veers' model (Veers, 1988), then this wind was fed into equation 6.1 as inflow $u_{\infty,I}(t_n)$.

Figure 6.4 shows the wind speed realization used for the deterministic solution at the six blade elements together with the resulting deterministic bound circulation and one realization of the stochastic solution (bottom), as well as the steady state solution for $u = 10$ m/s with five snapshots of the stochastic solution (top). Note the

transient start-up period in the deterministic blade loads for $t < 5$ s (bottom part for Figure 6.4). This is due to the wake initialization with $\Gamma_{I,ij}(t_{n=0}) = 0$. As a result of the periodic nature of $\Phi_l(t_n)$ this transient phase does not exist in the stochastic solution.

The realization of the stochastic solution is generated from the same random seed as was used to generate the deterministic wind. Hence the stochastic solution perfectly reproduces that one particular deterministic solution (after the initial transient phase $t > 5$ s). Note, however, that the stochastic solution also contains all other possible realizations. Hence all other load time series can be calculated directly via equation 6.4 from only one stochastic solution.

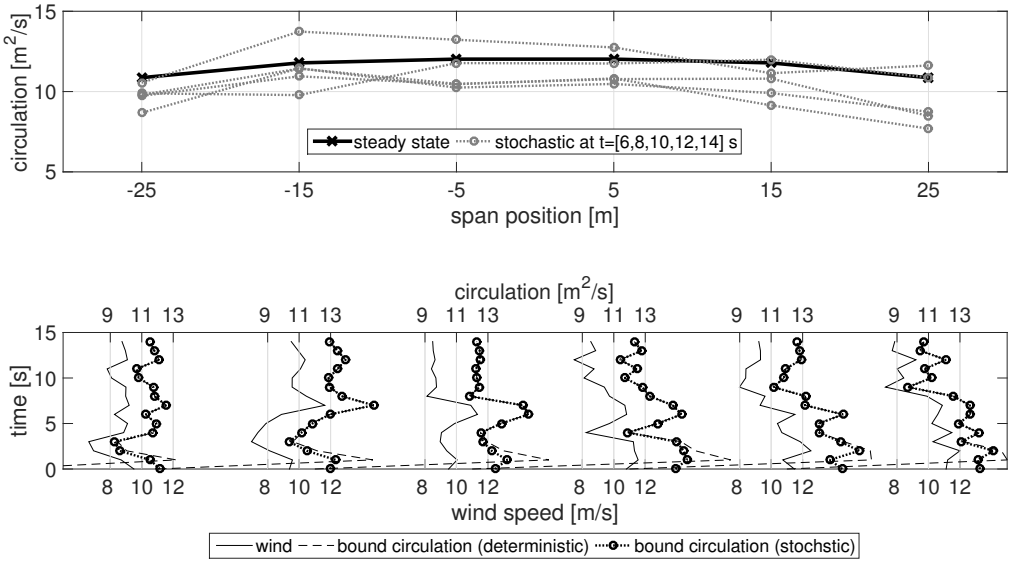

Figure 6.4: Wing load (circulation) and wind speed time series.

Next we will compare cross-correlation, covariance, and cross-spectrum of the dynamic blade loads from our stochastic method to the deterministic results. For the deterministic analysis, blade loads were calculated for 100 realizations of 600 s samples of turbulent wind synthesized with the commonly used wind simulator *TurbSim* (Kelley and Jonkman, 2007). For better comparison the spectrum $\boldsymbol{S}$ in equation 6.3 and 6.5 was replaced with the (slightly different) spectrum extracted from the *TurbSim* wind data set via Welch's periodogram method as implemented in Matlab's *cpsd* function (Welch, 1967). Similarly, phase increments $\Delta\boldsymbol{\Theta}_I$ were extracted from the Fourier

transform of the *TurbSim* data. To achieve smoother cross-correlation, covariance, and cross-spectrum curves we used 100 different sets of phase increments $\Delta\boldsymbol{\theta}_I$. As discussed in section 6.2.2, most of the stochasticity is contained in the uncorrelated random variables $\boldsymbol{\xi}$. The influence of random or deterministic $\Delta\boldsymbol{\theta}_I$ is hence a second order effect. Assessing the implications of only using one (or a few) set(s) of phase increments remains the subject of further study. As before, we use $N_b = 6$, $N_t = 5$, $N_f = 20$ with $f_m \in [1/600, 5]$ Hz, and $\Delta t = 1$ s.

6.3.1 Blade loads cross-correlation

Figure 6.5 shows the cross-correlation function of the circulation on the bound element pairs Γ_1-Γ_1, Γ_1-Γ_3, and Γ_1-Γ_6. It can be seen that the stochastic model results in a very similar cross-correlation as the computationally much more expensive deterministic model. The obvious difference – a much smoother curve in the deterministic cases – is due to the difference in the number of frequencies contained in the data. While the deterministic data (provided through *TurbSim*) is synthesized with well over ten thousand frequencies, the stochastic data is based on the reduced order model with only 20 frequencies.

6.3.2 Blade loads covariance

Table 6.1 shows the covariance of the blade loads for selected bound vortex elements (cf. figure 6.2) for the stochastic and deterministic results, and the error between the two results. This error is small, especially considering that (assuming normal distributed blade loads) the 90% $\mathcal{X}^2$ confidence bounds of the deterministic variance $\mathrm{Var}[\Gamma_1, \Gamma_1]$ are [-0.94, 0.96]%. Thus it can be seen that the stochastic and deterministic results are in very good agreement.

Table 6.1: Covariance of blade loads.

	$\mathrm{Var}[\Gamma_1, \Gamma_1]$	$\mathrm{Var}[\Gamma_1, \Gamma_2]$	$\mathrm{Var}[\Gamma_1, \Gamma_3]$	$\mathrm{Var}[\Gamma_1, \Gamma_5]$	$\mathrm{Var}[\Gamma_4, \Gamma_5]$
stochastic [$\mathrm{m}^2/\mathrm{s}^4$]	4.06	3.76	2.60	4.17	4.82
deterministic [$\mathrm{m}^2/\mathrm{s}^4$]	4.20	3.77	2.56	4.20	4.91
error [%]	3.27	0.20	-1.37	0.63	1.81

6.3.3 Blade loads cross-spectrum

Figure 6.6 shows the cross power spectral density functions of the circulation for the same bound element pairs as before. Both the deterministic and stochastic results were again obtained from Welch's spectral estimation from 100 realizations of the resulting blade loads, binned to the frequencies ω_m as used in the reduced model. Again, the stochastic results are very similar to the computationally much more expensive deterministic model.

Note the two zero-power frequencies ω_2 and ω_3 result from the different frequency spacing in the *TurbSim* data (linear spacing) versus the reduced model (logarithmic spacing). The *TurbSim* data does not contain frequencies between ω_1 and ω_4, and hence there is zero power in the spectrum there. Although these frequencies exist in the stochastic data, they do not contain any power because we use the *TurbSim* spectrum $\boldsymbol{S}$ in equation 6.5.

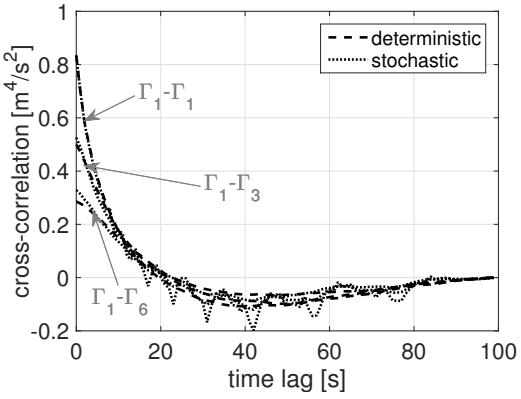

Figure 6.5: Cross-correlation function for circulation of selected bound element pairs.

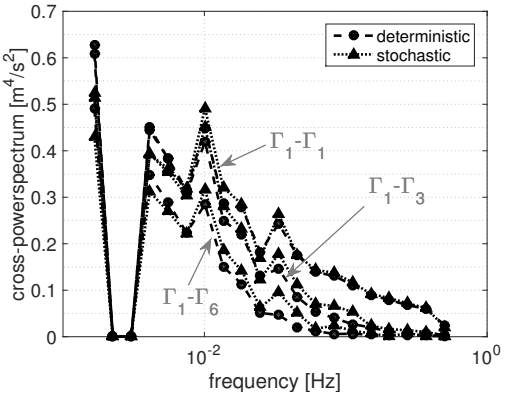

Figure 6.6: Discrete cross-spectrum for circulation of selected bound element pairs.

6.3.4 Numerical Cost

At this point we use a crude Matlab implementation of both the deterministic and stochastic models. This implementation was designed for experimenting with the new model, rather than for performance. Hence, only a very rough estimate of the computational cost can be given. However, the superiority of the stochastic model becomes apparent nonetheless. On an Intel i5 quad core processor solving 100 realizations of 600 s of the deterministic model takes roughly ten minutes (upper path in figure 6.1). On the other hand, calculating one stochastic solution with one set of deterministic phase increments takes less than one second, and realizing 100 samples at the end (lower path in figure 6.1) is done in about three seconds, yielding 100 realizations from the stochastic model in under five seconds. This is less than 1% of the time originally used for the deterministic solution.

As shown in the preceding subsections, the stochastic solution reproduces the statistics of the (correlated) blade loads well. Through postponing the generation of various different realizations from before calculating a solution (deterministic approach, upper path in Figure 6.1) to generating realizations of a stochastic solution at the end (stochastic approach, lower path in Figure 6.1) long term loads can be estimated very quickly and thus become accessible to be included into an optimization routine.

Besides generating individual solution realizations, a stochastic expression for the blade loads also holds the possibility of directly extracting load statistics (mean, variance, possibly peak return periods). Details of such a stochastic load analysis from a stochastic load solution will presented in a future publication.

6.4 Conclusions

We extended a stochastic model previously introduced for a single element blade to model correlated aerodynamic loads on a stationary wind turbine blade in turbulent atmospheric wind. The blade is now resolved with several spanwise and wake lifting line elements. A reduced order model for the (stochastic) wind inflow fields, based on phase angle increments between the wind speed at a base point and any other data point in the wind field is employed to limit the number of random variables necessary.

Through a comparison to deterministic results (based on several wind field realizations generated from *TurbSim*) it was shown that the stochastic model conserves the stochastic properties of the dynamic blade loads, including coupling of loads on different stations along the blade (cross-correlation, covariance, cross-spectrum). For a simple Lagrangian vortex model test case (lifting line model), the stochastic formulation yielded results for 100 blade load samples in less than 1% of the computation time needed by the deterministic model. This indicates that long term (extreme and fatigue) blade loads, commonly extracted from the tails of a load probability distribution, can now be assessed quickly.

Future work will take the currently stationary blade into a rotating reference frame to model a wind turbine rotor and subsequently include the stochastic formulation into a multidisciplinary design optimization framework. While the Lagrangian vortex model allows extension of the design space to unconventional blade geometries, the stochastic aerodynamic model limits the computational effort required to extract reliable blade load statistics. The new stochastic model also makes long term loads directly accessible to optimization. Hence the combination of a Lagrangian vortex model with a stochastic aerodynamic model might open up new avenues to pursue improved and novel wind turbine blade designs.

Chapter 7

A Fast Stochastic Solution Method for the Blade Element Momentum Equations for Long-Term Load Assessment

This chapter presents the latest version of a paper submitted March 1, 2017 for publication in the journal Wind Energy:
Fluck, Manuel and Crawford, Curran: "*A fast stochastic solution method for the Blade Element Momentum equations for long-term load assessment*", Wind Energy, **submitted**

In this paper we extend the stochastic models derived previously to spinning wind turbine rotor and rotationally sampled wind. Moreover, we extend our work to non-linear equations, and show that one stochastic solution can produce similar results for turbine blade loads as multiple solutions from the deterministic model conventionally used.

See appendix C.4.2 for further information regarding the MATLAB code used to generate results for this section.

Abstract

Unsteady power output and long term loads (extreme and fatigue) drive wind turbine design. However, these loads are difficult to include in optimization loops, and so are only typically assessed in a post-optimization load analysis or via reduced order methods, yielding sub-optimal results. The basis for this difficulty are the deterministic approaches to assess long term loads. They require the analysis of many unsteady load cases, generated from many different random seeds, to model the statistics of life time loads, a computationally expensive Monte Carlo procedure. In this paper, we present an alternative: a stochastic solution for the unsteady aerodynamic loads based on a projection of the unsteady Blade Element Momentum (BEM) equations onto a stochastic space spanned by chaos exponentials. This approach is similar to the increasingly popular polynomial chaos expansion (PCE), but with two major differences. First, the BEM equations constitute a random process, varying in time, while previous PCE methods were concerned with random parameters (i.e. random but constant in time or initial values). Second, a new, more efficient basis (the exponential chaos) is used. This new stochastic method enables us to obtain unsteady long term loads much faster, enabling unsteady loads to become accessible inside wind turbine optimization loops. In this paper we derive the stochastic BEM solution and present the most relevant results showing the accuracy of the new method.

Nomenclature

Latin Letters:

a	power law exponent
c	chord length
c_d	drag coefficient
c_l	lift coefficient
c_x	thrust coefficient
h_{hub}	hub height
K	number of terms in airfoil series
N	number of stochastic samples
N_F	number of frequencies
N_P	number of wind speed sample points
N_R	number of random variables
N_S	number of random basis functions
r	rotor radius
S	wind speed power spectrum
$\hat{S}$	solution series coefficient
T	thrust force
$\hat{T}$	thrust series coefficient
t_n	(discrete) time
$\tilde{u}$	turbulent fluctuations
u_{app}	apparent wind speed
u_0	mean wind speed (at hub height)
u_{ax}	axial induced velocity
u_{dc}	mean wind speed
u_{rot}	rotationally sampled inflow wind speed
u_{tg}	tangential induced velocity

Greek Letters:

α	angle of attack
β	element twist
θ	phase
$\Delta\theta$	phase increment
Ξ	stochastic space
ξ	random number
ϕ	local inflow angle
τ	local pitch
τ_0	blade pitch
Ψ	chaos basis
Ω	rotor angular frequency
ω	angular frequency

Indices:

k	index for points
l	index for blade elements
m	index for frequencies
n	index for samples in time

7.1 Introduction

Long term loads (i.e. life time extreme and fatigue loads) are often critical drivers for the structural design of wind turbines. However, the analysis of long term loads is typically not included into the turbine design optimization loop. Instead, compliance of a candidate design with long term load requirements is ensured only after the

design optimization is completed. This sequential procedure can obviously lead to sub-optimal results. However, today this is usually the only possibility, because reliably analyzing long term loads is computationally expensive – too expensive to be included into the optimization loop.

These challenges arise from the procedure through which long term loads are assessed. Today, wind turbine design and analysis is usually carried out in a deterministic framework, or at best as a Monte Carlo like set of several subsequent deterministic solutions (upper path in Fig. 7.1). Adequately capturing the long term load statistics in such a deterministic framework requires the analysis of many samples. The design standard IEC 61400-1, Ed. 3 (2005) is indicative of this challenge: it bases the turbine load analysis on multiple deterministic 600 s simulations, carried out at many different mean wind speeds, for roughly 20 different load cases, every one repeated several times with different realizations of the turbulent inflow, each generated from a different random seed. This large number of analyses and the associated computational costs obviously present a challenge to any automated optimization, where many different candidate designs have to be evaluated.

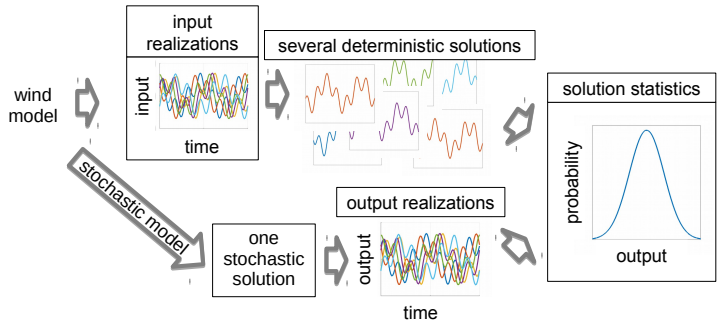

Figure 7.1: Alternate solution methods. Top: conventional deterministic route; Bottom: the new stochastic alternative.

Even if this large number of deterministic simulations was tractable, the challenges with the deterministic framework continue. It is known that extrapolation from a limited data set to extreme loads is a delicate exercise and results can vary greatly (Moriarty, 2008; Burton et al., 2011). It was shown that basing a wind turbine analysis on six ten-minute wind speed simulations, generated from six different random seeds,

results in a difference of up to 34% in the ultimate load results for the most extreme 1% of seed combinations (Zwick and Muskulus, 2015). Tibaldi et al. (2014) present a study which indicates that turbine loads extracted even from 20 different ten-minute wind fields, generated from 20 different random seeds, vary greatly. This shows that in a deterministic framework, load variations from different random seeds can dominate effects from design parameter changes. Obviously this constitutes a fundamental problem, particularly with gradient-based optimization where obtaining reliable design variable gradients is vital.

The goal of this paper is to avoid these problems and present a means to quickly analyze long term loads which can be used within a future optimization routine. To do this we propose to look at the governing equations from a different perspective. The current method obtains a deterministic solution from a deterministic analysis using deterministic equations. The deterministic equations are individual samples (obtained through the use of specific random seeds) from an a priori stochastic input (e.g. wind or waves). This approach is convenient, because it allows us to remain in the well known deterministic world; when individual samples are treated we can ignore the difficulties related to the stochastic dimension of the problem at hand. However, this comfort comes with the price outlined above (Fig. 7.1, upper path): If we want to regain the stochastic domain of our solution (i.e. load statistics) we need to analyze a large number of deterministic samples.

If we step away from this deterministic thinking and look at the process in the context of its full stochastic scope, we see that instead of embracing the stochastic dimensions available we reduced the (initially stochastic) problem to the analysis of individual sample paths or realizations[14] and then struggle at the end to regain the stochastic dimensions through the analysis of multiple deterministic solutions. We propose a stochastic solution, the lower path in Fig. 7.1. This stochastic approach will embrace the stochasticity of turbulent atmospheric wind and thus take advantage of the knowledge of the stochastic domain all the way through the system analysis towards a stochastic solution.

[14] A sample path (also called a realization) is the evolution of the system through time for one specific random seed.

To achieve this we, advance the basic ideas brought forward earlier (Fluck and Crawford, 2017b), and no longer employ a deterministic analysis of multiple input realizations (the wind), but instead treat the aerodynamic equations in their full stochastic context. This will allow us to eventually assess long term loads from one single stochastic solution. Thus, long term loads can be assessed more quickly.

In the following, we present a preliminary test case to show the feasibility and benefits of the new stochastic analysis method based on the aerodynamic equations form Blade Element Momentum (BEM) theory (Burton et al., 2011; Bladed, 2012; Hansen, 2008). This is not an example of a full wind turbine optimization, but merely a proof of concept for that eventual application. Thus, at several instances we chose an easier solution over a computationally more efficient or more elegant alternative. Extending the authors previous work (Fluck and Crawford, 2017b, 2016c), where a stationary wing with linear time dependent aerodynamic equations was treated, we here show the feasibility of the stochastic method with non-linear time dependent aerodynamic equations for a wind turbine rotor. An expansion to a more involved aerodynamic model (e.g. a Lagrangian vortex model) and the incorporation into an optimization routine is left for future work.

7.2 Method

To arrive at a stochastic solution for the unsteady BEM equations we adopt a stochastic spectral approach, first employed by Ghanem and Spanos (1991) for finite element analysis. This method separates the random dimensions of the problem from the deterministic ones, by expressing the solution S (later the thrust or torque contribution of a particular blade element) as a stochastic series:

$$S(t, \boldsymbol{\xi}) = \sum \hat{S}_s(t) \Psi_s(\boldsymbol{\xi}) \tag{7.1}$$

Eq. 7.1 can be interpreted as expressing the solution S by a linear combination of deterministic coordinates $\hat{S}_s$ in a stochastic space Ξ spanned by a set of adequately selected stochastic basis functions $\Psi_s(\boldsymbol{\xi})$ of the random vector $\boldsymbol{\xi} = [\xi_m]$, Fig. 7.2 (with Ξ, Ψ, and $\boldsymbol{\xi}$ to be specified later). Thus the problem of finding an unknown stochastic solution S is transformed into finding the unknown coordinates $\hat{S}_s$. Note that while the usual applications of the stochastic spectral method have been concerned with

a random variable constant in time, the aerodynamic equations considered here are random functions of time (i.e. random processes). Hence the coordinates $\hat{S}_i$ are not constant anymore, but a function of time, too. This allows the stochastic solution to capture short term time history and hysteresis effects as well as the long term stochastic behavior of loads. To solve for the coordinates $\hat{S}_s$ a stochastic Galerkin projection (presented in (Fluck and Crawford, 2017b)) is employed. Since each basis function $\Psi_i(\boldsymbol{\xi})$ is a multivariate function of N_R random variables $[\xi_1, \ldots, \xi_{N_R}] = \boldsymbol{\xi}$, this projection will collapse the different deterministic solutions from all different random seeds $\boldsymbol{\xi}$ into a single set of time varying coordinates $\hat{T}_i(t_n)$.

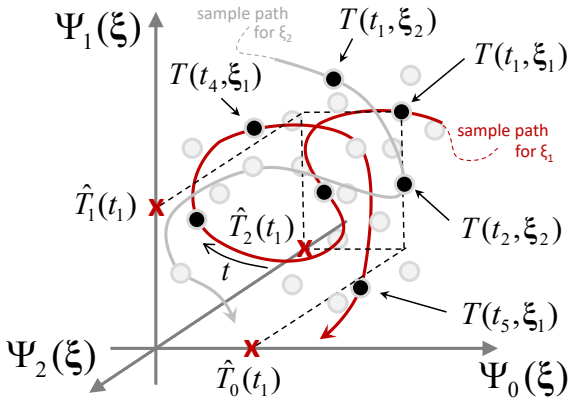

Figure 7.2: Projection of the time dependent, stochastic solution onto a stochastic space spanned by three basis functionals $\Psi_s(\boldsymbol{\xi})$.

Let $\langle \square, \Psi_s(\boldsymbol{\xi}) \rangle$ denote some stochastic projection onto Ψ_s (details explained later). If $S_{\boldsymbol{\xi}_i}(t) = \mathcal{B}(\boldsymbol{x}, u_{\boldsymbol{\xi}_i}(t))$ is the solution to the unsteady BEM equations for a particular turbine design described by the state vector [15] $\boldsymbol{x}$ and one specific wind field sample $u_{\boldsymbol{\xi}_i}(t)$ generated from one specific random seed $\boldsymbol{\xi}_i$, then $\hat{S}_s$ could be approximated deterministically by sampling the unsteady BEM equations for a sufficiently large set of random seeds $\boldsymbol{\xi}_i$ and numerically evaluating the stochastic projection $\langle \mathcal{B}(\boldsymbol{x}, u_{\boldsymbol{\xi}}(t)), \Psi_s(\boldsymbol{\xi}) \rangle$ from multiple samples. However, as will become apparent later, the stochastic projection is computationally expensive. Following this route would mean that for each change in turbine design parameters $\boldsymbol{x}$, the projection would have

[15] In general $\boldsymbol{x}$ will contain all turbine design parameters, i.e. geometry and control parameters. For this study, however, we will assume constant rotational speed and thus neglect any controller input.

to be evaluated anew. For application to optimization, this is obviously problematic.

The goal of this paper will instead be to reformulate the unsteady BEM equations to split them into a turbine design dependent part $\mathcal{B}_T(\boldsymbol{x})$, and a time-random part $\mathcal{B}_R(\boldsymbol{\xi}, t)$:

$$\mathcal{B}\left(\boldsymbol{x}, u_{\boldsymbol{\xi}}(t)\right) = \mathcal{B}_T(\boldsymbol{x}) \cdot \mathcal{B}_R(\boldsymbol{\xi}, t) \tag{7.2}$$

Following this route will allow the separation of $\mathcal{B}_T$, which will be independent of $\boldsymbol{\xi}$, from the projection:

$$\langle \mathcal{B}(\boldsymbol{x}, u_{\boldsymbol{\xi}}(t)), \Psi_s(\boldsymbol{\xi}) \rangle = \mathcal{B}_T(\boldsymbol{x}) \cdot \langle \mathcal{B}_R(\boldsymbol{\xi}, t), \Psi_s(\boldsymbol{\xi}) \rangle \tag{7.3}$$

Thus, during a turbine optimization run, the computationally expensive projection $\langle \mathcal{B}_R, \Psi_s \rangle$ will be carried out only once in a pre-processing step, while the varying turbine parameters can be included quickly through multiplication by $\mathcal{B}_T$.

For this strategy to work an enhanced closed-form analytic expression of the BEM equations is required with:

i) a stochastic expression of the inflow wind speed as function of the random seed $\boldsymbol{\xi}$, and

ii) an analytic expression of the lift and drag coefficients, or thrust and torque coefficients c_x and c_t respectively, for the blade airfoils.

In the following, the well-known BEM equations will be repeated briefly. Subsequently the required analytic expressions for turbulent atmospheric wind (Section 7.2.2) and airfoil data (Section 7.2.3) will be derived to arrive at the fundamental equations used for the stochastic projection (Section 7.2.4). Subsequently a suitable stochastic basis will be defined and the projection outlined above will be presented in detail (Section 7.2.6).

To avoid excessive indexing only one rotor blade will be considered for the derivation. The extension to N_B rotor blades is trivial; Moreover, only the equations for thrust will be derived. The procedure for calculating torque will be identical with the torque coefficient instead of the thrust coefficient.

7.2.1 The conventional unsteady BEM thrust equation

From BEM theory (Burton et al., 2011; Bladed, 2012; Hansen, 2008) the thrust at any blade element indexed by its radial position r is:

$$T_r(t) = \frac{\rho}{2}\, u_{app}^2(t) c_x(t)\; c\Delta r \tag{7.4}$$

with $c_x(t) = c_x(\phi(t))$ the blade element instantaneous thrust coefficient as a function of the local (time varying) inflow angle $\phi(t)$, c the element's chord, and Δr its length (cf. Figs. 7.3–7.4). The rotationally sampled apparent inflow is:

$$u_{app}(t) = \sqrt{(u_{rot}(t) - u_{ax})^2 + (\Omega r + u_{tg})^2} \tag{7.5}$$

with axial and tangential induced velocities, u_{ax} and u_{tg} respectively (Fig. 7.3), and the axial component of the rotationally sampled inflow wind speed u_{rot} (without the tangential component of the relative blade motion). Note that, without explicit labeling, u_{app}, u_{rot}, c_x, c, and Δr are of course functions of the blade element location r on the rotor disc. Moreover, the inflow wind field $V = [u_x, 0, 0]$ is assumed to be purely one-dimensional and aligned with the turbine rotor axis. To not unnecessarily complicate the equations, this study uses a frozen wake model (Bladed, 2012), by assuming that the induced velocities u_{ax} and u_{tg} are constant in time and equal to the induced velocities from the steady BEM for constant, homogeneous hub height mean wind speed u_0. It is important to note that the induced velocities u_{ax} and u_{tg} are frozen in time, not the induction factors themselves, and that u_{ax} and u_{tg} are still obtained from a steady state BEM solution for each specific the rotor geometry. For a future optimization u_{ax} and u_{tg} will be updated with each rotor design update. Moreover, freezing the wake does not mean induction terms are neglected. The induced velocities u_{ax} and u_{tg} will still be contained in the equations. Only the (temporal) variations $\tilde{u}_{ax}$ and $\tilde{u}_{tg}$ are neglected. Considering that wake advection causes a time lag between rotor load changes and wake strength changes, and that the rotational sampling of the turbulent wind field by the spinning rotor blade, as well as dynamic on blade effects cause considerable averaging of the dynamic induction effects, assuming a frozen wake is a fair choice for this preliminary study. Since the stochastic solution is still a time stepping solution, a more advanced wake model (e.g. instantaneous induction change (Pitt and Peters, 1981; Peters and He, 1991), inertially lagged wake) can later easily be incorporated into the to the stochastic equations in a

similar fashion as is already well established for the conventional deterministic methods.

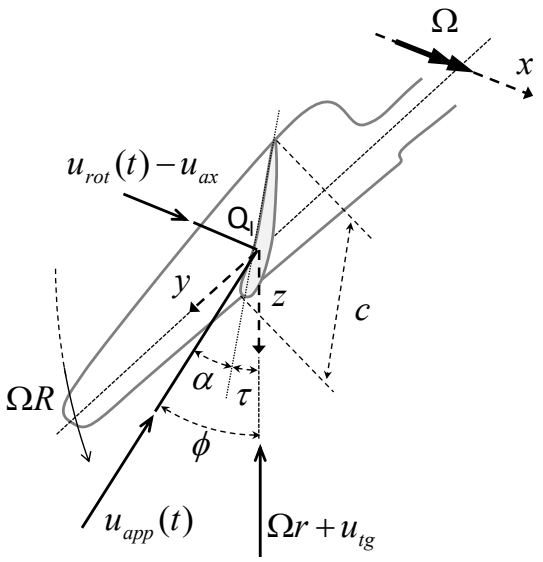

Figure 7.3: Definition of velocities and inflow angles at a blade section with local (rotating) coordinate system.

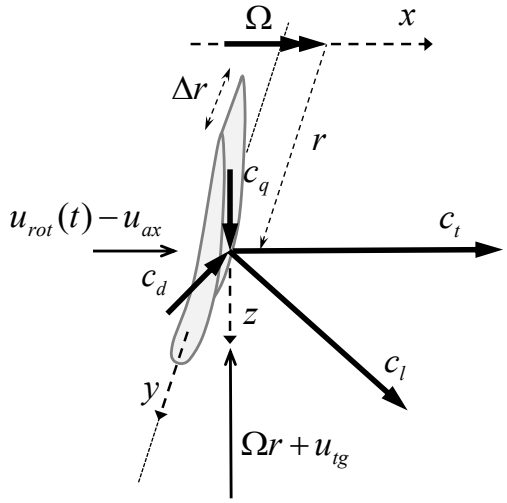

Figure 7.4: Definition of blade element geometry and force coefficients with local (rotating) coordinate system.

7.2.2 Stochastic wind, rotationally sampled

The wind inflow data, used for a BEM analysis, is usually synthesized from a numeric wind model and the stochastic wind simulator TurbSim (described by Kelley and Jonkman (2007)) is the standard tool for this task in industry. Based on Veers' spectral model (Veers, 1988), TurbSim generates a data set of wind from a random seed. Although it is well known that Veers' model does not capture all physical details of 'real' atmospheric wind (e.g. Mücke et al. (2011); Morales et al. (2012); Lavely et al. (2012); Park et al. (2015)), it is an appropriate engineering model (Nielsen et al., 2007) required by the international design standard IEC 61400-1, Ed. 3 (2005). For a grid of N_P wind speed data points (distributed over the rotor plane) resolved with N_F frequencies from the wind speed spectrum, Veers' model (and TurbSim) uses $N_R = N_F \cdot N_P$ random variables to set the wind field's phase angles. In practical cases this quickly amounts to somewhere on the order of 10^5 random variables. Since realizations of large sets of random variables can be generated very quickly, this

is not a problem for deterministic load analyses. However, the computational cost of stochastic tools increases dramatically with the number of random variables, a phenomenon commonly known as the 'curse of dimensionality' (Majda and Branicki, 2012). To keep the number of random variables manageable a reduced order wind model is used (Fluck and Crawford, 2017a):

$$u_k(t, \boldsymbol{\xi}) = \sum_{m=-N_F}^{N_F} \sqrt{S(\omega_m)}\, e^{i(\omega_m t + 2\pi\xi_m + \Delta\theta_{mk})} \tag{7.6}$$

where S is the (symmetric) wind speed power spectrum (e.g. a Kaimal spectrum, cf. (Burton et al., 2011) Eq. (2.24)), ω_m are selected spectral frequencies, $\boldsymbol{\xi} = [\xi_m]$ is a random vector, and $\Delta\boldsymbol{\theta} = [\Delta\theta_{mk}]$ is a matrix of (deterministic, known, and usually constant) phase increments implicitly containing the spatial structure (i.e. coherence) of the wind field. This brings the count of necessary random numbers ξ_m down to $N_R = N_F$, independently of how many data points are contained in the wind data grid.

Through Eq. 7.6 the inflow wind speed u_k is given in an earth-fixed reference frame. For Eq. 7.4, however, the rotationally sampled inflow $u_{rot,l}$ at a point Q_l on the rotor blade a distance r_l from the hub, is required. To obtain $u_{rot,l}$ we assume constant[16] rotor speed Ω and arrange the (earth-fixed) points P_{k_n} in a azimuthal pattern such that $P_{k_n} = [p_{kx_n}, p_{ky_n}] = r_l[\sin(\Omega t_n), \cos(\Omega t_n)]$, Fig. 7.6. Thus Q_l passes through P_{k_n} at the time $t_n = n \cdot \Delta t$. Hence it is possible to group the phase increments $\Delta\theta$ such that $\Delta\theta_{ml}(t_n) = \Delta\theta_{mk_n}$ with $k_n = k(t_n)$. For clarity we define the deterministic wind component as:

$$\hat{u}_{ml}(t_n) := \sqrt{S(\omega_m)}\, e^{i(\omega_m t_n + \Delta\theta_{mk_n})} \tag{7.7}$$

for each blade element Q_l.

Next consider wind shear. Neglecting any details of the atmospheric boundary layer we must assume a power law description (IEC 61400-1, Ed. 3, 2005). Hence, the mean wind speed at each data point P_k is $u_{dc,k} = u_0 \left(\frac{p_{ky}}{h_{hub}}\right)^a$ for a mean wind speed u_0 at hub height h_{hub}, with the power law exponent a set according to e.g. Jonkman and Kilcher (2012). For the rotationally sampled mean wind speed including wind

[16] This assumption for now simplifies the equations, and moreover allows to avoid dealing with the setup of a controller algorithm. Since the final solution (Eqs. 7.21 and 7.22) is a time series solution, eventually introducing a controller routine and modeling variable rotor speed will not be a major challenge.

shear at the blade point Q_l this yields (with zero shaft tile angle, and no yaw):

$$u_{dc,l} = u_0 \left(1 + \frac{r_l}{h_{hub}} \cos(\Omega t_n)\right)^a \tag{7.8}$$

Discarding the DC component from the spectrum $S(\omega_0) = 0$ ($\hat{u}_{0l}(t_n) = 0$) and replacing it with the rotationally sampled mean wind shear, Eq. 7.7 yields the rotationally sampled turbulent wind speed at any blade point Q_l:

$$u_{rot,l}(t, \boldsymbol{\xi}) = u_{dc,l} + \sum_{m=-N_F}^{N_F} \hat{u}_{ml}(t_n)\, e^{2i\pi\xi_m} \tag{7.9}$$

For clarity we drop the index l in the sequel and look at one blade element only.

7.2.3 Airfoil data

With lift and drag coefficients, c_l and c_d, obtained from experiment or simulation the thrust coefficient c_x in Eq. 7.4 is computed as (Fig. 7.4):

$$c_x(t) = c_l(\alpha, \phi, t)\cos(\phi(t)) + c_d(\alpha, \phi, t)\sin(\phi(t)) \tag{7.10}$$

For any given inflow angle ϕ and known local pitch angle τ at the blade element, Eq. 7.10 is usually solved via interpolation from tabulated airfoil data for c_l and c_d. However, in order to separate turbine design dependent parts of the BEM equations from the stochastic parts (cf. Eq. 7.3) we seek a closed-form function $c_x = c_x(\phi(t))$. Note that the following steps will not change the BEM equations in principle, and that ϕ will still include the induced velocities (Fig. 7.4), but that we merely map the element force look-up table from $c_l(\alpha)$ and $c_d(\alpha)$ to $c_x(\phi)$. We include the local blade element pitch angle $\tau(r) = \beta(r) + \tau_0$ in a reformatted airfoil data set and use $\alpha = \phi - \tau$. Then we approximate the thrust coefficient as a complex Fourier series of the discrete base mode numbers m_k: $c_x = \sum_k Y^0_{\tau,k}\, e^{i\phi m_k}$, to obtain the desired function of ϕ. For convenience later on we note:

$$\phi(t) = \tan^{-1}\left(\frac{u_{rot}(t) - u_{ax}}{\Omega r + u_{tg}}\right) \tag{7.11}$$

and map the airfoil data such that c_x is obtained as a function of $\tan\phi$ (instead of ϕ itself) from a sufficiently large number of modes K (Fig. 7.5):

$$c_x\left(\tan(\phi(t))\right) = \sum_{k=0}^{K-1} Y_{\tau,k}\, e^{i(\tan(\phi(t))+\frac{\pi}{2})m_k} \qquad \text{for} \quad \tan\phi \in \left[-\frac{\pi}{2}, \frac{\pi}{2}\right] \tag{7.12}$$

For Eq. 7.12 $Y_{\tau,k}$ is easily obtained from a Fast Fourier Transform of any airfoil data set $c_l(\alpha)$, $c_d(\alpha)$ and Eq. 7.10, mapped for a specific pitch angle τ from α to $\tan(\phi)$.

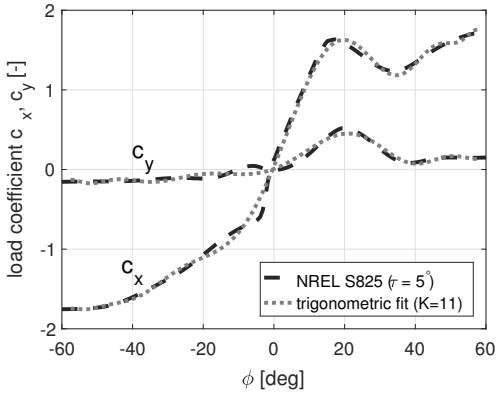

Figure 7.5: Thrust coefficient original data, and a trigonometric fit (Eq. 7.12).

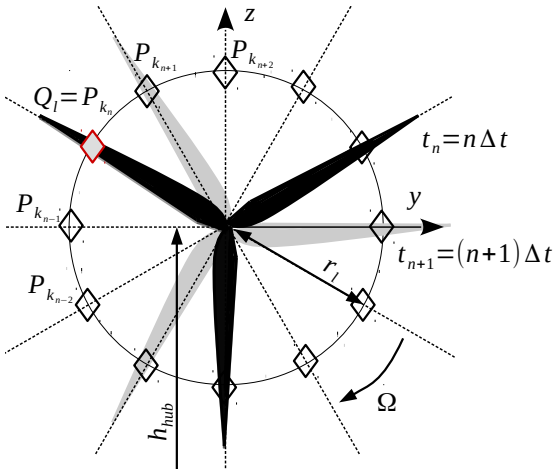

Figure 7.6: Wind speed data points arranged around rotor in an azimuthal pattern (shown only for one radius $r = r_l$, looking downwind).

Combining Eqs. 7.8, 7.9, 7.11, 7.12 and rearranging yields:

$$c_x(t_n) = \sum_{k=0}^{K} Y_{\tau,k}\, e^{L_k \tilde{u}(t_n)} \cdot E_k(t_n) \tag{7.13}$$

where

$$E_k(t_n) := \exp\left[i\left(\frac{u_{dc}(t_n) - u_{ax}}{\Omega r + u_{tg}} + \frac{\pi}{2}\right) m_k\right] \tag{7.14}$$

$$L_k := i\frac{m_k}{\Omega r + u_{tg}} \tag{7.15}$$

and the (mean-free, rotationally sampled) turbulent fluctuations:

$$\tilde{u}(t_n, \boldsymbol{\xi}) := u_{rot}(t) - u_{dc} = \sum_{m=-N_F}^{N_F} \hat{u}_m(t_n)\, e^{2i\pi\xi_m} \tag{7.16}$$

7.2.4 The combined BEM thrust equation

To arrive at the desired analytic expression of the BEM equations, Eqs. 7.5, 7.9, and 7.13 can now be combined into Eq. 7.4:

$$T_r(t) = \frac{\rho}{2} c \Delta r \ \left((\tilde{u}(t_n, \boldsymbol{\xi}) + u_{dc} - u_{ax})^2 + (\Omega r + u_{tg})^2 \right) \ \sum_{k=0}^{K} Y_{\tau,k}\, e^{L_k \tilde{u}(t_n, \boldsymbol{\xi})} \cdot E_k(t_n) \tag{7.17}$$

As discussed, it is important to separate turbine dependent parts from the stochastic parts. Thus, we write Eq. 7.17:

$$\begin{aligned} T_r(t_n) = \overbrace{\frac{\rho}{2} c \Delta r}^{\text{turbine, } \mathcal{B}_T} \overbrace{\Bigg(A \cdot \sum_{k=0}^{K} Y_{\tau,k} E_k(t_n) \ \ F_k(t_n, \boldsymbol{\xi})}^{\text{random, } \mathcal{B}_R} \ + \\ B \cdot \sum_{k=0}^{K} Y_{\tau,k} E_k(t_n) \ \ F_k(t_n, \boldsymbol{\xi}) \tilde{u}(t_n, \boldsymbol{\xi}) \ + \\ \sum_{k=0}^{K} Y_{\tau,k} E_k(t_n) \ \ F_k(t_n, \boldsymbol{\xi}) \tilde{u}^2(t_n, \boldsymbol{\xi}) \Bigg) \end{aligned} \tag{7.18}$$

with $A := (u_{dc} - u_{ax})^2 + (\Omega r + u_{tg})^2$, $B := 2(u_{dc} - u_{ax})$, and $F_k(t_n, \boldsymbol{\xi}) := \exp\left[L_k \tilde{u}(t_n, \boldsymbol{\xi})\right]$. Note that $T_r(t_n)$ and thus $T_r(t)$ are still time domain solutions. Hence time domain effects such as load auto-correlation and for future work hysteresis effects (e.g. dynamic stall, wake advection) can easily be included.

In Eq. 7.18 only the latter part of each summand is dependent on the random vector $\boldsymbol{\xi}$, while most of the turbine parameters are contained in the leading part. The only exception is L_k, which theoretically is a function of the induced velocity u_{tg}, and thus of the turbine design. Practically, however, L_k can easily be considered constant and independent of the turbine design, as $u_{tg} << \Omega r$.

Eq. 7.18 already represents a stochastic solution, i.e. a solution on the lower path of Fig. 7.1. However, repeatedly solving this equation for multiple candidate designs is still fairly costly, even for an aerodynamic model as simple as BEM. A more complicated aerodynamic model (e.g. a Lagrangian vortex model as would be used to analyze advanced blade geometries (Fluck and Crawford, 2014)) might not allow to express blade loads explicitly as a function of the random variable. Hence, the next section presents the steps necessary to project Eq.7.18 onto the stochastic space. Thus we arrive at a stochastic series expression of for blade loads and at a solution process which can similarly be used for BEM equations as well as for more complicated equations.

7.2.5 The stochastic basis

To arrive at the chaos series form Eq. 7.1 we follow the method presented by Fluck and Crawford (2017b) and apply a stochastic projection. Due to the nature of the BEM equations we use the strategy labeled 'Expansion of Random Phase Angles'. For this expansion, a polynomial chaos basis is usually used (Le Maître and Knio, 2010). However, for the problem at hand complex exponential functions turn out to be a better choice. Firstly, these allow an approximation of the stochastic domain with only a very small subset of the stochastic basis functions, cf. Fig. 7.7. Secondly choosing complex exponential functions will result in a stochastic projection operation similar to a multidimensional Fourier transform, enabling the use of efficient Fast Fourier Transform algorithms.

Similar to polynomial chaos (PC), the new basis functions will be functions of the random vector $\boldsymbol{\xi}$. Hence, they will be called chaos exponentials, or exponential chaos (EC) functions. Since Eq. 7.18 is a function of the N_R-dimensional random vector $\boldsymbol{\xi} = [\xi_m]$, $m = 1 \dots N_R$, multivariate complex chaos exponentials $\Psi(\boldsymbol{\xi})$ are required. Let $\lambda_m \in \{0, 1, \dots p\}$ and $\boldsymbol{\Lambda}_s = \{\lambda_m\}_s$, $s = 1 \dots N_S$, be one of N_S rows in the integer lattice $\boldsymbol{\Lambda} \in \mathbb{Z}^{N_R}$ of all points in $[0, \dots, p]^{N_R}$, then:

$$\Psi_s(\boldsymbol{\xi}) = \prod_{\lambda_m \in \boldsymbol{\Lambda}_s} e^{2i\pi\ \lambda_m \xi_m} = e^{2i\pi\ \boldsymbol{\Lambda}_s \boldsymbol{\xi}} \tag{7.19}$$

Consider a discrete, N_R-dimensional stochastic (chaos) space $\Xi = [0, 1]^{N_R}$ of N_R random variables ξ_m, sampled in each dimension $m = 1 \dots N_R$ at N equidistant sample

points $\bar{\boldsymbol{\xi}}_m = [0, 1/N, \ldots, (N-1)/N]$. For a discrete sample lattice $\bar{\boldsymbol{X}} = [\bar{\boldsymbol{\xi}}_m]$ over all N_R dimensions the chaos exponentials Ψ_s constitute an orthonormal basis of Ξ with the (normalized) inner product:

$$\langle f, g \rangle = \frac{1}{N^{N_R}} \sum_{\bar{\boldsymbol{X}}} f(\bar{\boldsymbol{\xi}}) g^*(\bar{\boldsymbol{\xi}}) \tag{7.20}$$

where $\sum_{\bar{\boldsymbol{X}}}$ denotes the N_R-dimensional sum over all points in the sample tensor $\bar{\boldsymbol{X}}$, and g^* the conjugate complex of g. Eq. 7.20 is normalized with $1/N^{N_R}$, such that $\langle \Psi_s(\boldsymbol{\xi}), \Psi_t(\boldsymbol{\xi}) \rangle = \delta_{s,t}$ ($\delta_{s,t}$ denoting the Kronecker delta). Hence $\langle \square, \Psi_s(\boldsymbol{\xi}) \rangle$ constitutes an orthonormal projection of $\square$ onto the stochastic basis function Ψ_s. Note that in general, for an arbitrary function, $N \to \infty$ is necessary. However, as will be shown later, in our case $N \ll \infty$ is sufficient.

7.2.6 Projection and stochastic solution

In order to conduct the stochastic Galerkin projection, the thrust solution $T_r(t_n)$ is now expanded in terms of the random variable (as introduced by Fluck and Crawford (2017b)). Instead of a polynomial chaos expansion (PCE) we use the more suitable exponential chaos basis, and write $T_r(t_n)$ as an exponential chaos expansion (ECE):

$$T_r(t_n, \boldsymbol{\xi}) = \sum_{s=0}^{N_S} \hat{T}_{r,s}(t_n) \Psi_s(\boldsymbol{\xi}) \tag{7.21}$$

Inserting Eq. 7.21 into Eq. 7.18 and projecting onto the EC basis $\{\Psi_s(\boldsymbol{\xi})\}$ yields the unknown solution coefficients $\hat{T}_{r,s}$ by virtue of the orthogonality of the discrete EC basis $\{\Psi_s(\boldsymbol{\xi})\}$ (for details see Fluck and Crawford (2017b)):

$$\hat{T}_{r,s}(t_n) = \frac{\rho}{2} c \Delta r \left(A \cdot \sum_{k=0}^{K-1} Y_{\tau,k} E_k(t_n) I_{1,k}(t_n) + B \cdot \sum_{k=0}^{K-1} Y_{\tau,k} E_k(t_n) I_{2,k}(t_n) + \sum_{k=0}^{K} Y_{\tau,k} E_k(t_n) I_{3,k}(t_n) \right) \tag{7.22}$$

with K the number of terms in the airfoil coefficient series (Fig. 7.5), and

$$\begin{aligned} I_{1,k}(t_n) &:= \langle F_k(t_n, \boldsymbol{\xi}) \quad\quad\quad\quad\quad\quad\quad , \ \Psi_s(\boldsymbol{\xi}) \rangle \\ I_{2,k}(t_n) &:= \langle F_k(t_n, \boldsymbol{\xi}) \ \tilde{u} \ (t_n, \boldsymbol{\xi}), \ \Psi_s(\boldsymbol{\xi}) \rangle \\ I_{3,k}(t_n) &:= \langle F_k(t_n, \boldsymbol{\xi}) \ \tilde{u}^2(t_n, \boldsymbol{\xi}), \ \Psi_s(\boldsymbol{\xi}) \rangle \end{aligned} \tag{7.23}$$

with the discrete projection sums $I_{1,k}$, $I_{2,k}$, and $I_{3,k}$ from the inner product as defined in Eq. 7.20.

If we consider $\Psi_s(\boldsymbol{\xi})$ as multivariate harmonics in the chaos space, each $\lambda_m \in \boldsymbol{\Lambda}_s$ a discrete base frequency of the s-th chaos exponential in the m-th chaos dimension (corresponding to the m-th random variable ξ_m), and $1/N$ as the sample rate, then Eqs. 7.19 and 7.20 directly lead to a multidimensional discrete Fourier transform (Marks II, 2009; Amidror, 2013)[17] and the projection of Eq. 7.23 can be evaluated efficiently via a multidimensional Fast Fourier Transform.

With Eqs. 7.22 and 7.23, Eq. 7.21 yields a compact and quick solution for the varying blade thrust at each blade element not only for one sample time series (as Eq. 7.4), but for all possible realizations of $\boldsymbol{\xi}$, i.e. for all possible wind field random seeds over all time (i.e. covering all possible constructive/ destructive inferences of all frequency components in the wind field). The advantages discussed in the introduction are obvious:

1. For any new turbine design only Eq. 7.22 needs to be updated for Eq. 7.21 to very quickly yield a large ensemble of blade loads. The projection itself (Eq. 7.23) is independent of the turbine geometry.
2. Since Ψ_s in Eq. 7.21 are known the stochastic properties (e.g. probability distributions and thus return periods) of blade loads will only depend on $\hat{T}_s$. Hence it will be possible to extract stochastic moments (e.g. load mean, variance) and thus long term loads for each design directly and very quickly from Eq. 7.22. We previously showed this for a polynomial chaos basis (Fluck and Crawford, 2017b); similar equations can be derived for an ECE.

[17] N.B.: This is *not* the usual Fourier analysis in time or (geometric) space, but rather in random coordinates of the stochasitc space.

In the following results for (1) will be presented. To yield long term loads the wind inflow expression (Eq. 7.9) needs to be modified. In line with the usual deterministic analysis, Eq. 7.9 gives the turbulent wind speed for medium samples length, where u_0 is assumed to be constant for each sample, but variable over the long term (for details see e.g. (IEC 61400-1, Ed. 3, 2005; Burton et al., 2011)). To obtain long term loads, these long term variations of u_0 need to be included into Eq. 7.9, e.g. by substituting the constant u_0 with $\tilde{u}_0(\xi_0)$ of some appropriate long term (e.g. Weibull) probability distribution. This step and deriving the equations to relate $\hat{\boldsymbol{T}}$ to probability distributions for blade loads will be left for future work.

7.3 Results

In this section we compare BEM results for thrust loads on individual blade elements, as well as integrated over a rotor blade, obtained from both deterministic and stochastic methods. The deterministic simulation Eq. 7.4 was implemented in MATLAB and solved iteratively. The results of that code were successfully verified against results from NREL's FAST code (Jonkman and Buhl, 2005) for steady state conditions, i.e. for constant wind speed, and no yaw or rotor axle tilt. For unsteady conditions, i.e. turbulent wind inflow varying in space and time, FAST uses the Generalized Dynamic Wake model (Moriarty and Hansen, 2005), while our stochastic solution employs a frozen wake model. To compare like-for-like aerodynamic models in the deterministic and the stochastic case we thus use our own implementation of the unsteady BEM model (Eq. 7.4) as deterministic base line. For the stochastic case Eqs. 7.18 and 7.22 were solved.

7.3.1 Model setup

In the following a generic three-bladed wind turbine with $R = 35$ m rotor radius is analyzed. To avoid any control peculiarities constant rotor speed is prescribed at $\Omega = 20$ rpm. Table 7.1 summarizes the blade geometry and element locations. To limit computational effort for the deterministic simulations only seven evenly spaced elements were used.

Table 7.1: Blade geometry and element locations for a generic $R = 35$ m wind turbine.

element #		1	2	3	4	4	6	7
relative position $\tau = r/R$	[-]	0.14	0.29	0.43	0.57	0.71	0.86	0.96
element center r	[m]	5.0	10	15	20	25	30	33.75
element length Δr	[m]	5.0	5.0	5.0	5.0	5.0	5.0	2.5
chord c	[m]	2.3	2.8	2.4	2.0	1.6	1.3	1.0
twist β	[°]	28	14	9.0	5.0	3.0	1.0	0.0

We use data from the NREL S825 airfoil (Somers, 2005) for all blade sections fitted between $\phi = \pm 60\,^\circ$ by Eq. 7.12 with $K = 11$ (Fig. 7.5). Note that for this study we arbitrarily chose a reasonable airfoil. Hence an exact fit for the c_x curve in Fig. 7.5 was not our primary goal. However, we took care to retain generic features of the airfoil (linear lift, stall, post stall recovery). Blade pitch is set to $\tau_0 = 2°$ and twist according to Tab. 7.1. We set $h_{hub} = 90$ m, $u_0 = 12$ m/s, $a = 0.2$ (Jonkman and Kilcher, 2012), and use IEC normal turbulence class A (IEC 61400-1, Ed. 3, 2005). We use $N_F = 7$ logarithmically spaced frequencies $\vec{f} = \vec{\omega}/(2\pi) = [f_k] \in [f_1, f_{N_F}] = [1/600, 5]$ Hz with $f_m = 10^{a_m}$ and $a_m = \log_{10}\left(\frac{f_{N_F}}{f_1}\right) \frac{m-1}{N_F-1}$ for $m = 1, \ldots, N_F$, and thus capture the variance contained in the turbulent peak of the wind energy spectrum (Burton et al., 2011). Loads are calculated at $t_n = n\Delta t$ with $\Delta t = 0.1$ s intervals. Only the axial wind component of the wind is used.

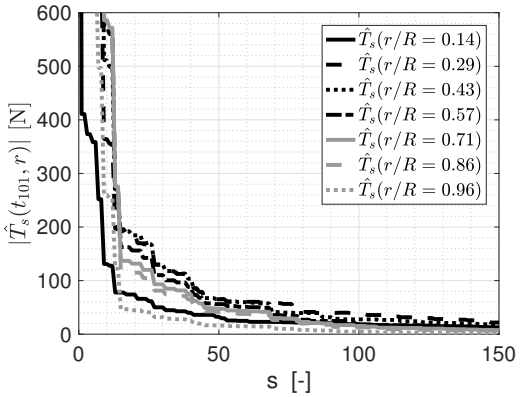

Figure 7.7: Spectrum of the chaos modes $\hat{T}_s$ for the first 150 modes for each element at $t_n = 10$ s.

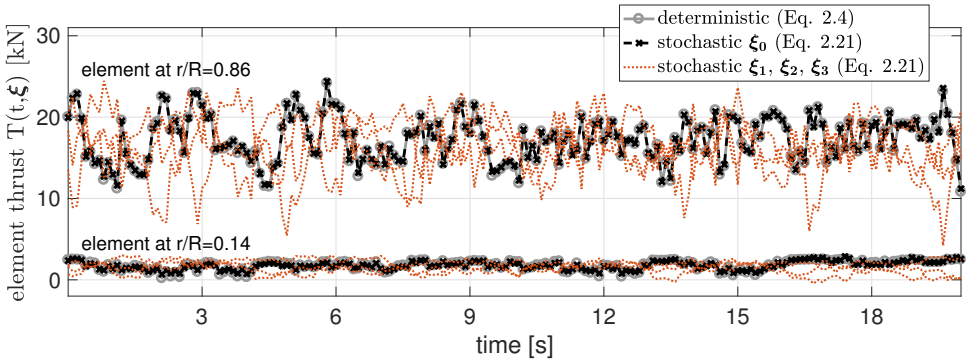

Figure 7.8: Thrust time series for two blade elements: Deterministic solution from random seed $\boldsymbol{\xi}_0$, stochastic solution from same random seed, and three other realizations of the stochastic solution (from different random seeds $\boldsymbol{\xi}_i \neq \boldsymbol{\xi}_0$).

To capture the stochastic dimension via ECE (Eq. 7.23), the stochastic functions (F_k, $F_k\tilde{u}$, $F_k\tilde{u}^2$) need to be sampled adequately. For the present example we found stochastic sampling with $N = 8$ and a resolution with $p = 2$ sufficient. For $N_F = 7$ frequencies this results in a total of $N_S \approx 8 \cdot 10^5$ basis functions Ψ_s. However, only a few of these are actually significant, particularly the low order ones $\boldsymbol{\Lambda}_i = \{\lambda_{mi}\}$ with $\sum|\lambda_{mi}| \leq 3$, and obviously $\boldsymbol{\Lambda}_0 = \{\lambda_{m0}\}$ with $\sum|\lambda_{m0}| = 0$. Hence we truncate the EC series (Eq. 7.21) to $N_S = 50$, and only use the most important terms. Fig. 7.7 shows an excerpt of the chaos spectrum in terms of the absolute value of each mode $|\hat{T}_s|$. The amplitude spectra for other time steps are almost identical. Hence, the importance sorting of the spectra is based on the amplitudes at one time step only. Note, however, that although the amplitudes are almost constant over time for each blade element, the stochastic phases $\tan(\mathrm{Im}[\hat{T}]/\,\mathrm{Re}[\hat{T}])$ at each time step differ.

In the following we focus on turbine blade thrust loads. Torque loads can be calculated similarly by substituting the torque coefficient for the thrust coefficient in all proceeding equations. Any derived load, such as e.g. blade root bending moments, tower base loads, or rotor power, can be calculated directly in the well-known way from these basic loads.

7.3.2 Element thrust time series

Fig. 7.8 compares the first 10 s of the unsteady thrust force on two different blade elements obtained from either the deterministic BEM equation (Eq. 7.4) or from four

realizations for of the EC solution (Eq. 7.21). Because we use a frozen wake formulation no start-up transients are appearing. For comparability both the deterministic and stochastic analysis are based on a 20 s wind realization generated from the reduced order model with $N_F = 7$. The first stochastic realization (labeled $\boldsymbol{\xi}_0$) is generated from the same random seed $\boldsymbol{\xi}_0$ and the same phase increments $\Delta\boldsymbol{\theta}$ as used for the deterministic wind realization. For this case the deterministic and the stochastic solution should be identical for a perfect ECE with $N \to \infty$ and $N_S \to \infty$. Fig. 7.8 shows that even for our choice of $N = 8$ and $N_S = 50$ very good agreement is achieved.

However, instead of only a single solution to one specific wind speed time series, the ECE solution contains all possible phase angle combinations, and thus all possible thrust load solutions. This is illustrated by three further realizations ($\boldsymbol{\xi}_1$, $\boldsymbol{\xi}_2$, $\boldsymbol{\xi}_3$) of the stochastic solution (Fig. 7.8, dotted lines). These additional solution samples were generated directly from the ECE solution (Eq. 7.21), this time with different random vectors $\boldsymbol{\xi}$ (but still the same phase increments $\Delta\boldsymbol{\theta}$).[18]

7.3.3 Element thrust covariance

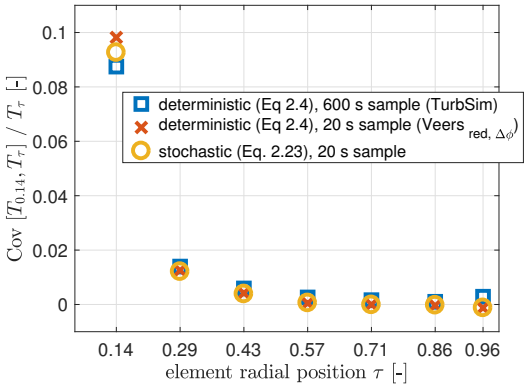

Figure 7.9: Normalized blade element thrust covariance.

Fig. 7.9 shows the normalized thrust force covariance $Cov[T_{0.14}, T_\tau]/T_\tau$ for an element at the radial position $\tau = r/R$ and the thrust at the first element $T_{0.14}$. Results from the new stochastic approach are compared to two different deterministic results with the input wind

[18] The results presented here and in the following sub-sections are calculated each based on one specific realization of phase angle increments $\Delta\boldsymbol{\theta}$. Note, however, that these fixed phase angles were *not* the same throughout the study, but generated anew for each new simulation.

(a) generated from the reduced order Veers' wind model (cf. Section 7.2.2) with $N_F = 7$ frequencies prescribed on a radial grid of $N_P = 210$ points (Fig. 7.6) with fixed phase increments $\Delta\boldsymbol{\theta}$. This is labeled '$\mathbf{Veers}_{\mathbf{red},\Delta\theta}$';

(b) synthesized through the stochastic wind simulator TurbSim (Kelley and Jonkman, 2007), labeled '**TurbSim**'.

Loads were calculated from the conventional BEM model (Eq. 7.4) for 100 different realizations of 600 s, resulting in total of 1,000 minutes of realized data.

The stochastic results are obtained from 3,000 realizations of the stochastic EC solution (Eq. 7.21) for 20 s, i.e. the same 1,000 minutes total data. The wind input was set up identically to (a) for the deterministic case with fixed phase increments $\Delta\boldsymbol{\theta}$. Note that, while TurbSim, case (b), on a 15×15 Cartesian wind speed data grid used $N_F \approx 3,000$ frequencies and thus relied on $N_R \approx 7 \cdot 10^5$ random numbers, the reduced order model (case (a) the stochastic solution) used only $N_R = N_F = 7$ frequencies.

Fig. 7.9 shows that the stochastic results agree almost perfectly with the deterministic case based on the same wind speed input (20 s from the reduced order Veers' model, case (i)). This is not very surprising: with the same random seed, the stochastic method reproduces the deterministic time series results almost exactly (Fig. 7.8). For enough realizations, with enough different random seeds, the results for each individual realization will be different, however, the statistics of the data set should converge.

It was demonstrated by Fluck and Crawford (2017a) that the reduced order version of Veers' model preserves the same wind field covariance as obtained from a full TurbSim run. Fig. 7.9 shows that the stochastic model preserves that covariance from the deterministic results based on TurbSim input, too.[19] This is important, because the dynamic blade loads (as the sum of the correlated loads on each blade element) can be calculated correctly only if the covariance is preserved.

7.3.4 Thrust force statistics

Fig. 7.10 compares the probability distribution function (PDF) of unsteady thrust loads integrated over a single blade from the usual deterministic model to results from the

[19] For comparability the results form each 600 s TurbSim sample were split into 30 individual sample of 20 s each.

new stochastic approach as above. Once a load probability distribution like Fig. 7.10 is obtained extrapolation to long term loads, e.g. life time extreme loads (Burton et al., 2011), is straight forward. Again, the stochastic results agree almost perfectly with the deterministic case from the reduced order Veers' model (case (a)), see Fig. 7.10, left. Slight differences result possibly from the truncation of the ECE to $N_S = 50$ terms.

Fig. 7.10, right, shows the blade load PDFs obtained from the stochastic model compared to results based on TurbSim wind (case (b)). Although the agreement is not quite perfect anymore, a good match is still obtained. Considering the enormous reduction in the number of random variables involved and the computational speed-up, particularly when analyzing various different turbine geometries (see next section), this agreement is remarkable.

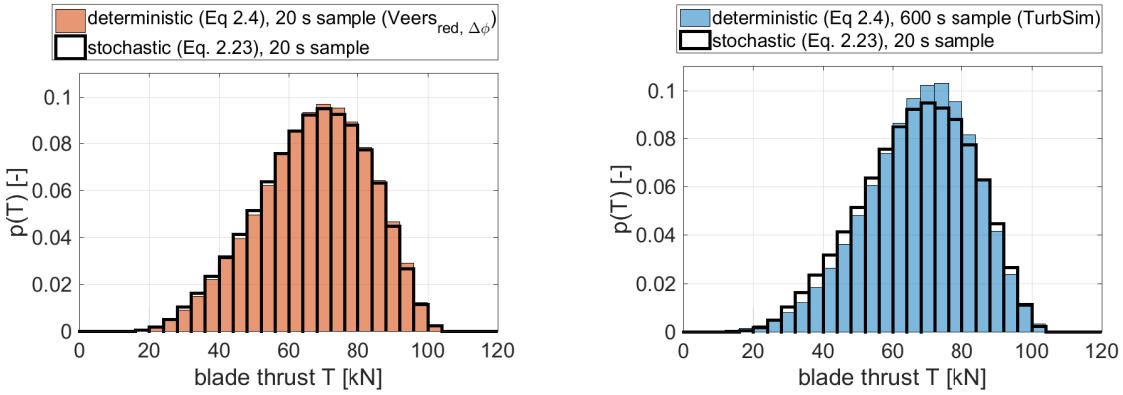

Figure 7.10: Probability distribution of unsteady blade thrust load obtained from 100 deterministic solutions compared to results from one stochastic solution. Left: deterministic solution based on a wind field from the reduced order Veers wind model (7 random numbers); Right: deterministic solution based on a TurbSim wind field ($7 \cdot 10^5$ random numbers).

The reduced order wind model was previously studied for $N_F = 20$ frequencies Fluck and Crawford (2017a). Using $N_R = N_F = 20$ random variables for the stochastic projection was not feasible with the MATLAB code at hand and the desktop computational resources available for the projection (due memory limitations incurred with the current implementation of the stochastic projection). However, there are indications that increasing the number of frequencies only slightly (e.g. $N_F = 10$, a quite realistic number with some code optimization and better memory management)

could already bring significant improvement. Moreover, Fluck and Crawford (2016b) show that wind speed interpolation (as commonly used to obtain on-blade wind data from a fixed grid of stored data points) distorts the stochastic properties of the wind field. For the reduced order version of Veers' model we used a radial grid, set up such that no interpolation was necessary. This was not possible for the TurbSim data. Thus, nearest neighbor interpolation was employed. It is likely that this distorted the blade load PDFs relative to the stochastic method. A detailed study of the remaining discrepancy between blade load PDFs, where the difference originates from, and how they can be further reduced, is left for future work.

7.3.5 Computational effort

At this point a quantitative comparison of the computational costs is difficult, because currently the equations are implemented in an experimental MATLAB code, where an easy development of the method took priority over computational efficiency. Thus any time requirement analysis is inevitably biased by limited code efficiency. However, we will give a rough estimate of the time required to calculate the PDF of Fig. 7.10 on a Intel i5 quad core processor with no explicit parallelization in the MATLAB code. With the deterministic method it took roughly 10 minutes to solve 100 samples of 600 s duration. On the other hand, 3,000 realizations of the stochastic 20 s solution, Eq.7.21 can be obtained within about 30 s. When concerned with design optimization, where multiple candidate designs have to be evaluated quickly, the stochastic method clearly shows its advantage. A typical optimization might require 50 iterations. With 20 design variables and a finite differencing approach to estimate design gradients the deterministic method would take $T_d = 50 \cdot (20 + 1) \cdot 10$ min $= 175$ hours vs. $50 \cdot (20 + 1) \cdot 30$ s $= 8.75$ hours for the stochastic solution (both covering 1,000 minutes of simulated data for each design evaluation). Moreover, a gradient based optimization will be very sensitive to obtaining precise design variable gradients. When optimizing with respect to long term loads these gradients have to be extrapolated from load PDFs as in Fig. 7.10. To improve these gradients in the deterministic case one needs to gather more data, i.e. analyze more samples. For the stochastic solution, on the other hand, load statistics (mean, variance, and higher order moments), thus the load PDF and eventually long term loads (as well as their finite gradients) can be extracted directly and analytically from the series coefficients $\hat{T}$. This means gradients can be estimated much more consistently without relying on a large number

of realizations to sufficiently populate a PDF. Discussing this step is outside the scope of this introductory work. It will thus be deferred to a forthcoming publication.

These gains, however, do not come for free. While TurbSim takes about 25 minutes to generate 100 wind field samples of 600 s duration for the deterministic method, calculating the stochastic projection (Eq. 7.23) for a 20 s time series in its current implementation requires roughly 3.2 hours. However, both synthesizing the wind field as well as executing the stochastic projection is performed prior to the actual design evaluation, i.e. in a pre-processing step before the optimization loop. With code optimization and parallelization we expect to significantly reduce this time demand. Here it is crucial to note that the projection is independent of the turbine design. Thus, the computational cost associated with the stochastic projection occurs only once during a turbine optimization. With $K = 11$ and $N_S = 50$ the computational costs incurred at run-time associated with updating $\hat{T}_{r,s}$ in Eq. 7.22 is negligible. Hence, in an optimization context, these costs are irrelevant. Instead, the run-time costs of obtaining a big enough data set (e.g. 100 solutions of 600 s realizations) is the critical one. Here, the huge advantage of stochastic method becomes obvious: 10 minutes for the deterministic method vs. 30 seconds for the stochastic one.

7.4 Conclusions

In previous work a stochastic solution to linear aerodynamic equations for a simple horseshoe vortex wing model subject to turbulent (stochastic) atmospheric wind was presented. This work was extended here to non-linear Blade Element Momentum (BEM) equations set up to calculate wind turbine blade thrust (and similarly torque, as well as derived loads such as e.g. blade root bending moments, or tower base loads) in turbulent inflow. Similar to previous work, a stochastic projection approach was chosen to arrive at a stochastic solution. However, instead of a projection onto a polynomial chaos basis (the common choice) a new basis, composed of multivariate complex exponential functions, the exponential chaos (EC), was introduced. This new basis permitted a rapid projection using multidimensional Fast Fourier Transform, and, moreover, allowed representation of the stochastic domain with only a small subset of the stochastic basis functions.

As usual, the number of random variables which the stochastic method can handle is limited. Hence, a reduced order model for the stochastic representation of the turbulent atmospheric wind was used. It was shown that the stochastic model reproduces the deterministic time stepping solution of the BEM equations for a generic wind turbine rotor example if both solutions, the deterministic and the stochastic one, are generated from the same random seed. Even with a highly truncated expansion series (50 stochastic basis functions) a very good agreement between deterministic and stochastic solutions is maintained. Moreover, it was shown that also the covariance of element load on different stations along the blade is maintained well with the stochastic method.

Instead of only presenting a single solution to a single realization of the inflow wind field (e.g. a 600 s sample), the stochastic solution contains all possible realizations. It was shown that this can be used to very quickly produce probability distribution functions (PDF) of the loads obtained form an unsteady BEM analysis, and that the resulting PDFs are almost identical. It was also shown that the blade load PDFs obtained through the stochastic method match the ones from the deterministic method based wind fields generated through TurbSim, a standard tool used in industry for wind field simulation. As the stochastic method allows calculation of such a load PDF for a specific turbine design in several seconds (vs several minutes for a deterministic analysis), the assessment of long term loads (e.g. extreme and fatigue loads) now becomes accessible within a turbine optimization routine.

However, the fast stochastic analysis comes at a price: a costly stochastic projection. Yet, the projection equations presented here are arranged such that the extensive part is a function of the wind conditions only and independent of the turbine geometry. Hence the projection can be carried out off-line for any representative site, independently of the turbine design, and prior to actual turbine optimization. Future work will seek to accelerate this projection (e.g. by parallelizing the computations), and aim for a detailed study of long term loads, including methods to extract long term statistics directly from the stochastic series. Moreover, controller design for unsteady rotor speed will be included, the frozen wake assumption will be relaxed, and eventually a full unsteady stochastic wind turbine optimization framework will be set up to include life time loads.

Chapter 8

Conclusions and Future Work

This chapter wraps up this dissertation by summarizing the conclusions as well as the fundamental assumptions made. Finally an outlook onto possible future work is given.

8.1 Conclusions

The principal objective of our work was to develop a method to assess life time unsteady wind loads, which in the future can be used in a new wind turbine design optimization framework. These new methods and the surrounding work were presented in this dissertation, grouped into three building blocks: analyzing *unconventional geometries* via Lagrangian vortex methods (Chapter 2); handling *turbulent wind* as input for stochastic models (Chapters 3 and 4); and fast analysis of *unsteady aerodynamic* loads via stochastic models (Chapters 5, 6, and 7). The dissertation itself is a collection of six research papers. Each of these papers is published or submitted for publication in a peer reviewed scientific journal. Fig. 8.1 summarizes the principal contributions and outcomes of this research. Together with this figure the remainder of this section summarizes our conclusions.

8.1.1 Unconventional geometries

Existing Lagrangian vortex models were modified to be capable to assess unconventional, non-planar, and strongly interacting lifting surfaces. This has been a challenge, because Lagrangian vortex models tend to become numerically unstable with vortex elements in close interaction. Hence it was questionable if these models are actually a

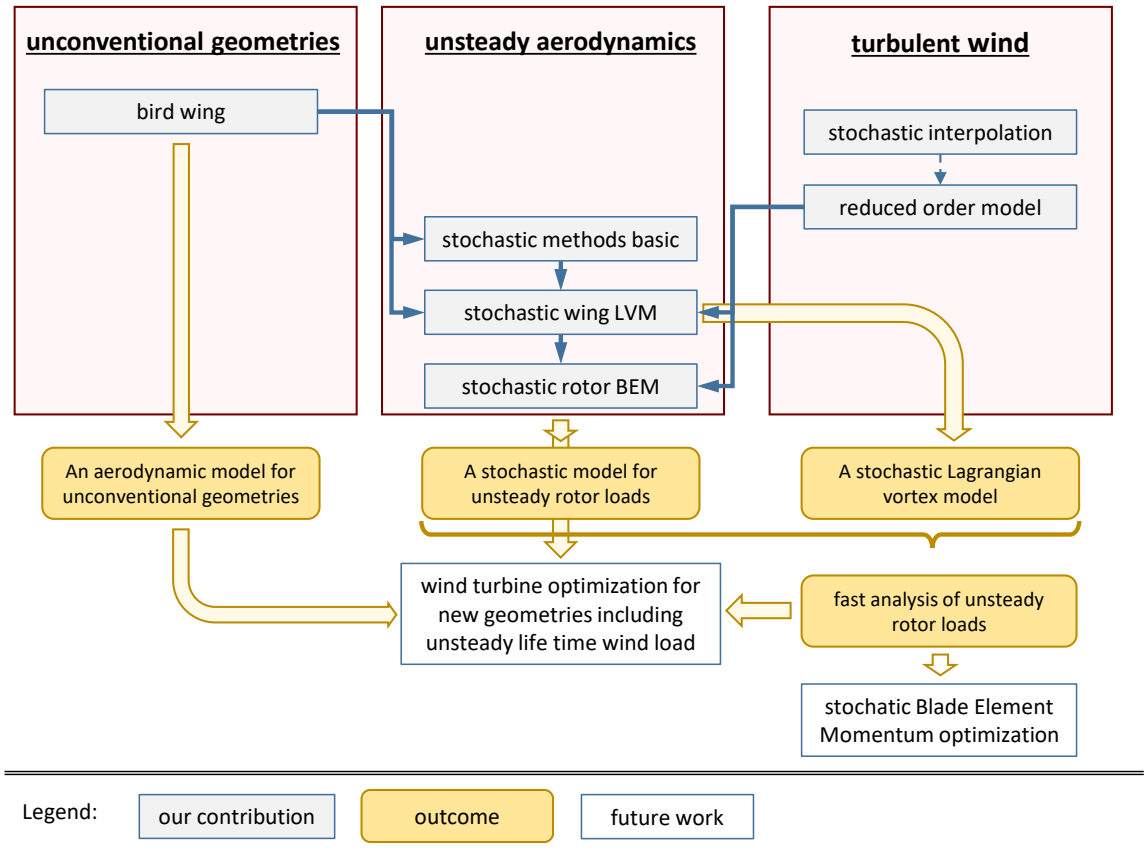

Figure 8.1: Principal research contributions and outcomes.

good choice for advanced wind turbine design.

We chose one of the possibly most complex wing geometries (bird wings with strongly interacting tip feathers, Fig. 2.1), and developed a reliable Lagrangian vortex model (lifting line formulation, Fig. 2.2) capable of analyzing these kinds of complex geometries. Thus we arrived at a model, which is now available to better understand bird flight, the way evolution has optimized these animal's wings, and potentially bring forward new bionic applications. In an initial study we found that (Section 2.6):

1. Introducing multiple tip feathers, horizontally and vertically spread to create a non-planar tip slotted wing, *can* be beneficial for in wing efficiency (i.e. the obtained glide ratio L/D), stall behavior, and/ or maximum lift.

2. Without optimization a 21% efficiency improvement of the best configuration with tip feathers over an elliptic wing of same aspect ratio but with no tip

feathers was found.

3. The details of the geometry of the tip feather is vital. Small changes can make a big difference, and not all configurations are beneficial in all situations.

Very good agreement between results from our extended lifting line model and experimental data was found (Section 2.3, especially Tab. 2.1 and Fig. 2.4). Thus, it was shown that a Lagrangian vortex model, in contrast to Blade Element Momentum equations, is capable to yield reliable results for highly unconventional wing or blade geometries, indeed. This was important to confirm before moving forward to advanced unsteady aerodynamic models and eventually wind turbine optimization where new geometries such as e.g. winglets, ailerons, swept or kinked blades, etc. are to be analyzed.

8.1.2 Turbulent wind

Turbulent wind fields can be regarded as three dimensional random fields with prescribed spatial and temporal statistics, such as auto and cross-spectrum, variance and covariance, auto and cross-correlation. In this dissertation we studied the way these fields are synthesized from a numeric model (Cahpter 4), and how the resulting (inevitably discrete) data is eventually interpolated when input into other analysis models, e.g. from a 'block of frozen wind' to data on a rotating wind turbine blade (Chapter 3).

Once wind speed (as well as data from other random processes) is obtained from a numerical model or an experimental measurement, it is only available at discrete data points (Chapter 3). Often these data points are spaced far enough apart (5-10 m) for the data to be only weakly correlated (Section 3.1). In this dissertation:

1. We revealed that for the typically available wind data linearly interpolating between discrete values (the most common method) distorts the statistical properties of the data series (Fig. 3.1 and Tab. 3.1).

2. To solve this problem an alternative was introduced in Section 3.2, based on random wind speed interpolation increments. In Section 3.3 it was demonstrated that this new method conserves the statistical properties of the original data much better than the conventional linear interpolation (Tab. 3.1).

On the other hand looking at wind models (Chapter 4) as an input to further analysis we found that currently these models rely on a large set of random numbers for synthesizing the wind (Section 4.1 and particularly Tab. 4.1). Because generating random seeds is cheap, previously there has been no incentive to be careful about the number of random variables in use. However:

1. A large number or random variables poses a problem for a stochastic treatment of wind loads. A fact not only relevant for wind turbine analysis, but for the analysis of stochastic wind loads on engineering structures in general.

2. Hence, before moving to stochastic models for wind turbine aerodynamics, it became necessary to find a new wind model, which relies on significantly less random variables than the previously available models.

3. In Section 4.2.2 we presented a new method, based on a separation of the temporal and spatial part of the random dimension of turbulent wind. This new model reduces the number of random variables used from the usual 10^5 to only 7-20 (Tab. 4.1), while conserving the statistical properties of the wind field (Section 4.3).

8.1.3 Unsteady aerodynamics (stochastic models)

In this block we combined the results from the previous blocks and eventually arrived at a stochastic model for unsteady aerodynamic loads (see Fig. 8.1). This resulted in:

A) A stochastic solution to a simple Lagrangian vortex model for unsteady blade loads on a translating blade/wing (Chapter 6).

B) A stochastic solution for the aerodynamic analysis of a wind turbine rotor with Blade Element Momentum theory (Chapter 7).

Together, (A) and (B) showed that a fast analysis of unsteady rotor loads is quite possible with the proposed stochastic methods. The conclusions for the Chapters 5-7 are summarized in the following.

So far conventional polynomial chaos methods were concerned with uncertain (but constant) boundary conditions or system parameters. Expanding on this we found in Chapter 5:

1. With slight modifications polynomial chaos expansion can be used for random processes varying in time (Section 5.3.3). Turbulent atmospheric wind can be regarded as such a random process (cf. Chapter 4).

2. Substituting the polynomial chaos basis with complex exponential functions (Fourier modes) yields a very simple solution for linear unsteady equations (Section 5.3.2).

3. Using such a stochastic series expansion we can obtain the system output (e.g. turbine blade loads resulting from turbulent wind inflow), and its stochastic properties, such as mean or variance, directly from one stochastic solution (Section 5.4, particularly Fig. 5.6).

By combining the new stochastic wind model for a limited set of random variables form above (Chapter 4) with the stochastic aerodynamic model (Chapter 5) we were able to obtain a stochastic solution for a wing/ blade translating in a three dimensional turbulent wind field (Chapter 6). Finally we switched to a new basis for a stochastic series expansion, introduced exponential chaos (Section 7.2.5), and arrived at a new model to solve the unsteady aerodynamic equations for wind turbine rotor loads directly in the stochastic domain (Section 7.2.6) – a process considerably faster than the repeated analysis of the equivalent deterministic equations (Section 7.3.5). With this we conclude for unsteady aerodynamic equations in general, and wind turbines aerodynamics in particular:

1. The stochastic model presented here and the conventional deterministic approach result in very similar stochastic properties of the dynamic loads along a turbine blade resolved with several elements (Sections 6.3 and 7.3). This includes two point statistics of loads on different stations along the blade (cross-correlation, covariance, cross-spectrum).

2. Assessing long term aerodynamic loads from *one* stochastic solution is much faster than from *multiple* solutions of the corresponding deterministic equation. For the examples considered the stochastic model yielded results in 1-5% of the time required by the deterministic model (Section 7.3.5). Thus analyzing unsteady aerodynamic loads becomes accessible within an aerodynamic optimization routine.

3. The stochastic model was successfully applied to a Lagrangian vortex model with linear airfoil properties (Chapter 6) as well as to non-linear Blade Element Momentum equations (Chapter 7). Combining both into a stochastic non-linear Lagrangian vortex model and eventually arriving a new stochastic optimization routine for novel blade geometries is left for future work.

In the Chapters 5 and 6 a stochastic solution to Lagrangian vortex equations for wing or blade loads was developed. However, in Chapter 7 we did not advance directly to a stochastic lifting line wind turbine optimization geared towards new geometries. Instead, we derived a stochastic solution for the Blade Element Momentum equations (see Fig. 8.1). The rational behind this is the *divide et impera* maxim. We did not have an unsteady Lagrangian vortex model for wind turbine aerodynamics readily available. Implementing such a model would not come without significant challenges (mainly based in handling the evolving helical wake structures) even before employing stochastic methods. Instead of jumping forward and trying to conquer all at once, we decided to divide the process in two sub-steps: first, develop a stochastic solution for a (more straight forward) conventional rotor aerodynamics model based on Blade Element Momentum theory; subsequently move on to the full Lagrangian vortex model for unconventional rotors, and eventually implement the new optimization framework. Due to the limited scope of this work we are content with completing the first step here. This step alone is valuable, as it now allows to bring unsteady loads and power production into the turbine optimization, particularly since today all certified wind turbine design codes use a variant of Blade Element Momentum theory, thus making the contributions in this dissertation directly relevant in industry. Possible future work will be outlined in the following section.

8.2 Model assumptions

Just like every model, the models presented in this dissertation are based on a few assumptions. Before looking at future work, which to a large extent will be concerned with relaxing these assumptions, we present a brief summary of the basic assumptions made in this work.

8.2.1 Lagrangian vortex model

The Lagrangian vortex model used in Chapters 2, 5, and 6 relies on the potential flow assumption, i.e. invicid and irrotational flow. To include viscous drag into the equations, experimental airfoil data (drag coefficients) was employed in Chapter 2. The good agreement between our results and experimental data (Section 2.3) show that this is a valid approach.

In Chapters 5 and 6 no drag term is included and a $c_l = 2\pi\alpha$ is assumed. This is probably the simplest version of a Lagrangian vortex model. Here, this choice seemed reasonable, because details of the wing/ blade geometry were not relevant. The goal was rather a fundamental feasibility study of the new stochastic methods for Lagrangian vortex equations.

For the results presented in Chapter 2 the wake was assumed to be fixed and aligned with the free stream velocity. We found that this simplification had little influence on the results, but brought a considerable reduction in computational effort (Section 2.5).

8.2.2 Stochastic wind model

To be applicable to the stochastic solutions procedures we sought, the stochastic wind model could only rely on a very limited number of random variables. Since every frequency used in the spectral wind model requires a random phase angle, only a very limited number of frequencies from the wind speed frequency spectrum could be included. This is a major simplification.

To further reduce the number of random variables in use, it was assumed that phase angles can be split into random phases at one base point, and deterministic phase increments at all other points. As discussed in Section 4.2 this is a significant simplification and obviously reduces the randomness contained in the system. However, as discussed in Section 4.3 the accuracy penalty is acceptable, particularly considering the enormous reduction in random variables necessary in the model.

These two steps (reducing the number of frequencies, and assuming deterministic phase increments) are doubtlessly significant simplifications. However, the figures in

Sections 6.3 and 7.3 demonstrate good agreement between results based on TurbSim wind (generated from the full spectrum with a full set of random phases) and from the reduced order model, and thus justify these simplifications.

8.2.3 Blade Element Momentum model

Besides the usual assumption of any Blade Element Momentum model (the most severe arguably: planar rotors and radial independence of blade elements) we assume in Chapter 7 frozen wake, i.e. constant induced velocities. This means (temporal) fluctuations are neglected, and instead mean values of the induced velocities are used. Considering the complexity and the many vague assumptions associated with dynamic wake models this is a fair assumption for showing the principal feasibility of the presented stochastic models, see discussion in Section 7.2.1. However, this certainly is a point to be relaxed in future work.

8.2.4 Stochastic projection and stochastic solution

For the stochastic projection and stochastic solutions presented in Chapters 5, 6, and 7 we employ the Fourier-Galerkin approach, or use polynomial or exponential chaos methods. All three options require that the solution can be expressed as a series of random functions which span the entire stochastic domain of the problem at hand, and (for practical relevance) that the employed series expansion converges with increasing number of terms. Since the present work is an engineering dissertation we did not dive into mathematical rigor to prove either of these two requirements. Instead we are content with finding that for the aerodynamic problems studied here (a) the chosen stochastic basis functions represent the stochastic space well enough, and (b) the stochastic series yields very accurate results with only a reasonable subset of terms. This is sufficient for practical engineering. A more rigorous treatment is left to the many better trained mathematicians out there.

8.3 Future work

In this dissertation the feasibility of Lagrangian vortex methods to analyze unconventional wing or blade geometries was confirmed. With the stochastic aerodynamic methods introduced in Chapters 5-7 a tool for relatively quick assessment of unsteady

turbine thrust and torque was provided. These are two important steps forward. However, in the long run the goal should be to arrive at an optimization framework, which will be able to expand to new blade geometries and include life time unsteady loads as well as unsteady power output dynamics into the coast function. However, progress happens in small increments, and each single research project extends the horizon of knowledge only by a tiny bit. Thus more work is left for the ones to follow.

From an engineering perspective the most obvious next step, as indicated in Fig. 8.1, is to complete the journey towards a wind turbine optimization for new geometries including unsteady life time wind loads. This will first of all require extending the stochastic wind model to a life time wind model. So far, the stochastic formulation is set up to capture the same information as captured in multiple 600 s samples of the same wind conditions, i.e. with the same mean wind speed. To capture life time loads this needs to be extended to a time span in the order of 20 years. To achieve this, the deterministic process can be adopted in the stochastic model. For a deterministic load assessment life time loads are assembled from multiple 600 s simulations at different mean wind speeds. Similarly the stochastic analysis can be extended by moving from our model with a constant mean wind speed to a new model where the mean wind speed is an additional random variable. If the frequencies in Eq. 4.8 are chosen such that they cover 600 s, and the random mean wind speed is set such that it represents the ten minute mean distribution correctly, life time wind speed fluctuations will be covered in a similar fashion as previously in the deterministic model (Burton et al., 2011). The challenge which remains is to find a proper representation of the long time variability of the 600 s mean wind speed.

Once a life time stochastic wind model is available two directions further forward become apparent:

1. Enhance the available stochastic Blade Element Momentum model:
   This could, for example, be relaxing the frozen wake assumptions, including a stochastic formulation for dynamic on blade effects (e.g a stochastic stall model, Bertagnolio et al. (2010)), considering variable speed operation, blade pitch, and/ or controller design, and eventually building a wind turbine optimizer around this new stochastic aerodynamics model. This could lead to an interesting study of how considering life time loads influences the 'optimal' aerodynamic (and possibly controller) design.

2. Apply the stochastic formulation of Chapter 7 to a Lagrangian vortex model: In Chapter 7 we showed that our stochastic formulation can be applied to non-linear equations, and that transferring the stochastic approach from a Blade Element Momentum model to a Lagrangian vortex model is in principle straight forward. However, some effort will be required to bring the stochastic projection of the vortex equations (cf. Section 7.2.6) into a shape, which can be solved sufficiently fast.

For either of these directions, a combination of the stochastic aerodynamic model with an appropriate structural model (possible a stochastic structural model as investigated by Ghulam (2016)) will eventually be necessary to include aero-structural effects. Moreover, combining the aerodynamic model with a larger scale economic model (as investigated e.g. by Broeer (2016)), including not only integral (i.e. time averaged) power production, but time resolved revenue based on the dynamic electricity market prize, as well as grid stability costs, could be a further step. This would allow to set up a true system level optimization (in the widest sense), which in turn could enable researchers and turbine designers to study improved turbine concepts to mitigate electrical grid stability issues, which currently arise from too much, too volatile, and too uncontrollable wind power feed-in.

Beyond the stochastic models geared towards wind turbines, the ideas presented in this dissertation could also be extended to other fields of applications. A stochastic wave model, to combine stochastic wind and wave forcing on an offshore wind turbine, and supply stochastic solution for the resulting loads is probably the most obvious one. Similarly an application to a stochastic analysis of wave and tidal power technologies could open up new perspectives and be very beneficial. Others promising applications are for example: stochastic analyses of bridge loads from wind forcing; or a stochastic analysis of the sailboat driving force generated from turbulent wind input.

On the other hand, the bird wing study of Chapter 2 revealed interesting insights into biomimetic means to improve wing or blade performance. With the lifting line code available much more can be investigated. For us, proceeding in that direction would have diverted too far from our principal objective (cf. Chapter 1.2). For future work, however, it would be valuable to actually embed the available lifting line model into a wing or blade optimization framework, and study which wing (tip) configuration is actually best. Combined with a sensitivity analysis this promises to reveal very

interesting insights into wing design. Chapter 2 showed already that distinct tip feather are beneficial in specific flight conditions, but detrimental in others, but a major question is left open: given a mechanical wing or blade, with limited ability to change its geometry during operation, do distinct tip feathers actually yield gross benefits over the whole range of operational conditions?

Bibliography

Abramowitz, M. and Stegun, I. A. (1972). Handbook of mathematical functions. Applied Mathematics series 55, National Buro of Standards.

AirfoilPrep (2014). NWTC Information Portal (AirfoilPrep). https://nwtc.nrel.gov/AirFoilPrep; Last modified 14-March-2014; accessed 10-June-2014.

Altın, M., Goksu, O., Teodorescu, R., Rodriguez, P., Jensen, B.-B., and Helle, L. (2010). Overview of recent grid codes for wind power integration. In *Optimization of Electrical and Electronic Equipment (OPTIM), 2010 12th International Conference on*, page 1152–1160. IEEE.

Amidror, I. (2013). *Mastering the discrete Fourier transform in one, two or several dimensions: pitfalls and artifacts*. Springer, London.

Anderson Jr, J. D. (1985). *Fundamentals of aerodynamics*. McGraw-Hill, New York, 2nd edition.

Ashuri, T., Zaaijer, M. B., Martins, J. R., van Bussel, G. J., and van Kuik, G. A. (2014). Multidisciplinary design optimization of offshore wind turbines for minimum levelized cost of energy. *Renewable Energy*, 68:893–905.

Aubin, N., Augier, B., Bot, P., Hauville, F., and Floch, R. (2016). Inviscid approach for upwind sails aerodynamics. How far can we go? *Journal of Wind Engineering and Industrial Aerodynamics*, 155:208 – 215.

Barnsley, M. F. (1986). Fractal functions and interpolation. *Constructive approximation*, 2(1):303–329.

Barnsley, M. F. and Harrington, A. N. (1989). The calculus of fractal interpolation functions. *Journal of Approximation Theory*, 57(1):14–34.

Bergami, L. and Gaunaa, M. (2014). Analysis of aeroelastic loads and their contributions to fatigue damage. In *Journal of Physics: Conference Series*. IOP Publishing.

Bertagnolio, F., Rasmussen, F., Sørensen, N. N., Johansen, J., and Madsen, H. A. (2010). A stochastic model for the simulation of wind turbine blades in static stall. *Wind Energy*, 13(4):323–338.

Bladed (2012). *Bladed Theory Manual, Version 4.3*. Garrad Hassan & Partners Ltd, Bristol, UK.

Boettcher, F., Peinke, J., et al. (2007). Small and large scale fluctuations in atmospheric wind speeds. *Stochastic environmental research and risk assessment*, 21(3):299–308.

Bortolotti, P., Bottasso, C. L., and Croce, A. (2016). Combined preliminary–detailed design of wind turbines. *Wind Energy Science*, 1(1):71–88.

Bottasso, C. L., Campagnolo, F., and Croce, A. (2012). Multi-disciplinary constrained optimization of wind turbines. *Multibody System Dynamics*, 27(1):21–53.

Bouboulis, P. (2012). *Fractal Interpolation. Theory and Applications in Image Compression*. LAP Academic Publishing.

Broeer, T. (2016). *Analysis of Smart Grid and Demand Response Technologies for Renewable Energy Integration: Operational and Environmental Challenges*. PhD thesis, University of Victoria.

Broeer, T., Fuller, J., Tuffner, F., Chassin, D., and Djilali, N. (2014). Modeling framework and validation of a smart grid and demand response system for wind power integration. *Applied Energy*, 113(0):199–207.

Buhl, M. L. (2008). MCrunch user's guide for version 1.00. Tech. Rep. NREL/TP-500-43139, National Renewable Energy Laboratory.

Burton, T., Jenkins, N., Sharpe, D., and Bossanyi, E. (2011). *Wind Energy Handbook*. Wiley, Chichester, West Sussex.

Calif, R. and Schmitt, F. (2012). Modeling of atmospheric wind speed sequence using a lognormal continuous stochastic equation. *Journal of Wind Engineering and Industrial Aerodynamics*, 109:1–8.

Calif, R., Schmitt, F. G., and Huang, Y. (2013). Multifractal description of wind power fluctuations using arbitrary order hilbert spectral analysis. *Physica A: Statistical Mechanics and its Applications*, 392(18):4106–4120.

Cameron, R. H. and Martin, W. T. (1947). The orthogonal development of non-linear functionals in series of fourier-hermite functionals. *Annals of Mathematics*, 48(2):pp. 385–392.

Chew, K.-H., Tai, K., Ng, E., and Muskulus, M. (2016). Analytical gradient-based optimization of offshore wind turbine substructures under fatigue and extreme loads. *Marine Structures*, 47:23 – 41.

Choe, Y., Byon, E., and Chen, N. (2015). Importance sampling for reliability evaluation with stochastic simulation models. *Technometrics*, 57(3):351–361.

Cline, S., McWilliam, M. K., Lawton, S., and Crawford, C. (2011). Validation of potential flow aerodynamics for horizontal-axis wind turbines in steady conditions using the mexico project experimental data. In *30th ASME Wind Energy Symposium/49th AIAA Aerospace Sciences Meeting and Exhibit, Orlando, FL.*

Constantine, P. G., Doostan, A., and Iaccarino, G. (2009). A hybrid collocation/galerkin scheme for convective heat transfer problems with stochastic boundary conditions. *International journal for numerical methods in engineering*, 80(6-7):868–880.

Cosin, R. and Catalano, F. M. (2009). Aerodynamic analysis of the use of multi-winglets in light aircrafts. In *Brazilian Symposium on Aerospace Eng. & Applications, 3rdCTA-DLR Workshop on Data Analysis & Flight Control, September 14-16, 2009, S. J. Campos, SP, Brazil.*

Davis, P. J. and Rabinowitz, P. (1984). *Methods of numerical integration.* Academic Press, Orlando.

Desai, A. and Sarkar, S. (2010). Analysis of a nonlinear aeroelastic system with parametric uncertainties using polynomial chaos expansion. *Mathematical Problems in Engineering*, 2010. Article ID 379472.

Doenhoff, A. E. v. and Abbot, I. H. (1959). *Theory of wing sections. Including a summary of airfoil data.* Dover, New York.

Doubrawa, P., Barthelmie, R. J., Wang, H., and Churchfield, M. J. (2017). A stochastic wind turbine wake model based on new metrics for wake characterization. *Wind Energy*, 20(3):449–463. we.2015.

Dörenkämper, M., Tambke, J., Steinfeld, G., Heinemann, D., and Kühn, M. (2014). Atmospheric impacts on power curves of multi-megawatt offshore wind turbines. *Journal of Physics: Conference Series*, 555(1):012–029.

Eberhardt, S. (2011). Wingtip feathers, including forward swept feathers, and associated aircraft systems and methods. US Patent 7,900,876.

Emeis, S. (2012). *Wind Energy Meteorology: Atmospheric Physics for Wind Power Generation*. Springer, Heidelberg, Germany.

Etkin, B. (1981). Turbulent wind and its effect on flight. *Journal of Aircraft*, 18(5):327–345.

Faltinsen, O. M. (2005). *Hydrodynamics of high-speed marine vehicles*. Cambridge university press, New York.

Fluck, M. and Crawford, C. (2014). A lifting line model to investigate the influence of tip feathers on wing performance. *Bioinspiration & Biomimetics*, 9(4).

Fluck, M. and Crawford, C. (2016a). Exploring stochastic models for fast analysis of unsteady wing aerodynamics. In *18th AIAA Non-Deterministic Approaches Conference, AIAA SciTech*, San Diego, California. AIAA.

Fluck, M. and Crawford, C. (2016b). Minimizing errors in interpolated discrete stochastic wind fields. *Journal of Wind Engineering and Industrial Aerodynamics*, 152:15 – 22.

Fluck, M. and Crawford, C. (2016c). A stochastic aerodynamic model for stationary blades in unsteady 3d wind fields. In *Journal of Physics: Conference Series*, volume 753. IOP Publishing.

Fluck, M. and Crawford, C. (2017a). An engineering model to generate 3d turbulent wind fields from a limited set of random variables. *Wind Energy Science*. accepted for discussion.

Fluck, M. and Crawford, C. (2017b). Fast analysis of unsteady wing aerodynamics via stochastic models. *AIAA Journal*, 55(3):719–728.

Fluck, M., Gerhardt, F. C., Pilate, J., and J. Flay, R. G. (2010). Comparison of potential flow-based and measured pressure distributions over upwind sails. *Journal of Aircraft*, 47(6):2174–2177.

Fung, J. C. H., Hunt, J. C., Malik, N., and Perkins, R. (1992). Kinematic simulation of homogeneous turbulence by unsteady random fourier modes. *Journal of Fluid Mechanics*, 236:281–318.

Gant, S. and Stallard, T. (2008). Modelling a tidal turbine in unsteady flow. In *Proceedings of the Eighteenth (2008) International Offshore and Polar Engineering Conference*, page 473–480.

Ghanem, R. G. and Spanos, P. D. (1991). *Stochastic finite elements: a spectral approach*. Springer, New York.

Ghulam, M. (2016). *High Fidelity Micromechanics-Based Statistical Analysis of Composite Material Properties*. PhD thesis, University of Victoria.

Graf, P. A., Stewart, G., Lackner, M., Dykes, K., and Veers, P. (2016). High-throughput computation and the applicability of monte carlo integration in fatigue load estimation of floating offshore wind turbines. *Wind Energy*, 19(5):861–872.

Guo, Q. (2013). *Incorporating stochastic analysis in wind turbine design: data-driven random temporal-spatial parameterization and uncertainty quantication*. PhD thesis, Iowa State University.

GWEC (2015). *Global Wind Report - Annual Market Update 2015*. Global Wind Energy Council.

Hansen, M. O. (2008). *Aerodynamics of wind turbines*. Earthscan, London.

Heier, S. (2014). *Grid integration of wind energy*. John Wiley & Sons, Chichester, West Sussex.

HM Government (2013). Offshore wind industrial strategy. Technical report, The Government of Great Britain.

Hoerner, S. (1952). Aerodynamic shape of the wing tips. Tech. Rep. 5752, US Air Force.

Holttinen, H., Meibom, P., Orths, A., Lange, B., O'Malley, M., Tande, J. O., Estanqueiro, A., Gomez, E., Söder, L., Strbac, G., et al. (2011). Impacts of large amounts of wind power on design and operation of power systems, results of iea collaboration. *Wind Energy*, 14(2):179–192.

Hossain, A., Rahman, A., Iqbal, A., Ariffin, M., and Mazian, M. (2011). Drag analysis of an aircraft wing model with and without bird feather like winglet. *International Journal of Mechanical, Aerospace, Industrial, Mechatronic and Manufacturing Engineering*, 5(9):30–35.

Hummel, D. (1980). The aerodynamic characteristics of slotted wing-tips in soaring birds. In *Proceedings of the 17th International Ornithology Congress*, volume 1, page 391 – 396.

IEC 61400-1, Ed. 3 (2005). International standard 61400-1 (3rd edition): Wind turbines, part 1: Design requirements. *International Electrotechnical Commission*.

Jonkman, J. and Kilcher, L. (2012). Turbsim user's guide: Version 1.06. 00. Technical Report Draft Version, National Renewable Energy Laboratory.

Jonkman, J. M. and Buhl, M. L. (2005). Fast user's guide. Technical Report NREL/EL-500-38230, National Renewable Energy Laboratory.

Junge, T., Gerhardt, F. C., Richards, P., and J. Flay, R. G. (2010). Optimizing spanwise lift distributions yacht sails using extended lifting line analysis. *Journal of Aircraft*, 47(6):2119–2129.

Kantz, H., Holstein, D., Ragwitz, M., and Vitanov, N. K. (2004). Markov chain model for turbulent wind speed data. *Physica A: Statistical Mechanics and its Applications*, 342(1–2):315 – 321. Proceedings of the VIII Latin American Workshop on Nonlinear Phenomena.

Kareem, A. (2008). Numerical simulation of wind effects: A probabilistic perspective. *Journal of Wind Engineering and Industrial Aerodynamics*, 96(10–11):1472 – 1497. 4th International Symposium on Computational Wind Engineering (CWE2006).

Karimi, M., Hall, M., Buckham, B., and Crawford, C. (2017). A multi-objective design optimization approach for floating offshore wind turbine support structures. *Journal of Ocean Engineering and Marine Energy*, 3(1):69–87.

Karimirad, M. (2014). *Offshore Energy Structures*. Springer International Publishing, Switzerland.

Kauppinen, J. and Partanen, J. (2011). *Fourier Transforms in Spectroscopy*. Wiley-VCH, Berlin.

Kelley, N. and Jonkman, B. (2007). Overview of the turbsim stochastic inflow turbulence simulator, version 1.21. Technical Report NREL/TP-500-41137, National Renewable Energy Laboratory.

Kelley, N. D. (1992). Full vector (3-d) inflow simulation in natural and wind farm environments using an expanded version of the snlwind (veers) turbulence code. Tech. Rep. NRELtrP-442-5225, National Renewable Energy Laboratory.

Kirk, P. S. and Whitcomb, R. (1995). System for increasing airplane fuel mileage and airplane wing modification kit. US Patent 5,407,153.

Kleinhans, D., Friedrich, R., Schaffarczyk, A. P., and Peinke, J. (2008). Synthetic turbulence models for wind turbine applications. In Peinke, J., Oberlack, M., and Talamelli, A., editors, *Progress in Turbulence III: Proceedings of the iTi Conference in Turbulence 2008*, pages 111–114, Berlin, Heidelberg. Springer.

Kroese, D. P., Taimre, T., and Botev, Z. I. (2011). *Handbook of Monte Carlo Methods*. John Wiley & Sons, Hoboken, NJ, USA.

Lavely, A., Vijayakumar, G., Brasseur, J., Patterson, E., and Kinzel, M. (2012). Comparing unsteady loadings on wind turbines using turbsim and les flow fields. In *50th AIAA Aerospace Sciences Meeting and Exhibit*, Nashville, Tennessee. AIAA.

Lawton, S. and Crawford, C. (2012). Development and validation of libaero, a potential flow aerodynamics library for horizontal-axis wind turbines. In *31th ASME Wind Energy Symposium/50th AIAA Aerospace Sciences Meeting and Exhibit*, Nashville, Tennessee. AIAA.

Lawton, S. and Crawford, C. (2013). An analysis of an implicit vortex method for wind turbine wake modelling. In *51st AIAA Aerospace Sciences Meeting including the New Horizons Forum and Aerospace Exposition*.

Lawton, S. and Crawford, C. (2014). Investigation and optimization of blade tip winglets using an implicit free wake vortex method. In *Journal of Physics: Conference Series*, volume 524-1, page 012–033. IOP Publishing.

Le Maître, O. (2006). Développement en polynômes de chaos d'un modèle lagrangien d'écoulement autour d'un profil. *Comptes Rendus Mecanique*, 334(11):693–699.

Le Maître, O., Huberson, S., and De Cursi, E. S. (1999). Unsteady model of sail and flow interaction. *Journal of Fluids and Structures*, 13(1):37–59.

Le Maître, O., Knio, O., Najm, H., and Ghanem, R. G. (2001). A stochastic projection method for fluid flow: I. basic formulation. *Journal of Computational Physics*, 173(2):481–511.

Le Maître, O. P. and Knio, O. M. (2010). *Spectral methods for uncertainty quantification: with applications to computational fluid dynamics*. Springer,.

Lockwood, R., Swaddle, J. P., and Rayner, J. M. V. (1998). Avian wingtip shape reconsidered: wingtip shape indices and morphological adaptations to migration. *Journal of Avian Biology*, 29(3):273–292.

Lupton, R. (2014). *Frequency-domain modelling of floating wind turbines*. PhD thesis, University of Cambridge.

Majda, A. J. and Branicki, M. (2012). Lessons in uncertainty quantification for turbulent dynamical systems. *Discrete Cont. Dyn. Systems*, 32(9).

Mann, J. (1994). The spatial structure of neutral atmospheric surface-layer turbulence. *Journal of Fluid Mechanics*, 273(1):141–168.

Mann, J. (1998). Wind field simulation. *Probabilistic engineering mechanics*, 13(4):269–282.

Marks II, R. J. (2009). *Handbook of Fourier analysis & its applications*. Oxford University Press, New York.

Mastroianni, G. and Milovanovic, G. (2008). *Interpolation processes: Basic theory and applications*. Springer-Verlag, Berlin Heidelberg.

McWilliam, M. K. (2015). *Towards Multidisciplinary Design Optimization Capability of Horizontal Axis Wind Turbines*. PhD thesis, University of Victoria.

McWilliam, M. K., Lawton, S., and Crawford, C. A. (2013a). An implicit model for lagrangian vortex dynamics for horizontal axis wind turbine design optimization. In *54th AIAA/ASME/ASCE/AHS/ASC Structures, Structural Dynamics, and Materials Conference*, Boston, Massachusetts.

McWilliam, M. K., Lawton, S., and Crawford, C. A. (2013b). Towards a framework for aero-elastic multidisciplinary design optimization of horizontal axis wind turbines. In *32th ASME Wind Energy Symposium/51st AIAA Aerospace Sciences Meeting and Exhibit, Grapevine, TX*.

Merz, K. O. (2015a). Rapid optimization of stall-regulated wind turbine blades using a frequency-domain method: Part 1, loads analysis. *Wind Energy*, 18(10):1703–1723.

Merz, K. O. (2015b). Rapid optimization of stall-regulated wind turbine blades using a frequency-domain method: Part 2, cost function selection and results. *Wind Energy*, 18(6):955–977.

Milan, P., Wächter, M., and Peinke, J. (2013). Turbulent character of wind energy. *Physical Review Letters*, 110(13):138–701.

Morales, A., Wächter, M., and Peinke, J. (2012). Characterization of wind turbulence by higher-order statistics. *Wind Energy*, 15(3):391–406.

Moriarty, P. (2008). Database for validation of design load extrapolation techniques. *Wind Energy*, 11(6):559–576.

Moriarty, P. and Hansen, A. (2005). AeroDyn Theory Manual. Technical Report TP-500-36881, National Renewable Energy Laboratory.

Mücke, T., Kleinhans, D., and Peinke, J. (2011). Atmospheric turbulence and its influence on the alternating loads on wind turbines. *Wind Energy*, 14(2):301–316.

Munk, M. M. (1923). The minimum induced drag of airfoils. Technical Report 121, NACA.

Nagel, F. (1924). Flügel mit seitlichen Scheiben. In *Vorläufige Mitteilungen der Aerodynamischen Versuchsanstalt zu Göttingen*. in German.

Najm, H. N. (2009). Uncertainty quantification and polynomial chaos techniques in computational fluid dynamics. *Annual Review of Fluid Mechanics*, 41:35–52.

Navascués, M. A., Chand, A. K. B., Veedu, V. P., and Sebastián, M. V. (2014). Fractal interpolation functions: a short survey. *Applied Mathematics*, 2014.

Naylor, A. W. and Sell, G. R. (1971). *Linear operator theory in engineering and science*. Springer, New York.

Nielsen, M., Larsen, G. C., and Hansen, K. S. (2007). Simulation of inhomogeneous, non-stationary and non-gaussian turbulent winds. In *Journal of Physics: Conference Series*, volume 75. IOP Publishing.

Nielsen, M., Larsen, G. C., Mann, J., Ott, S., Hansen, K. S., and Pedersen, B. J. (2004). Wind simulation for extreme and fatigue loads. Technical Report Risø-R-1437 (EN), Risø.

Norberg, U. M. (1990). *Vertebrate flight: mechanics, physiology, morphology, ecology and evolution*. Springer-Verlag.

Padrón, A. S., Stanley, A. P. J., Thomas, J. J., Alonso, J. J., and Ning, A. (2016). Polynomial chaos for the computation of annual energy production in wind farm layout optimization. *Journal of Physics: Conference Series*, 753:032021.

Palutikof, J., Guo, X., and Halliday, J. (1991). The reconstruction of long wind speed records in the uk. In *Wind Energy Conversion, 1991: Proceedings of the 13th British Wind Energy Association Conference, 'Wind Energy and the Environment'*, pages 275–280.

Panofsky, H. A. & Dutton, J. A. (1984). *Atmospheric turbulence*. John Wiley & Sons, New York.

Park, J., Manuel, L., and Basu, S. (2015). Toward isolation of salient features in stable boundary layer wind fields that influence loads on wind turbines. *Energies*, 8(4):2977–3012.

Patel, C. K. and Kroo, I. (2006). Control law design for improving uav performance using wind turbulence. In *44th AIAA Aerospace Sciences Meeting and Exhibit*, Reno, Nevada. AIAA.

Peters, D. A. and He, C. J. (1991). Correlation of measured induced velocities with a finitestate wake model. *Journal of the American Helicopter Society*, 36(3):59–70.

Phillips, G. M. (2003). *Interpolation and approximation by polynomials*. Springer, New York.

Phillips, W. F. and Snyder, D. O. (2000). Modern adaptation of prandtl's classic lifting-line theory. *Journal of Aircraft*, 37(4):662–670.

Pitt, D. M. and Peters, D. A. (1981). Theoretical prediction of dynamic-inflow derivatives. *Vertica*, 5(1):21–34.

Prandtl, L. (1918). Tragflügeltheorie. I. Mitteilung. *Nachrichten von der Gesellschaft der Wissenschaften zu Göttingen, Mathematisch-Physikalische Klasse*, 1918:451–477. In German.

Prandtl, L. (1919). Tragflügeltheorie. II. Mitteilung. *Nachrichten von der Gesellschaft der Wissenschaften zu Göttingen, Mathematisch-Physikalische Klasse*, 1919:107–137. In German.

Rai, R. K., Gopalan, H., and Naughton, J. W. (2015). Effects of spatial and temporal resolution of the turbulent inflow on wind turbine performance estimation. *Wind Energy (online)*.

Reid, E. G. (1925). The effects of shielding the tips of airfoils. Technical report, NACA TR-201.

Sachs, G. and Moelyadi, M. A. (2006). Effect of slotted wing tips on yawing moment characteristics. *Journal of theoretical biology*, 239(1):93–100.

Schlichting, H. and Truckenbrodt, E. A. (2000). *Aerodynamik des Flugzeuges.*, volume 2. Springer Verlag.

Sheldahl, R. E. and Klimas, P. C. (1981). Aerodynamic characteristics of seven symmetrical airfoil sections through 180-degree angle of attack for use in aerodynamic analysis of vertical axis wind turbines. Technical Report SAND-80-2114, Sandia National Labs.

Shives, M. R. (2011). Hydrodynamic modeling, optimization and performance assessment for ducted and non-ducted tidal turbines. Master's thesis, University of Victoria.

Simonoff, J. S. (1996). *Smoothing methods in statistics*. Springer series in statistics. Springer, New York.

Smith, J. O. (2007). Mathematics of the discrete fourier transform (dft) with audio applications, second edition. http://ccrma.stanford.edu/ jos/mdft/, online book, 2007 edition, accessed July 27, 2015.

Smith, M., Komerath, N., Ames, R., Wong, O., and Pearson, J. (2001). Performance analysis of a wing with multiple winglets. In *19th AIAA Applied Aerodynamics Conference*, Anaheim, CA.

Smith, S. C. (1996). A computational and experimental study of nonlinear aspects of induced drag. Technical Report NASA TP3598, NASA.

Somers, D. (2005). Design and experimental results for the s825 airfoil. Technical Report NREL/SR-500-36346, National Renewable Energy Laboratory.

Steffensen, J. F. (2006). *Interpolation*. Dover, Mineola, 2nd ed. edition.

Stiesdal, H. (2013). Redefining the cost debate - the concept of society's cost of electricity. In *Global Wind Report - Annual Market Update 2013*. GWEC.

Stresing, R. and Peinke, J. (2010). Towards a stochastic multi-point description of turbulence. *New Journal of Physics*, 12(10):103046.

Sudret, B. (2007). Uncertainty propagation and sensitivity analysis in mechanical models–contributions to structural reliability and stochastic spectral methods. *Habilitation a diriger des recherches, Université Blaise Pascal, Clermont-Ferrand, France*.

Sullivan, T. J. (2015). *Introduction to uncertainty quantification*. Springer, Switzerland.

Suzuki, D. (2014). Windmills are things of beauty. online. http://www.davidsuzuki.org/blogs/science-matters/2014/04/windmills-are-things-of-beauty/, accessed April 12, 2014.

Swaddle, J. P. and Lockwood, R. (2003). Wingtip shape and flight performance in the european starling sturnus vulgaris. *Ibis*, 145(3):457–464.

Tibaldi, C., Henriksen, L. C., and Bak, C. (2014). Investigation of the dependency of wind turbine loads on the simulation time. In *Proceedings of EWEA 2014, Barcelona, Spain*. European Wind Energy Association (EWEA).

Tucker, V. et al. (1995). Drag reduction by wing tip slots in a gliding harris' hawk, parabuteo unicinctus. *Journal of experimental biology*, 198(3):775–781.

Tucker, V. A. (1993). Gliding birds: reduction of induced drag by wing tip slots between the primary feathers. *Journal of experimental biology*, 180(1):285–310.

Van Garrel, A. (2003). Development of a wind turbine aerodynamics simulation module. Technical Report ECN-C-03-079, ECN.

Veers, P. S. (1988). Three-dimensional wind simulation. Technical Report SAND88–0152, UC–261, Sandia National Labs.

Vijayakumar, G., Brasseur, J., Lavely, A., Jayaraman, B., and Craven, B. (2016). Interaction of atmospheric turbulence with blade boundary layer dynamics on a 5MW wind turbine using blade-boundary-layer-resolved CFD with hybrid URANS-LES. In *34th Wind Energy Symposium, AIAA SciTech*, San Diego, California. AIAA.

Wang, K., Moan, T., and Hansen, M. O. L. (2016). Stochastic dynamic response analysis of a floatingvertical-axis wind turbine with a semi-submersible floater. *Wind Energy (online)*.

Welch, P. (1967). The use of fast fourier transform for the estimation of power spectra: A method based on time averaging over short, modified periodograms. *IEEE Transactions on Audio and Electroacoustics*, 15(2):70–73.

Whitcomb, R. T. (1976). A design approach and selected wind-tunnel results at high subsonic mounted speeds for winglets. Technical Note D-8260, NASA.

Wikipedia (2015). Nyquist–shannon sampling theorem — Wikipedia, the free encyclopedia. [Online; accessed 27-July-2015].

Williams, T., Wang, D., Crawford, C., and Djilali, N. (2013). Integrating renewable energy using a smart distribution system: Potential of self-regulating demand response. *Renewable Energy*, 52(0):46–56.

Williams, T. J. (2012). *Probabilistic Power Flow Modeling of Renewable Energy and PEV Grid Interactions*. PhD thesis, University of Victoria.

Withers, P. C. (1981). The aerodynamic performance of the wing in red-shouldered hawk buteo lznearzs and a possible aeroelastic role of wing-tip slots. *Ibis*, 123(2):239–247.

Wächter, M., Heißelmann, H., Hölling, M., Morales, A., Milan, P., Mücke, T., Peinke, J., Reinke, N., and Rinn, P. (2012). The turbulent nature of the atmospheric boundary layer and its impact on the wind energy conversion process. *Journal of Turbulence*, 13:N26.

Xiu, D. and Karniadakis, G. E. (2002). The Wiener–Askey polynomial chaos for stochastic differential equations. *SIAM Journal on Scientific Computing*, 24(2):619–644.

Zhang, L., Ye, T., Xin, Y., Han, F., and Fan, G. (2010). Problems and measures of power grid accommodating large scale wind power [j]. *Proceedings of the CSEE*, 25:002.

Zhang, P. and Huang, S. (2011). Review of aeroelasticity for wind turbine: Current status, research focus and future perspectives. *Frontiers in Energy*, 5(4):419–434.

Zhou, N., Chen, J., Adams, D. E., and Fleeter, S. (2016). Influence of inflow conditions on turbine loading and wake structures predicted by large eddy simulations using exact geometry. *Wind Energy*, 19(5):803–824.

Zwick, D. and Muskulus, M. (2015). The simulation error caused by input loading variability in offshore wind turbine structural analysis. *Wind Energy*, 18(8):1421–1432.

Appendix A

Some Practical Notes on the Discrete Fourier Transform – An Engineering Perspective

Spectral models, and with them Fourier transforms and Fourier series are instrumental for this dissertation. Hence, this appendix will summarize a few notes on Fourier theory. These notes are compiled from multiple sources. Personally I found the online book by Smith (2007) the the best.

The MATLAB scripts *testingFourier.m*, *Fourier_VKMspectrum.m*, and *testingFourierOrthogonality.m* can be used to experiment with the theory presented in the sequel. These scripts can be found on the SSDL group's server (ssdl.me.uvic.ca) in the directory `projects/stochasticGalerkin/sandbox/`. Access authorization may be requested from Dr. Crawford.

These notes are meant to help the ones continuing this work after me to dive into the matter quickly. Emphasis is put onto an easily comprehensible introduction for engineering practitioners, rather than a mathematically rigorous treatment of the theory.

A.1 Basic definitions and nomenclature

For two discrete functions $x(n)$, $y(n)$ inner product of Eq. 5.1 turns into

$$\langle x(n), y(n) \rangle = \frac{1}{N} \sum_{n=0}^{N-1} x(n) y^*(n) \tag{A.1}$$

with y^* denoting the conjugate complex of y. Let moreover

$$s_k(n) = e^{i\omega_k t_n} = e^{i2\pi kn/N} \tag{A.2}$$

be the k-th complex harmonic with:

$\boldsymbol{\omega} = [\omega_k] = 2\pi\,[f_k]$, with $\omega_k = 2\pi\, k/(N\,\Delta t)$, $\qquad k = 0, \ldots, N-1$

$\boldsymbol{f} = [f_k]$, with $f_k = k/(N\,\Delta t) = k/T = k f_s/N$,

i.e. $\boldsymbol{f} = [0, f_s/N, 2f_s/N, \ldots, (N-1)f_s/N]$

and

$\boldsymbol{t} = [t_n]$, with $t_n = n\Delta t$, $\qquad n = 0, \ldots, N-1$

We then call:

$f_s = 1/\Delta t$	the sampling frequency ($f_s/2$: 'highest frequency in spectrum')
$T = N\,\Delta t$	the sampling time (T: 'longest period in spectrum')
$1/T = 1/(N\Delta t)$	lowest frequency in spectrum.

The highest resolved frequency $f_s/2$ is called the Nyquist frequency. Higher frequencies, which might appear in the spectrum for $f > F_s/2$, are only shifted negative frequencies, which appear through periodicity, but do not contribute additional information.

Note that for the conjugate complex

$$s_k^*(n) = s_k(-n) \tag{A.3}$$

and that s_k, s_l^* are orthonormal for **integers** $k, l \in \mathbb{N}_0$ (see section A.5.3):

$$\langle s_k(n), s_l(n) \rangle = \frac{1}{N} \sum_{n=0}^{N-1} s_k(n) s_l(-n) = \delta_{nl} \tag{A.4}$$

with δ denoting the Kronecker Delta.

A.2 Transforming to frequency space and back

The (discrete) Fourier transform (DFT) of a discrete time series $x(t_n) = x(n)$ is obtained with the inner product of Eq. A.1. Write

$$x(t_n) = \sum_{\omega_k \in \boldsymbol{\omega}} X(\omega_k)\, e^{i\omega_k t_n} \tag{A.5}$$

with: $\boldsymbol{\omega} = [\omega_k]$, $k = 0...N-1$. By projecting both sides of Eq. A.5 onto $s_k(n)$ via the inner product of Eq. A.1 we obtain the Fourer coefficients $X(\omega_k)$. With $\omega_k = 2\pi\, k/(N\,\Delta t)$ and $t_n = n\Delta t$ and Eq. A.4 we get:

$$X(\omega_k) = \langle x(n), s_k(n)\rangle = \frac{1}{N}\sum_{t_n \in \boldsymbol{t}} x(t)\, e^{-i\omega_k t_n} \tag{A.6}$$

In general the spectrum $X(\omega_k)$ is complex, with the amplitudes $|X(\omega_k)|$ and the phase angles $\theta = \arctan(\frac{\mathrm{Im}[X(\omega_k)]}{\mathrm{Re}[X(\omega_k)]})$ for each harmonic $s_k(n)$. The (discrete) power spectrum, which we will use later to describe a wind speed time series, is:

$$S(\omega_k) = |X(\omega_k)|^2 \tag{A.7}$$

Note, however, that through the absolute value operation all phase information is lost.

The time series can be recovered via the inverse (discrete) Fourier transformation (iDFT) of Eq. A.5.

A.3 Two-sided vs. one-sided spectrum

For a real valued signal the spectrum $X(\omega_k)$ is symmetric about $\omega_{N/2} = \pi/\Delta t$ with $X(\omega_k) = X^*(\omega_{N-k})$.[20] Hence $X(\omega_{\bar{k}})$ with $\bar{k} = 0\ldots N/2$ alone contains the full information of the (real valued) signal. This is referred to as the 'one-sided' spectrum, vs. the 'double sided' spectrum when $k = 0\ldots N-1$ is used.

[20] N.B.: this holds only for *real* signals. The spectrum of complex signals, as encountered in Chapter 7, is generally not symmetric!

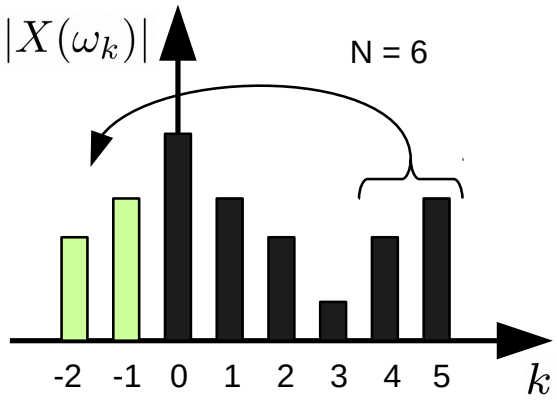

Figure A.1: Scematic of a two-sided spectrum and how to take advantage of the symmetry.

Using a one sided spectrum is attractive, since it reduces the number of necessary frequencies, i.e. the number of data stored, the number of floating point operations, and/ or the number of random phase angles. If the full spectrum obtained from the DFT contains N frequencies the one-sided spectrum contains $N/2+1$ frequencies. But how are the two-sided vs. one-sided Fourier series connected?

To answer this question we recall Euler's identity

$$e^{i\omega t_n} = \cos(\omega t_n) + i\sin(\omega t_n) \tag{A.8}$$

which can also (and more helpfully for the following discussion) be written:

$$\cos(\omega t_n) = \frac{1}{2}e^{i(-\omega)t_n} + \frac{1}{2}e^{i\omega t_n} \tag{A.9a}$$

$$\sin(\omega t_n) = \frac{1}{2}e^{i(-\omega)t_n} - \frac{1}{2}e^{i\omega t_n} \tag{A.9b}$$

Further on we note (again, only for a real signal!):

1. For periodic signals (n.b. periodicity is inherently assumed with finite signals) spectrum is symmetric about $\omega_{N/2}$, the Nyquist frequency. See Fig. A.1.

2. Two amplitudes appear only once. These are the ones for ω_0 and $\omega_{N/2}$. At these frequencies $\sin(2\pi k/(Nt_n)) = 0$ and hence the complex part of the spectrum is irrelevant: $\mathrm{Im}[X(\omega_0)] = \mathrm{Im}[X(\omega_{N/2})] = 0$.

Further at $\omega_0 = 0$, $\cos(0) = 1$, and $X(\omega_0) = \bar{x}$, the mean value.
For the middle frequency $k = N/2$ we get $\omega_{N/2} = 2\pi f_k = m\pi$ and $\cos(m\pi t_n) = \pm 1$.

3. For all other frequencies the amplitudes appear twice, and $X(\omega_k) = X^*(\omega_{N/2-k})$.

4. The identities $e^{2m\,i\pi} = 1$ and $e^{(2m-1)\,i\pi} = -1$ hold for any integer $m \in \mathbb{N}$. Consequently we get $e^{i(x+2m\pi)} = e^{ix}$ and $e^{i(x+(2m-1)\pi)} = e^{-ix}$.

From point 3 we see that all the information is actually contained in the spectrum from 0 to $N/2$. Now we take advantage of this:
Based on point 4 we shift all frequencies ω_k for $k > N/2 + 1$ to $\omega_j = \omega_k - \pi$ with $j = k - N$. **Note that this is a shift, not a mirroring of the spectrum!** See green frequencies in Fig. A.1.

Attention: be careful when using frequencies ω_k with $k > N/2 + 1$. In test cases this lead to trouble (strong oscillations between support points). Better use negative frequencies.[21]

This means that $X(\omega_k) = X(\omega_j) + X(\omega_l)$ for $k = 0, \ldots, N-1$ and for the new case $j = -N/2 + 1, \ldots, 0$ and $l = 0, \ldots, N/2$. Hence $\omega_j = -\omega_l$. Keeping point 2 in mind, Eq. A.5 can now be re-written:

$$x(t_n) = \frac{1}{N} \sum_{k=-N/2+1}^{N/2} X(\omega_k)\, e^{i\omega_k t_n} = \frac{1}{N} \left(X(\omega_0) + \sum_{k=1}^{N/2-1} X(\omega_k) e^{i\omega_k t_n} + X^*(\omega_k) e^{-i\omega_k t_n} + X(\omega_{N/2}) e^{i\omega_{N/2} t_n} \right) \quad \text{(A.10)}$$

This is the one-sided notation. Note that here the frequencies ω_0 and $\omega_{N/2}$ have to be dealt with separately, because these two only appear once while all other frequencies

[21] Reason: for a signal recorded at N sample points ω_k completes at most one period every two sample intervals (i.e. over three sample points) at $k = N/2 + 1$. This means a smooth interpolation between samples because there is at most one peak between two sample points. Higher frequencies ($k > N/2 + 1$) result in more than one period over there samples, up to one period for over only two samples for $k = N$. This leads to extra osscilations between samples points, as now we extract more frequencies than we actually supply data. (Remember: each frequency contains two pieces of information, amplitude and phase.)

come in pairs. Since $X(\omega_0) = \bar{x}$, and $x + x^* = 2\,Re[x]$ Eq. A.10 further simplifies to:

$$x(t_n) = \frac{1}{N}\left(\bar{x} + 2\,Re\left[\sum_{k=1}^{N/2-1} X(\omega_k) e^{i\omega_k t_n}\right] + X(\omega_{N/2}) e^{i\omega_{N/2} t_n}\right) \tag{A.11}$$

The last term in Eq. A.11 seems to be often neglected as it is usually small.

A.4 Synthesizing turbulent wind (via iDFT)

Now we turn to a turbulent wind sample composed of L frequencies. The phase angle ϕ_l of each of these frequencies ω_l $(l = 0, ...L-1)$ is assumed to be random (with uniform distribution), and only the power *density* spectrum $S_u(\omega_l)$ is given. Note that the spectra S_u given in literature (e.g. (Burton et al., 2011) and (IEC 61400-1, Ed. 3, 2005)) are often continuous power spectra. We adopt the notation used by Veers (1988) with

- G denoting the *continuous* power spectrum
- S the *discrete* power spectrum and
- S_u the *discrete* power spectral density.

For homogeneous frequency bin sizes Δf we get

$$S = S_u\,\Delta f = G\Delta f = G\frac{f_s}{N} = X\frac{1}{N} \tag{A.12}$$

Based on eq. A.5 the wind field can thus be synthesized with the amplitude spectrum $X(\omega_l)$:

$$u(t_n) = \sum_{\omega_l \in \boldsymbol{\omega}} X(\omega_l)\, e^{i\omega_l t_n} = \sum_{\omega_l \in \boldsymbol{\omega}} \sqrt{\frac{S_u(\omega_l)\,\Delta f}{2}}\, e^{i(\omega_l t_n + \phi_l)} \tag{A.13}$$

Here S_u is assumed to be the one sided power spectrum, where $l = 0, \ldots, N-1$. **N.B.**: The scaling (factor 2) from a one-sided to a two-sided spectrum often happens happens at power (*not* frequency) spectrum level! Depending on how data from other sources (e.g. literature) is scaled a factor 2, or $\sqrt{2}$ might have to be introduced into

the Fourier sum.

Random phase angles for each frequency are realized by adding a random constant to each Fourier mode:

$$u(t_n) = \sum_{\omega_l \in \boldsymbol{\omega}} \sqrt{\frac{S_u(\omega_l)\,\Delta f}{2}}\, e^{i(\omega_l t_n + \phi_l)} \tag{A.14}$$

A shift (i.e. time lag) of the whole signal is achieved via

$$u(t + m\Delta t_n) = \sum_{\omega_l \in \boldsymbol{\omega}} \sqrt{\frac{S_u(\omega_l)\,\Delta f}{2}}\, e^{i\omega_l(t_n+\delta)} = e^{i\omega_l \delta} \sum_{\omega_l \in \boldsymbol{\omega}} \sqrt{\frac{S_u(\omega_l)\,\Delta f}{2}}\, e^{i\omega_l t_n} \tag{A.15}$$

with $\delta = m\Delta t$ the time lag in terms of multiple of the sampling time step Δt. Note the difference of a phase shift ϕ_l (Eq. A.14) and a time shift δ (Eq. A.15)! This is the shift theorem, c.f. Smith (2007).

A.5 Some general remarks

In the following we collect some general remarks relevant to the use of the Fourier transform in this dissertation.

A.5.1 Aliasing

From pure trigonometry we know:

$$\cos\left(2\pi(f + \frac{1}{\Delta t})k\Delta t\right) = \cos\left(2\pi f k \Delta t\right) \tag{A.16}$$

and similarly for sinus terms.

Hence the Fourier transformation of Eq. A.5 produces a spectrum that repeats after the highest frequency $\bar{f} = \frac{1}{\Delta t}$. For a double sided spectrum with frequencies ω_k, $k \in [0; N/2]$ this means the spectrum (more precisely it's negative part) starts repeating at $\omega_{\bar{k}}$ with $\bar{k} = N - N/2 + 1 = N/2 + 1$. This is the same property that also

leads to the symmetry exploited to use a one-sided spectrum (depicted in Fig. A.1). However, when not sampling at a high enough frequency $f_s > f_N$ with f_N the Nyquist frequency (i.e. double the highest frequency in the signal) energy from the aliased spectrum will "leak" into the actual spectrum and generate "false" amplitudes. This is the Nyquist–Shannon sampling theorem, nicely explained by Wikipedia (2015).

A.5.2 Variance

The variance of any sinusoid with amplitude a is

$$\mathrm{Var}[a\sin(x)] = \frac{a^2}{2\pi}\int_0^{2\pi}\sin^2(x)\,dx = \frac{a^2}{2} \tag{A.17}$$

Similarly for each cosine term: $\mathrm{Var}[a\cos(x)] = a^2/2$. Thus, with Eq. A.8 we get for each harmonic in the complex Fourier series of Eq. A.5:

$$\mathrm{Var}[X(\omega_k)\,e^{i\omega_k t}] = |X(\omega_k)|^2 \tag{A.18}$$

Hence the variance of a signal $x(t)$ synthesized through iDFT from a discrete frequency spectrum $X(\omega_k)$ is

$$\mathrm{Var}[x(t)] = \sum_{k=1}^{N-1}\left(|X(\omega_k)|\right)^2 \tag{A.19}$$

Care must be taken which spectrum is used. Particularly if a one-sided spectrum is employed, because depending on how the one-sided vs. two-sided scaling (Wq. A.12) was performed, i.e. with the power or the frequency spectrum, a factor $\sqrt{2}$ may appear somewhere.

N.B.: With a typical turbulent wind spectrum Eq. A.19 does not converge for a long time, i.e. with decreasing ω_1. The reason is that there is ample energy in the spectrum up to very low frequencies. Consider for example seasonal, annual and even decadal wind variations, cf. Burton et al. (2011, Section 2.3) and Palutikof et al. (1991).

A.5.3 Orthogonality

The complex sinusoid is defined via Eq. A.2. For discrete sinusoids the orthogonality of the sinusoids is derived e.g. by Smith (2007, section 6.3).

For continuous sinusoids we get

$$\langle s_k(t), s_l(t)\rangle = \int_0^T e^{i\omega_k t} e^{-i\omega_l t} dt = \int_0^T e^{i(\omega_k-\omega_l)t} dt = \left[\frac{e^{i(\omega_k-\omega_l)t}}{i(\omega_k-\omega_l)}\right]_0^T = \frac{e^{i(\omega_k-\omega_l)T}-1}{i(\omega_k-\omega_l)} \tag{A.20}$$

again setting $\omega_k = \frac{2\pi k}{T}$ and $\omega_l = \frac{2\pi l}{T}$we get

$$\langle s_k(t), s_l(t)\rangle = \frac{e^{i2\pi(k-l)}-1}{i\frac{2\pi}{T}(k-l)} = \begin{cases} 0 & \text{for } k \neq l \\ T & \text{for } k = l \end{cases} \tag{A.21}$$

Where we used $e^{i2\pi n} = 1$ for $n \in \mathbb{N}_0$ for the first case ($k \neq l$). For $k = l$ we employ l'Hospital's rule and obtain

$$\lim_{k\to l} \frac{e^{i2\pi(k-l)}-1}{i\frac{2\pi}{T}(k-l)} \overset{l'Hop}{=} \lim_{k\to l} \frac{i2\pi e^{i2\pi(k-l)}}{i\frac{2\pi}{T}} = T \tag{A.22}$$

Note: the same result is directly obtained form Eq. A.20 with $\omega_k = \omega_l$

$$\int_0^T e^{i(\omega_k-\omega_l)t} dt = \int_0^T e^0 dt = [t]_0^T = T \tag{A.23}$$

Appendix B

A Minimal Example for the Stochastic Projection Procedure

When someone starts dealing with stochastic methods and wants to look into stochastic projection methods the learning curve is initially very steep. For an easier start into the material a minimal example is presented here. We recommend the interested reader to work through this example (and possibly implement the equations themselves) as a start and before diving into the more complex problems presented in the body of this dissertation.

B.1 Problem definition

Consider a cantilever beam with a point load at its free end, see Fig. B.1. The governing equation for the beam bending deflection y is (setting $EI = 1$):

$$\frac{d^2}{dx^2}y = -M(x) = -F(1-x) \tag{B.1}$$

with the boundary conditions

$$y(0) = \frac{d}{dx}y(0) = 0 \tag{B.2}$$

This simple problem will serve as a minimal example to illustrate the chosen method and to verify the fundamental suitability of the chosen model to simplify unsteady time series calculations.

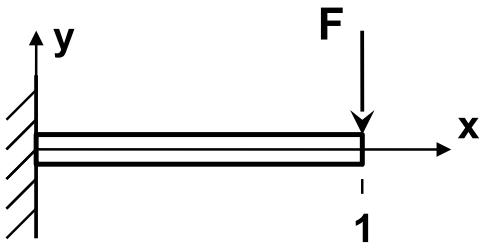

Figure B.1: The example set-up: a clamped beam with a point load.

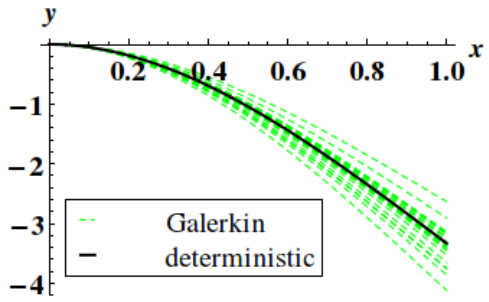

Figure B.2: Beam deflection results for the deterministic load and for 20 random realizations.

In the deterministic case (known and constant F) the solution to Eq. B.1 is:

$$y(x) = \frac{F}{6}(x^3 - 3x^2) \tag{B.3}$$

B.2 Stochastic solution

Now let us assume the load varies randomly in time (with no memory or time-lag):

$$F(t) = 10 + \xi(t) \tag{B.4}$$

With $\xi(t)$ a standard normal distributed random variable. Suppose moreover that Eqs. B.3 and B.4 are more complicated and the system non-linear, such that simply substituting Eq. B.4 in Eq. B.3 is not an option. For simplicity we assume a quasi static process with no dynamics in the beam (infinite damping and zero inertia). Thus each time step is independent from any other time step. Since the random variables are normal distributed we follow Xiu and Karniadakis (2002) and choose to use Hermite chaos polynomials $H_k(\xi)$ as basis for the stochastic space.[22] Thus we can express the solution deflection as a polynomial chaos expansion (PCE):

$$\tilde{y}(x, \omega) = \sum_{n=0}^{P-1} s_n(x) H_n(\xi) \tag{B.5}$$

[22] The lengthy definition of the Hermite polynomials is not repeated here. For details see e.g. Abramowitz and Stegun (1972, p. 775).

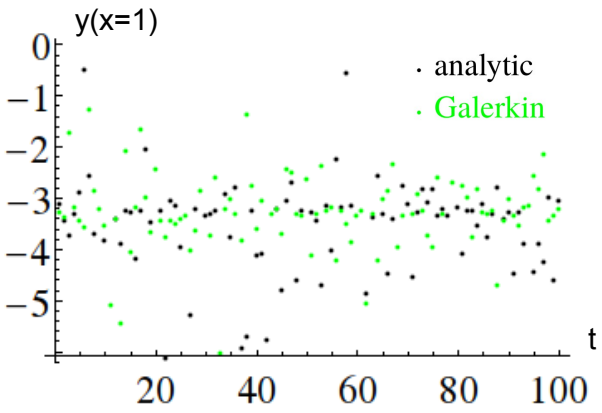

Figure B.3: Resulting series for 100 realizations of tip deflection $y(x = 1)$ for a Monte Carlo experiment versus the stochastic Galerkin solution.

Inserting Eq. B.4 and B.5 in Eq. B.1 and executing the Galerkin projection (i.e. taking the inner product $\langle \square, H_m(\xi) \rangle$, Eq. 5.1, of the system equation) for all basis functions H_m with $m \in [0, P-1]$ over the stochastic space $\Omega = \mathbb{R}$ yields:

$$\int_{-\infty}^{\infty} \left(\sum_{n=0}^{P-1} \frac{d^2 s_n(x)}{dx^2} H_n(\xi) + (10 + \xi)(1 - x) \right) H_m(\xi) p(\xi)\, d\xi = 0 \tag{B.6}$$

With the projection weights set equal to the PDF of the random variable $p(\xi) = \frac{1}{\sqrt{2\pi}} \exp\left(-\frac{\xi^2}{2}\right)$ and $n = 0, 1, \ldots, P-1$, this gives a system of P equations for the P unknown solution coefficients $s_n(x)$ (with $n = 0, 1, \ldots, P-1$). With the boundary conditions (Eq. B.2) the equations for each n can readily be solved:

$$\begin{aligned} s_0 &= \frac{10}{6}(x^3 - 3x^2) \\ s_1 &= \frac{1}{6}(x^3 - 3x^2) \\ s_n &= 0 \qquad \text{for} \quad n = 2, 3, ..., P-1, \end{aligned} \tag{B.7}$$

Thus we obtain the result for the stochastic deflection from the series of Eq. B.5

$$\tilde{y}(x) = \frac{1}{6}(10 + \xi)(x^3 - 3x^2) \tag{B.8}$$

For known and constant load F, i.e. $\xi = 0$, Eq. B.8 immediately recovers the deterministic solution. Fig. B.2 shows the results for the deterministic load and for 20 random realizations of Eq. B.8.

B.3 Discussion

For a time series with $\xi_i(t)$ independent realizations, Eq. B.8 now directly gives the deflection for all times from one single solve – without re-evaluating the whole model each time step. In this simple case the gain in computational effort is not relevant, as the initial system equation (Eq. B.1) could have been solved easily and as a function of an arbitrary load F quickly. However, once the system becomes more complicated (cf. Chapters 5 and 6) or non-linear (cf. Chapter 7) such an easy solution may not be available any more. In that case having Eq. B.8 as a faster approximation of the stochastic solution is valuable for reducing computational expenses: now a set of model responses can directly be calculated from one single stochastic evaluation (instead of a possibly expensive recurring solve of the system equations though the whole time series). Fig. B.3 shows the resulting time series for 100 time steps. Once the deflection $y(t)$ is obtained from solving Eq. B.1 for 100 different forces $F(t)$ (a Monte Carlo experiment), the other time from 100 realizations of Eq. B.8 (the stochastic Galerkin solution). As can be seen the processes seem statistically similar. Table B.1 compares the expected value and the variance from the Monte Carlo simulations (for one set of 1000 realizations) of to the values obtained via Eq. B.8 for the stochastic Galerkin solution. It confirms the impression from Fig. B.3: both processes are statistically equivalent. Moreover, it can be seen that in this simple case, where the random process is fully captured by a PC series of two terms, the stochastic Galerkin method reproduces the analytic mean value and variance exactly.

Table B.1: Statistics of tip deflection for the randomly loaded beam.

	Monte Carlo	stochastic Galerkin	analytic
mean	-3.348	$-10/3$	-10/3
variance	0.1097	1/9	1/9

Appendix C

Overview on Scripts and Code

All calculation scripts and all code relevant for this work can be found on the SSDL group's server (ssdl.me.uvic.ca). The projects are each under Mercurial Version control and can be cloned to a local drive after authorization by Dr. Crawford. Some custom MATLAB functions globally used can be found in: `projects/Matlab_functionLib/`

The work presented throughout this dissertation strongly builds on each other. Consequently, the computation code related to each section is dependent on each other. Each of the projects presented in the following, which are each stored in their own folders, are kept fairly independent. However, in some instances this was not practicable and some functions from one project need to be made accessible for another. Although spread over different folders all necessary files are available in the `/export/project/projects/`. At the time of writing this dissertation, this folder was located at `/export/project/`.

This appendix will give an overview of the available scripts and code related to the projects presented in the chapters of this dissertation.

C.1 Bird wing vortex code (C++)

The repository for the files related to the bird wing project presented in Chapter 2 can be found at: `projects/birdWing`.

This project is implemented in C++; CMake is used for building. `BirdMain.cpp` is the main file, `setup.conf` defines the wing geometry and flow conditions. All other necessary files are contained in the same folder or its sub-folders. Comments in the code explain their proper use and functionality.

C.2 Wind interpolation (Matlab)

The repository for the MATLAB files related to the turbulent wind interpolation project presented in Chapter 3 can be found at: `projects/windInterpolation`

The main scripts are *incrementInterpolTS.m* and *incrementInterpolTS_rotSample.m* for the stationary and the rotationally sampled interpolation respectively. Comments in the scripts explain their proper use and functionality. Sub-functions are in the same folder. TurbSim wind data is supplied in the sub-folder `/turbsim`, which is not under version control (for its large size).

C.3 Turbulent wind synthesizing

C.3.1 Veers model (Matlab)

In various places throughout this dissertation we use our own implementation of Veers' wind model. The MATLAB function *makeWindVeers(v0,P,Nf,dt_fft)* generates such a wind wind field for the data points P, with mean wind speed *v0*, from *Nf* frequencies resolved at a time step of *dt_fft*. This function can be found at `projects/stochasticGalerkin/3dWindField`

Comments in the code explain the use of this function and reference to Veers paper (Veers, 1988). Sub-functions are in the same folder.

C.3.2 Reduced order Veers model (Matlab)

The reduced order version of Veers' wind model is implemented in the MATLAB script *severalPoints.m*, available at `projects/stochasticGalerkin/3dWindField`.

This script compares wind data from different models (TurbSim, Veers original model, cf. Section C.3) to the reduced order model. The wind speed data is evaluated at several user-selected points in space. This is the script used to generate most of the results in Chapter 6. Comments in the script explains the proper use and functionality.

C.4 Stochastic solution of unsteady aerodynamic equations

C.4.1 Lagrangian vortex model for horseshoe wing and translating blade with correlated sections (Matlab)

The Lagrangian vortex model used to analyze the translating blade with correlated sections (cf. Chapter 6) is a direct evolution of the simple horseshoe vortex wing model (cf. Chapter 5). Hence, the MATLAB implementations for both models are in the same folder: `projects/stochasticGalerkin/2dHorseshoe`.

The MATLAB script *unsteady_multidim.m* is the latest implementation of the unsteady Lagrangian vortex equations using polynomial chaos functions (cf. Section 5.3.3). The script *unsteady_complexFourier.m* is the latest implementation of the unsteady Lagrangian vortex equations using complex (Fourier) exponential functions (cf. Section 5.3.2). The script *correlatedWing.m* is used for the analysis of a translating wing with correlated bound vortex elements of Chapter 6. Comments in the scripts explain their proper use and functionality.

These scripts use the chaos polynomials and Fourier exponential functions which are supplied in the folder `projects/stochasticGalerkin/Polynomials`.
The formulation of these polynomials is instrumental to the work presented here. Thus this folder is under its own version control.

C.4.2 Stochastic wind turbine Blade Element Momentum (Matlab)

The code used for the stochastic Blade Element Momentum analysis of Chapter 7 is stored in the folder: `projects/stochasticGalerkin/BEM`.

The stochastic thrust solution is calculated in the MATLAB script *bem_stochastic.m*. The torque solution in *bem_stochasticTQ.m*. The script *makePDF.m* generates multiple solutions and populates the PDFs of Section 7.3.4. Comments in the scripts explain their proper use and functionality.